The Dissertation Committee for Henry Chang
certifies that this is the approved version of the following dissertation:

Modeling Turbulence using Optimal Large Eddy Simulation

Committee:

Robert D. Moser, Supervisor

Bjorn Engquist

Omar Ghattas

Thomas J.R. Hughes

Venkat Raman

Modeling Turbulence using Optimal Large Eddy Simulation

by

Henry Chang, B.S.; M.S.

DISSERTATION

Presented to the Faculty of the Graduate School of

The University of Texas at Austin

in Partial Fulfillment

of the Requirements

for the Degree of

DOCTOR OF PHILOSOPHY

THE UNIVERSITY OF TEXAS AT AUSTIN

May 2012

In loving memory of Ye-Ye, Nai-Nai, Ah-Gong, and Ah-Ma.

Acknowledgments

I am most grateful to my advisor, Professor Robert D. Moser, for his guidance and motivation through out my graduate school career. It has been a blessing to work for an advisor with such expertise in turbulence and computation, as well as the skills and patience to mentor young researchers like myself. A similar acknowledgment must be given to my college fluid mechanics professor, Edwin G. Wiggins, who sparked my interest in the subject and supervised my undergraduate thesis. I would like to thank my committee members Professors Graham F. Carey, Bjorn Engquist, Omar Ghattas, Thomas J.R. Hughes, and Venkat Raman for valuable discussions and suggestions regarding this dissertation. I must also thank (former) fellow graduate students Amitabh Bhattacharya, Paulo Zandonade, and Shan Yang for their contributions to this dissertation. Amitabh was very helpful through out, from correlation modeling for isotropic turbulence to LES modeling for channel flow. He has been like a second advisor for me. Paulo provided isotropic turbulence data and a well-written finite-volume code, and Shan taught me constrained optimization for modeling pressure. I gratefully acknowledge the Air Force Office of Scientific Research, the National Science Foundation, and the W. A. "Tex" Moncrief Chair in Computational Engineering and Sciences for funding this research. I am thankful for the camaraderie, friendships, and enlightening discussions with classmates and colleagues at the University of Texas. Finally, I am grateful to my family and friends for their support and encouragement.

Modeling Turbulence using Optimal Large Eddy Simulation

Henry Chang, Ph.D.
The University of Texas at Austin, 2012

Supervisor: Robert D. Moser

Most flows in nature and engineering are turbulent, and many are wall-bounded. Further, in turbulent flows, the turbulence generally has a large impact on the behavior of the flow. It is therefore important to be able to predict the effects of turbulence in such flows. The Navier-Stokes equations are known to be an excellent model of the turbulence phenomenon. In simple geometries and low Reynolds numbers, very accurate numerical solutions of the Navier-Stokes equations (direct numerical simulation, or DNS) have been used to study the details of turbulent flows. However, DNS of high Reynolds number turbulent flows in complex geometries is impractical because of the escalation of computational cost with Reynolds number, due to the increasing range of spatial and temporal scales.

In Large Eddy Simulation (LES), only the large-scale turbulence is simulated, while the effects of the small scales are modeled (subgrid models). LES therefore reduces computational expense, allowing flows of higher Reynolds number and more complexity to be simulated. However, this is at the cost of the subgrid modeling problem.

The goal of the current research is then to develop new subgrid models consistent with the statistical properties of turbulence. The modeling approach pursued

here is that of “Optimal LES”. Optimal LES is a framework for constructing models with minimum error relative to an ideal LES model. The multi-point statistics used as input to the optimal LES procedure can be gathered from DNS of the same flow. However, for an optimal LES to be truly predictive, we must free ourselves from dependence on existing DNS data. We have done this by obtaining the required statistics from theoretical models which we have developed.

We derived a theoretical model for the three-point third-order velocity correlation for homogeneous, isotropic turbulence in the inertial range. This model is shown be a good representation of DNS data, and it is used to construct optimal quadratic subgrid models for LES of forced isotropic turbulence with results which agree well with theory and DNS. The model can also be filtered to determine the filtered two-point third-order correlation, which describes energy transfer among filtered (large) scales in LES.

LES of wall-bounded flows with unresolved wall layers commonly exhibit good prediction of mean velocities and significant over-prediction of streamwise component energies in the near-wall region. We developed improved models for the nonlinear term in the filtered Navier-Stokes equation which result in better predicted streamwise component energies. These models involve (1) Reynolds decomposition of the nonlinear term and (2) evaluation of the pressure term, which removes the divergent part of the nonlinear models. These considerations significantly improved the performance of our optimal models, and we expect them to apply to other subgrid models as well.

Table of Contents

List of Tables

List of Figures

Nomenclature

The following lists of abbreviations and symbols are arranged in approximately the order they are introduced in the dissertation. Not all abbreviations and symbols are listed here but only the ones that are used across multiple sections.

Abbreviations

DNS	Direct Numerical Simulation
LES	Large Eddy Simulation
RANS	Reynolds Averaged Navier Stokes
OLES	Optimal Large Eddy Simulation
$L20$	Simplest Linear Stencil, equation (4.35), figure (4.10a)
$L22$	Simple Linear Stencil, equation (4.34), figure (4.10b)
LRS	Reynolds Stress Matching Stencil, figure (4.10c)
$Q22$	Simple Quadratic Stencil, equation (4.36), figure (4.10b)
$Q\gamma$	Mean-Corrected Quadratic Model for Production, section 4.3.4.4

Superscripts and Subscripts

$\widetilde{[\cdot]}$	filtered, or volume filtered
$\overline{[\cdot]}$	surface filtered
$\langle[\cdot]\rangle$	expected value
$[\cdot]'$	fluctuating part

$[\cdot]^v$	cell indexing
$[\cdot]^s$	face indexing
$[\cdot]^{\pm k}$	cell or face in $\pm k$ direction
$[\cdot]^{mod}$	model
$[\cdot]^{mod}_{std}$	standard model
$[\cdot]^{opt}$	optimal model
$\underline{[\cdot]}_k$	average of two adjacents cells or faces in k direction, equation (4.16)

Greek Symbols

ρ	density
ν	kinematic viscosity
τ_{ij}	subgrid stress tensor
Δ	filter width
Ψ^n	Scalar basis functions for three-point third-order correlation
ϵ	dissipation rate
λ	Taylor microscale
η	Kolmogorov scale
γ	non-dimensional filter width
δ	channel half width, or shear flow thickness
δ_ν	viscous or wall scale
τ_w	wall shear stress
ϕ	standard pressure model
$\tilde{\partial}_k$	difference of two adjacent cells or faces in k direction, equation (4.10)

Latin Symbols

u_i	continuous velocity field
p	continuous pressure field
G	filter kernel
F	filtering with discretization
$\mathbb{U}$	continuous space of Navier Stokes solutions
w_i	discrete LES field
$\mathbb{W}$	discrete space of LES solutions
M	generic modeled term
m	generic model
A_k	generic model coefficients
E_k	generic model events
S	face, or area of face
V	cell, or volume of cell
$\mathcal{N}_i^s$	nonlinear flux
$\mathcal{P}_i^s$	pressure force
$\mathcal{V}_i^s$	viscous flux
$\mathcal{M}^s$	mass flux
$\mathcal{A}_i$	constant model coefficient
$\mathcal{L}_{ij}$	linear model coefficient
$\mathcal{Q}_{ijk}$	quadratic model coefficient
$\mathbb{R}_{ij}$	two-point second-order correlation

$\mathbb{S}_{ijk}$	two-point third-order correlation
$\mathbb{T}_{ijk}$	three-point third-order correlation
$\mathbb{F}_{ijkl}$	four-point fourth-order correlation
$\mathbb{T}^n_{ijk}$	basis function of three-point third-order correlation
$\mathbb{T}^{\parallel}_{ijk}$	three-point third-order correlation with points colinear
$\mathbb{T}^{\perp}_{ijk}$	three-point third-order correlation with separations orthogonal
S_p	longitudinal structure function of p-order
$\mathbf{r}, \mathbf{s}, \mathbf{t}$	separation vectors
q	magnitude of largest separation, $max(r, s, t)$
$\mathbb{Q}_{ijk}$	subgrid stress filter-velocity correlation
$\tilde{\mathbb{S}}_{ijk}$	two-point third-order correlation of filtered field
$\tilde{S}_p$	longitudinal structure function of p_{th} order for filtered field
U	mean velocity
P	mean pressure
u, v, w	components of velocity (streamwise, wall-normal, spanwise)
x, y, z	coordinate directions (streamwise, wall-normal, spanwise)
w_i^*	auxiliary velocity field
D_{ij}	discrete curl-free projection operator, equation (4.27)
P_{ij}	discrete divergence-free projection operator, equation (4.28)

Chapter 1

Introduction

Most flows in nature and engineering are turbulent, and turbulence generally has a large impact on the behavior of the flow. For example, approximately 50% of drag on commercial aircraft results from skin friction in turbulent boundary layers [42]. It is therefore important to be able to predict the effects of turbulence in such flows. Turbulent flows may be distinguished from laminar flows in several ways. Turbulent flows occur at higher Reynolds numbers, have higher dissipation and higher mixing rates than laminar flows. They exhibit fluctuations over a broad range of length and time scales. Turbulent flows are also chaotic; that is, perturbations on average, grow exponentially in time.

The Navier-Stokes equations are known to be an excellent model of the turbulence phenomenon [52]. For an incompressible, Newtonian fluid, the Navier-Stokes equations are given by

$$\frac{\partial u_i}{\partial t} = -\frac{\partial u_i u_j}{\partial x_j} - \frac{1}{\rho}\frac{\partial p}{\partial x_i} + \nu \frac{\partial^2 u_i}{\partial x_j \partial x_j} \tag{1.1}$$

$$\frac{\partial u_i}{\partial x_i} = 0 \tag{1.2}$$

where u_i is the velocity field, p is the pressure field, x_i and t are the space and time dimensions, ρ is the fluid density, and ν is the kinematic viscosity of the fluid.

Equations (1.1) and (1.2) are expressions of momentum and mass conservation, respectively.

Unfortunately, analytical solutions to these equations have been found only in very special circumstances. In fact, a million dollar prize awaits anyone who can prove existence and smoothness of Navier-Stokes solutions [20]. Therefore, scientists and engineers have resorted to making physical measurements of turbulent flows and/or to solving the Navier-Stokes equations numerically. In the subsections below, the issues surrounding the numerical simulation and modeling of turbulence are discussed briefly and the large eddy simulation (LES) approach to be pursued here is introduced.

1.1 Turbulence Simulation and Modeling

There are three levels of turbulence simulation: Direct Numerical Simulation (DNS), Large Eddy Simulation (LES), and Reynolds-Averaged Navier Stokes (RANS). In DNS, the Navier-Stokes equations are solved on spatial and temporal grids fine enough to resolve all scales of turbulence. LES employs a coarser grid and only solves for the large-scale turbulence, while the effects of the small-scale turbulence are modeled. RANS only solves for the "mean" flow, while all of the turbulence is modeled.

For any given turbulent flow problem, the most straightforward, accurate, and computationally expensive method of simulation is DNS. The cost of a DNS grows rapidly with Reynolds number (Re^3 for isotropic turbulence [52]), so its application is limited to moderate Reynolds number flows in simple geometries. See [45] for a review of DNS of turbulent flows.

On the other hand, the cost of RANS increases only modestly with Reynolds number [52]. However, RANS models are notoriously unreliable, and generally unable to represent the effects of turbulence over a wide range of flows [19]. The difficulty is that the largest scales of turbulence have the greatest effects on the flow, but are highly dependent on the flow configuration. RANS models are poorly suited to represent the effect of this flow dependent large-scale turbulence.

By simulating the dynamics of the flow-dependent large-scale turbulence, and modeling only the effects of the small scales, LES seeks to avoid the reliability problems with RANS and the cost escalation of DNS [52]. Modeling the small scales of turbulence is a promising endeavor, since these small scales exhibit universal behavior over a wide range of flows [64]. However, for LES to fulfill its promise as a widely applicable, computationally tractable turbulence modeling approach, a number of shortcomings of current LES formulations and models need to be addressed [27, 34, 53], which is the goal of the current research.

1.2 Large Eddy Simulation

In LES, the large scales (to be simulated) and the small scales (to be modeled) are distinguished by a filter operator. Filters are usually defined to be linear operators, expressed in terms of a filter kernel $G(x, x')$ as

$$\tilde{u}(x) = \int G(x, x')u(x')dx' \tag{1.3}$$

where $\tilde{u}$ is the filtered u, also called the resolved or large scale u. Common filters include the spectral cut-off filter which is simply a Fourier truncation, the box filter which averages u over finite-sized volumes, and the Gaussian filter in which G is a gaussian in $(x - x')$. For an overview of LES filters, see [52].

Applying the filter to the Navier-Stokes equation (1.1) produces:

$$\frac{\partial \tilde{u}_i}{\partial t} = -\frac{\partial \tilde{u}_i \tilde{u}_j}{\partial x_j} - \frac{\partial \tilde{p}}{\partial x_i} + \frac{1}{Re} \frac{\partial^2 \tilde{u}_i}{\partial x_j \partial x_j} - \frac{\partial \tau_{ij}}{\partial x_j} + C_i \tag{1.4}$$

where

$$\tau_{ij} = \widetilde{u_i u_j} - \tilde{u}_i \tilde{u}_j \tag{1.5}$$

and C_i is zero if filtering commutes with spatial differentiation. The "subgrid stress" tensor τ_{ij} is the quantity most often modeled in LES.

The usual approach to LES modeling involves approximating the subgrid stress τ_{ij} in terms of the large-scale velocities $\tilde{u}$. The most popular model was formulated by Smagorinsky [61]

$$\tau_{ij} \approx -2\nu_T S_{ij} \tag{1.6}$$

where $S_{ij} = \frac{1}{2}\left(\frac{\partial \tilde{u}_i}{\partial x_j} + \frac{\partial \tilde{u}_j}{\partial x_i}\right)$ is the strain rate of the large scales, $\nu_T = (C_S \Delta)^2 |S|$ is called the eddy viscosity, C_S is a constant, and Δ is the characteristic length of the filter.

Germano et al proposed a dynamic procedure for determining C_S, assuming similarity over two filter scales [22], which significantly improved on the Smagorinsky model. Leveque et al [40] proposed that mean shear be subtracted out of S_{ij} in the Smagorinsky model, which is similar to our stategy of using Reynolds decomposition in modeling wall-bounded turbulence (see section 4.3.3.6). Other noteable models include the scale-similarity model by Bardina et al [7], a model based on the eddy-damped quasi-normal Markovian (EDQNM) approximation by Chollet and Lesieur [14], monotone integrated large eddy simulation (MILES) by Boris et al [11], the stretched vortex model by Misra and Pullin [44], and the variational multiscale (VMS) model by Bazilevs et al [8]. For an overview of current LES turbulence models, see [39, 43].

1.3 Challenges in LES Modeling

While there are a wide variety of models available, they share several shortcomings that need to be addressed for LES to be a useful turbulence simulation tool. The first issue is that LES of wall-bounded flows fail to produce accurate results when the near-wall layer is not resolved (when the filter scale is much larger than the viscous length scale) [50]. This is primarily because LES models are usually built on assumptions of small-scale homogeneity and isotropy, and the existence of an inertial range, all of which are invalid near the wall. A common symptom of channel flow LES with unresolved wall layers is high streamwise and/or low wall-normal velocity variances [5, 12, 16, 48]. The second issue is the interaction of modeling errors and numerical discretization errors [23, 33]. All the subgrid models mentioned above, except MILES and VMS, were formulated without considering the discretization and numerical methods used in the LES. Optimal LES (OLES) pursued here addresses both of these issues.

In this dissertation, Chapter 2 will introduce the OLES framework. Chapter

3 will describe modeling the three-point third-order correlation for homogeneous isotropic turbulence, a statistic necessary for developing optimal quadratic models. It is also useful in the analysis of LES, since it represents transfer of energy among the filtered scales. Chapter 4 will describe the use of OLES to model wall-bounded flows with unresolved wall layers, which as explained above is an area of ongoing research. It will be shown that decomposing the nonlinear term in the filtered Navier-Stokes equation and considering it's effect on pressure are important to constructing accurate models in the near-wall region. Chapter 5 will discuss conclusions and future work.

Chapter 2

Optimal LES

Optimal LES is an LES modeling approach formulated to minimize the error in representing an “ideal” LES evolution. It is generally applicable provided only that the statistical information required to evaluate it is available. In the discussion below, this LES modeling formalism is briefly recalled.

2.1 Ideal LES

Ideal LES starts from the premise that the LES representation is fundamentally discrete, since this is what is required for computation. As a result LES fields are missing small-scale information. This fundamentally discrete representation is what Pope [53] classifies as “numerical LES”. It stands in contrast to “physical LES” where the LES equation is considered a partial differential equation and one seeks numerical solutions that converge to the solution of the PDE.

In the usual LES notion of filtering introduced briefly in Section 1.2, the filter operator does not necessarily remove information; it is then the sampling or discretization performed for numerical computation that discards the small-scale information. For example, the Gaussian filter, in which G in equation (1.3) is a Gaussian, is formally invertible; that is, a turbulent velocity field u on a continuous domain can be Gaussian filtered to get $\tilde{u}$ on a continuous domain, and $\tilde{u}$

can be inverse Gaussian filtered to get back u. Of course, inverting the filter is ill-conditioned, but in principle, with arbitrary precision computation the filter is invertible. However, $\tilde{u}$ sampled at a finite number of points cannot be inverse filtered; information has been lost.

For the current development, it is convenient to define the filter operator F to include the discretization used for numerical representation. F then maps the infinite dimensional space $\mathbb{U}$ to the finite-dimensional space $\mathbb{W}$, where $u \in \mathbb{U}$ is the real turbulent velocity field and $w \in \mathbb{W}$ is the LES field. It can be shown [34, 52] that if an LES field w evolves according to a conditional average

$$\frac{dw}{dt} = \left\langle \frac{d\tilde{u}}{dt} | \tilde{u} = w \right\rangle \tag{2.1}$$

then (1) multi-point, single-time statistics of w will be the same as those of $\tilde{u}$, and (2) the mean-square discrepency between the short-time dynamics of the LES and filtered turbulence $\langle (\frac{dw}{dt} - \frac{d\tilde{u}}{dt})^2 | \tilde{u} = w \rangle$ is minimized. Because correct large-scale statistics and accurate short-time dynamics is the most that can be expected from a deterministic LES evolution, equation (2.1) is called the "ideal LES" [34]. It is the best possible LES evolution.

An essential feature of ideal LES is that it is characterized statistically. This is appropriate since without the small-scale information, one cannot know exactly how the large scales will evolve. Because F has mapped turbulent fields in $\mathbb{U}$ to a finite-dimensional space $\mathbb{W}$, for any $w \in \mathbb{W}$, there are many (an infinite number) $u \in \mathbb{U}$ for which $\tilde{u} = w$. Each of these u will have a different evolution (time derivative), so that there is a distribution of possible time derivatives associated with each $w \in \mathbb{W}$. The ideal LES evolution (2.1) is simply the average over this distribution. Figure (2.1) illustrates Ideal LES.

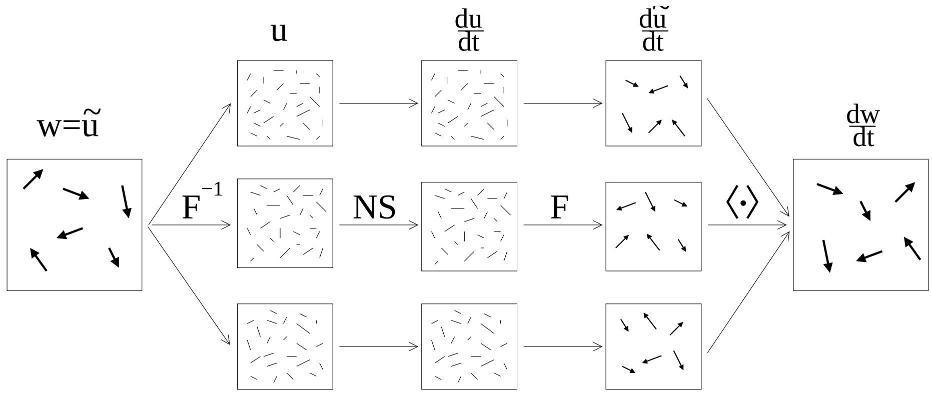

Figure 2.1: Ideal LES: the ideal evolution of the LES field w corresponds to the average over all possible evolutions of corresponding continuous fields u filtered. F is the filtering/discretization operation, NS is the Navier-Stokes equation, and $\langle\cdot\rangle$ is the average.

It is also possible to formulate ideal LES models for terms on the right hand side of the filtered Navier-Stokes equations. In what follows we will consider a generic term M and the model for it m. The ideal model for M is

$$m = \langle M | \tilde{u} = w \rangle \tag{2.2}$$

In general, formulating ideal LES models in this way is equivalent to equation (2.1), since they are terms from the same filtered Navier Stokes equation. It may be useful to formulate the modeling problem in terms of some model term like this, if the resulting conditional expectation is simpler to represent or approximate.

Unfortunately, the effective number of conditions represented in the conditional expectations in (2.1) and (2.2) is the dimension of the space $\mathbb{W}$, which will generally be many thousands or millions. It is thus not practical to evaluate these conditional averages. Instead, we seek to approximate the ideal LES with what we call "optimal LES".

2.2 Optimal LES

An "optimal" model formally approximates the ideal model using linear stochastic estimation [1–4]. First, one postulates the form of the model m as a function of w:

$$m = \sum_k A_k E_k \tag{2.3}$$

where E_k is a vector of the so-called events based on the velocity field w, and A_k is the corresponding vector of model coefficients. Note that in linear stochastic estimation, the model is linear in the coefficients A_k, but not necessarily in the LES state variables w. E_k allows the model m to be a function of any combination of products of w over different locations. The coefficients A_k are determined by minimizing the mean square difference between the model and the exact term, $\left\langle (M-m)^2 \right\rangle$, with respect to the model coefficients. While this optimality condition is written in terms of the exact term M, it can be shown [66] that the mean square error (MSE) of the optimal model relative to the ideal model:

$$MSE = \langle (\langle M | \tilde{u} = w \rangle - m)^2 \rangle \tag{2.4}$$

is also minimized. This error relative to the ideal LES is of primary concern since it is not possible to represent M more accurately than the ideal LES does. The optimality condition used to determine the linear coefficients is:

$$\langle mE_k \rangle = \langle ME_k \rangle, \tag{2.5}$$

which is a linear algebraic equation for the coefficients A_k.

Notice that nowhere in the development of ideal/optimal LES did we assume isotropy, homogeneity, existence of an inertial range, or scale similarity. Optimal models simply do what the statistics say they should do, which makes optimal models much more generalizable than other existing LES models. In addition, optimal models may be constructed to account for discretization errors associated with standard numerical methods. Optimal models may be seen as *customized* numerical methods for most accurately replicating turbulence statistics. This is important, since Ghosal [23] found that for low-order discretization schemes, such as finite-volume methods, truncation errors may be the same order of magnitude as subgrid modeling errors.

Another important property of the optimal LES model arises trivially from the optimality condition (2.5). The correlation of the model with the events E_k matches that for the actual term, when evaluated for filtered real turbulence, that is *a priori*. If the correlations $\langle ME_k \rangle$ include statistical quantities that are dynamically significant, then *a priori*, the model represents these quantities well. Appendix D shows how the simplest optimal flux model will match *a priori* statistics for the corresponding term in the component energy equations. Furthermore it was found in [66] that when the optimal model was formulated so that the correlation $\langle ME_k \rangle$ includes critical terms in the Reynolds stress transport equations, then the model produced an accurate LES. One of the challenges in optimal LES modeling is determining an appropriate dependence for the model, that is the event vector E_k. This property of matching the correlations $\langle ME_k \rangle$ can provide guidance when the dynamically important model statistics are understood.

The second challenge in optimal LES is the determination of the statistics appearing in (2.5), which are inputs to the modeling process. These statistics are multi-point correlations between M and w's. The theoretical determination of these input statistics for homogeneous turbulence is described in chapter 3. However, to explore the properties and performance of OLES models without the uncertainties associated with modeling the statistical inputs, much of the previous work on optimal LES [9, 37, 66, 68] has used statistical inputs determined from DNS.

2.3 Previous Optimal LES Studies

Optimal LES has been performed for forced isotropic turbulence, with Fourier spectral methods by Langford and Moser [37], and with finite-volume method by Zandonade et al [68]. Both showed good agreement with DNS data, and both performed similar or better than the dynamic Smagorinsky model [22]. Of particular relevance to the current study, Zandonade et al showed the viability of optimal models based on a finite-volume discretization (see section 2.4). They showed that small local stencils (2 or 4 adjacent cells) were sufficient to model the nonlinear term in isotropic turbulence, and that for small stencils, the optimal quadratic term is approximately the standard finite-volume reconstruction of the nonlinear term. Zandonade et al also found that care was needed in constructing optimal models based on poor estimates of the correlations, as the resulting models could be numerically unstable.

Optimal LES has also been performed for channel flows by Volker et al [66] and by Bhattacharya et al [9]. Volker et al used Fourier spectral representation for the wall-parallel directions and Chebychev tau representation for the wall-normal direction, with standard no slip walls. Bhattacharya et al used Fourier spectral representation in all directions and a special wall treatment involving buffer regions outside the channel walls, where the kinetic energy is minimized to solve for the wall stress. Both optimal LES results compared well with DNS data, and Bhattacharya's optimal model performed significantly better than dynamic Smagorinsky. Volker et al showed the importance of constructing models which have the right form and dependencies, and which would *a priori* match terms from the resolved Reynolds stress equation. Bhattacharya et al showed that good results are acheiveable without resolving the near wall turbulence. This is remarkable because the near-wall layer of a wall-bounded shear flow dominates the production and dissipation of turbulence. That these processes need not be resolved in a properly formulated LES is encouraging for the development of tractible LES models for high Reynolds number wall-bounded turbulence. Bhattacharya et al also showed that, contrary to common perception, it was important near the wall that the subgrid model account for more than the dissipation of energy. In particular, dispersive and anti-dissipative properties in the optimal model are shown to be important.

2.4 Finite Volume Optimal LES

In finite volume OLES, a finite volume discretization serves as the filter mapping Navier-Stokes solutions to a finite-dimensional representation. In this case, the LES state variables represent the velocities averaged over discrete volumes. The LES evolution equations are then determined from the volume averaged Navier-Stokes equations given by:

$$V^v \frac{d\tilde{u}_i^v}{dt} = -\sum_s \mathcal{N}_i^s - \sum_s \mathcal{P}_i^s + \sum_s \mathcal{V}_i^s \tag{2.6}$$

$$\sum_s \mathcal{M}^s = 0 \tag{2.7}$$

where $\tilde{u}_i^v$ is the velocity averaged over the cell v, and $\mathcal{M}^s$, $\mathcal{N}_i^s$, $\mathcal{P}_i^s$ and $\mathcal{V}_i^s$ are the mass flux, nonlinear flux, pressure force and viscous flux respectively for the face s. The sums in (2.6) are over the faces of the cell v. The quantities appearing in (2.6) are defined as:

$$\tilde{u}_i^v = \frac{1}{V^v}\int_v u_i \, \mathrm{d}\mathbf{x} \tag{2.8}$$

$$\mathcal{N}_i^s = \int_s u_i u_j n_j^s \, \mathrm{d}\mathbf{x} \tag{2.9}$$

$$\mathcal{P}_i^s = \int_s p n_i^s \, \mathrm{d}\mathbf{x} \tag{2.10}$$

$$\mathcal{V}_i^s = \int_s \nu \frac{\partial u_i}{\partial x_j} n_j^s \, \mathrm{d}\mathbf{x} \tag{2.11}$$

$$\mathcal{M}^s = \int_s u_i n_i^s \, \mathrm{d}\mathbf{x} \tag{2.12}$$

where u_i is the turbulent velocity and n_j^s is the outward-pointing unit normal to the face s. As indicated, the integrals are over a cell v or one of its faces s. V^v is the volume of the cell.

To distinguish the simulation quantities in an LES from the filtered real turbulence, the symbol w_i^v will be used to represent the LES variables. The goal, of course, is for the dynamics and statistics of w_i^v to approximate those of $\tilde{u}_i^v$ as closely as possible. The evolution equation for w_i^v will be the same as that for $\tilde{u}_i^v$ (2.6), with the fluxes replaced by models.

$$V^v \frac{dw_i^v}{dt} = -\sum_s \mathcal{N}_i^{s,mod} - \sum_s \mathcal{P}_i^{s,mod} + \sum_s \mathcal{V}_i^{s,mod} \tag{2.13}$$

In the context of OLES, $\mathcal{N}_i^{s,mod}$, $\mathcal{P}_i^{s,mod}$, $\mathcal{V}_i^{s,mod}$, and $\mathcal{M}^{s,mod}$ must be modeled as functions of w. The modeling of $\mathcal{N}_i^s$ is most closely related to standard LES modeling. In light of the quadratic nature of this term, it makes sense to formulate an optimal LES model for this term that is quadratic in the velocity state variables. Zandonade et al [68] found that for small stencils, with constrained quadratic dependence, the quadratic terms in the optimal model were consistent with standard finite volume approximations to the nonlinear terms. More general optimal quadratic terms were considered by Moser et al [47], who found that the quadratic part of the optimal operator was a consistent second order finite volume scheme. However, its spectral characteristics were different from common schemes. Given Zandonade's experience, the starting point for the modeling of $\mathcal{N}_i^s$ pursued in chapter 4 is a quadratic part consisting of a standard staggered grid finite volume representation. In this case, the only thing that distinguishes the the optimal flux model from a finite volume reconstruction scheme is the linear term, which in Zandonade et al [68] is purely dissipative.

The viscous fluxes $\mathcal{V}_i^s$ can be modeled as linear in w, and in many high

Reynolds number turbulent flows, away from walls, the viscous flux can be neglected, as was done by Moser et al [47]. In [68], it was found that in isotropic turbuence, it appeared to be sufficient to represent the viscous flux as a standard finite volume approximation. As was shown by Langford & Moser [36], it appears to be sufficient to approximate the mass fluxes $\mathcal{M}^s$ consistent with standard finite volume methods, and with a staggered grid arrangement, use the continuity constraint to determine the pressure in the usual way. This was pursued in isotropic turbulence [47, 68], with excellent results. The observations have informed our starting point for modeling the viscous and pressure terms in the current effort, which is to formulate them as standard finite volume schemes.

Chapter 3 will describe the modeling of the three-point third-order velocity correlation for homogeneous isotropic turbulence. This correlation, along with the second-order and fourth-order correlations, provide the theory-based statistics necessary to construct optimal quadratic models for finite-volume LES of forced isotropic turbulence.

Going from isotropic turbulence models, described above, to models for wall-bounded turbulence in chapter 4, we shall see that models for the viscous and nonlinear terms need to be extended or generalized. The standard approximation for viscous flux is no longer sufficient near the walls, so additional optimal linear terms are added. The nonlinear flux model is improved by generalizing the quadratic terms from standard to optimal.

Chapter 3

Theory-Based OLES

Previous optimal LES used statistics from DNS data to construct optimal models. In order for an LES model to actually be predictive, we must be freed from using DNS data. That is the motivation for constructing optimal models based on turbulence theory. In the following chapter, theoretically-based optimal models based on small-scale isotropy for use with finite-volume discretizations are presented.

3.1 OLES and Multi-Point Correlations

Consider the finite-volume LES equation (2.13) for infinite Reynolds number homogeneous isotropic turbulence. Optimal models for this flow and representation will be constructed using stochastic estimation as described in 2.1. The resulting models and modeling approaches will be applicable to any flow in which the assumptions of small-scale isotropy and homogeneity are valid. In this case, the viscous term $\mathcal{V}_i^s$ is zero due to the infinite Reynolds number. For the pressure model $\mathcal{P}_i^{s,mod}$, the model approach described by Langford & Moser [36] is taken, which amounts to using the standard staggered-grid finite-volume formulation for enforcing the approximate divergence-free condition of the resolved velocities. The only term in (2.13) that requires further modeling is thus the nonlinear flux (2.9). The dependence of the optimal model on the finite-volume averaged velocities w is postulated to be quadratic since the nonlinear flux term is itself quadratic in u. The resulting optimal model is

$$\mathcal{N}_i^{s,mod} = \mathcal{A}_i(s) + \sum_{v_1} \mathcal{L}_{ij}(s, v_1) w_j^{v_1} + \sum_{v_1, v_2} \mathcal{Q}_{ijk}(s, v_1, v_2) w_j^{v_1} w_k^{v_2} \tag{3.1}$$

where $\mathcal{A}_i(s)$ is a constant term, $\mathcal{L}_{ij}(s, v)$ are the linear coefficients, $\mathcal{Q}_{ijk}(s, v_1, v_2)$ are the quadratic coefficients, v_1 and v_2 are the cells over which the velocities are averaged to obtain $w_j^{v_1}$ and $w_k^{v_2}$ respectively, and s is the face through which the flux is being modeled.

The statistics needed to solve for optimal model coefficients can be expressed as volume and surface integrals of the second-, third-, and fourth-order velocity correlations:

$$\mathbb{R}_{ij}(\mathbf{r}^1) = \left\langle u_i'(\mathbf{x}) u_j'(\mathbf{x} + \mathbf{r}^1) \right\rangle \tag{3.2}$$

$$\mathbb{T}_{ijk}(\mathbf{r}^1, \mathbf{r}^2) = \left\langle u_i'(\mathbf{x}) u_j'(\mathbf{x} + \mathbf{r}^1) u_k'(\mathbf{x} + \mathbf{r}^2) \right\rangle \tag{3.3}$$

$$\mathbb{F}_{ijkl}(\mathbf{r}^1, \mathbf{r}^2, \mathbf{r}^3) = \left\langle u_i'(\mathbf{x}) u_j'(\mathbf{x} + \mathbf{r}^1) u_k'(\mathbf{x} + \mathbf{r}^2) u_l'(\mathbf{x} + \mathbf{r}^3) \right\rangle \tag{3.4}$$

For instance, $\left\langle \mathcal{N}_i^s \tilde{u}_l^{v_3\prime} \right\rangle$, the correlation between the nonlinear flux and a volume averaged velocity, is given by the five-dimensional integral

$$\left\langle \mathcal{N}_i^s \tilde{u}_l^{v_3\prime} \right\rangle = \frac{1}{v_3} \int_{v_3} \int_s \left\langle u_l'(\mathbf{x}^3) u_i'(\mathbf{x}) u_s'(\mathbf{x}) \right\rangle \, d\mathbf{x} \, d\mathbf{x}^3 \tag{3.5}$$

The integrand is actually the third-order correlation (3.3) where two of the points are collocated $\mathbb{T}_{isl}(0, \mathbf{x}^3 - \mathbf{x})$. All the correlations appearing in the optimality conditions can be similarly expressed.

3.2 Kolmogorov Inertial Range Theory

When the Reynolds number is sufficiently large and the sub-grid turbulence is approximately homogeneous, the small-scale turbulence will exhibit a Kolmogorov's inertial range, which can be used to develop theoretical expansions for the correlations (3.2,3.3,3.4). Kolmogorov derived a simple expression for the second-order structure function $S_2(r) = \langle (u_{\|}(\mathbf{x}+\mathbf{r}) - u_{\|}(\mathbf{x}))^2 \rangle = C_2(\epsilon r)^{2/3}$ [30], where $C_2 \approx 2.0$ (determined empirically). He further employed the Karman-Howarth [67] equation relating S_2 to S_3 to derive an expression for the third-order structure function $S_3(r) = \langle (u_{\|}(\mathbf{x}+\mathbf{r}) - u_{\|}(\mathbf{x}))^3 \rangle = C_3(\epsilon r)$, where $C_3 = \frac{4}{5}$ is determined analytically [29].

The constraints of isotropy and continuity allow the two-point, second-order correlation $\mathbb{R}$ to be determined from Kolmogorov's expression for S_2 with the result:

$$\mathbb{R}_{ij}(\mathbf{r}) = u^2\delta_{ij} + \frac{C_2}{6}(\epsilon r)^{2/3}\left(\frac{r_i r_j}{r^2} - 4\delta_{ij}\right) \tag{3.6}$$

Invoking the quasi-normal approximation, then allows the four-point, fourth-order correlation $\mathbb{F}$ to be expressed in terms of $\mathbb{R}$

$$\mathbb{F}_{ijkl}(\mathbf{r}^1,\mathbf{r}^2,\mathbf{r}^3) \approx \mathbb{R}_{ij}(\mathbf{r}^1)\mathbb{R}_{kl}(\mathbf{r}^3-\mathbf{r}^2)+\mathbb{R}_{ik}(\mathbf{r}^2)\mathbb{R}_{jl}(\mathbf{r}^3-\mathbf{r}^1)+\mathbb{R}_{il}(\mathbf{r}^3)\mathbb{R}_{jk}(\mathbf{r}^2-\mathbf{r}^1) \tag{3.7}$$

The quasi-normal approximation is the assumption that even-order correlations are related to each other as would be the case for a Gaussian process. In turbulence, odd-order correlations are certaintly not as in a Gaussian process because they are not zero. Quasi-normal approximations in turbulence are notorious because in two-point closure models they lead to unrealizable results [38]. However, DNS data indicates that the quasi-normal approximation is a good representation of fourth-order correlations [65], and its use in optimal LES models cannot lead to realizability problems.

As with the two-point second-order correlation, isotropy, continuity and the Kolmogorov expression for S_3 allow the *two-point* third-order correlation tensor to be written:

$$\mathbb{T}_{ijk}(0,\mathbf{r}) = \frac{\epsilon}{15}\left(\delta_{ij} r_k - \frac{3}{2}(\delta_{ik} r_j + \delta_{jk} r_i)\right). \tag{3.8}$$

However, these considerations are not sufficient, by themselves, to develop a model for the three-point third-order correlation.

3.3 Three-Point Third-Order Correlation

The three-point, third-order correlation $\mathbb{T}$ (a third-rank tensor function of two vectors) is a more complex quantity. Determining an analytical expression for $\mathbb{T}$ has been one of the major accomplishments of this dissertation. The derivation follows. A similar derivation can be found in [13].

3.3.1 The Fourier Transform of $\mathbb{T}$

Proudman and Reid [54] determined a general form for the Fourier transform of $\mathbb{T}$ in both $\mathbf{r}$ and $\mathbf{s}$ (this is a six-dimensional Fourier transform). For an incompressible, homogeneous, isotropic turbulence, the most general possible form for the Fourier transform Φ of $\mathbb{T}$ is given by

$$\Phi_{ijk}(\boldsymbol{\rho},\boldsymbol{\sigma}) = \Delta_{im}(\boldsymbol{\tau})\Delta_{jn}(\boldsymbol{\rho})\Delta_{kp}(\boldsymbol{\sigma})\left[\delta_{np}\rho_m\phi + \delta_{mp}\sigma_n\phi_1 + \delta_{mn}\rho_p\phi_2 + \rho_m\sigma_n\rho_p\zeta\right] \tag{3.9}$$

where the wavevectors $\boldsymbol{\rho}$, $\boldsymbol{\sigma}$ and $\boldsymbol{\tau}$ are interrelated $\boldsymbol{\rho}+\boldsymbol{\sigma}+\boldsymbol{\tau}=0$, and $\Delta_{im}(\boldsymbol{\rho}) = \delta_{im} - \rho_i\rho_m/\rho^2$ is the divergence-free projector. The scalar functions ϕ, ϕ_1, ϕ_2 and ζ depend only on the magnitudes of the wavevectors. For an outline of the derivation of (3.9), see Appendix B. Symmetries in the tensor $\mathbb{T}$ imply symmetries among scalar functions:

$$\phi(\rho,\sigma,\tau) = -\phi(\sigma,\rho,\tau) = \phi_1(\tau,\rho,\sigma) = \phi_2(\rho,\tau,\sigma) \tag{3.10}$$

Proudman & Reid[54] also analyze the dynamic equation for Φ in the context of the quasi-normal approximation to find independent (model) dynamic equations for ϕ and ζ. These equations imply that for stationary turbulence, ζ is zero. We will thus assume that $\zeta=0$, and with the symmetries expressed in (3.10), Φ is determined through (3.9) by a single scalar function ϕ of ρ, σ and τ. We start with this form in developing our real-space model for $\mathbb{T}$.

3.3.2 Inertial-range model of $\mathbb{T}$

To construct a model for the three-point third-order correlation, a general tensor form consistent with (3.9) is derived, and then the scalar function appearing in the expression is selected for consistency with the Kolmogorov 4/5 law.

3.3.3 A general form for $\mathbb{T}$ in real space

To develop the analog of (3.9) in real space, it will be inverse Fourier transformed to yield an expression for $\mathbb{T}$. However, to simplify the computations in real-space, it is convenient to recast the expression as

$$\Phi_{ijk}(\boldsymbol{\rho},\boldsymbol{\sigma}) = \tilde{\Delta}_{im}(\boldsymbol{\tau})\tilde{\Delta}_{jn}(\boldsymbol{\rho})\tilde{\Delta}_{kp}(\boldsymbol{\sigma})\big[\delta_{np} i\rho_m \tilde{\phi}(\rho,\sigma,\tau) + \delta_{mp} i\sigma_n \tilde{\phi}(\sigma,\tau,\rho) + \delta_{mn} i\rho_p \tilde{\phi}(\rho,\tau,\sigma)\big] \tag{3.11}$$

where $\tilde{\Delta}_{im}(\boldsymbol{\rho}) = \rho^2\delta_{im} - \rho_i\rho_m$ is a modified divergence free operator, and $\tilde{\phi}(\rho,\sigma,\tau) = -i\phi(\rho,\sigma,\tau)/(\rho\sigma\tau)^2$ is a modified scalar function that has the same symmetry properties as ϕ. The advantage of this form is that the inverse Fourier transform will not give rise to inverse Laplacian operators. An inverse Fourier transform of (3.11) yields

$$\mathbb{T}_{ijk}(\mathbf{r},\mathbf{s}) = \mathcal{P}^t_{im}\mathcal{P}^s_{jn}\mathcal{P}^r_{kp}[\delta_{np}\partial^s_m\psi(r,s,t) + \delta_{mp}\partial^r_n\psi(t,r,s) + \delta_{mn}\partial^s_p\psi(t,s,r)] \tag{3.12}$$

which is thus our general expression for $\mathbb{T}$ in stationary, homogeneous, isotropic incompressible turbulence. Here, the third separation vector is $\mathbf{t} = \mathbf{r} - \mathbf{s}$, the scalar function $\psi(r,s,t)$ is the inverse Fourier transform of $\tilde{\phi}$, and r, s and t are the magnitudes of the separation vectors $\mathbf{r}$, $\mathbf{s}$ and $\mathbf{t}$ respectively. The operators appearing in (3.12) are defined:

$$\partial^r_i \equiv \left.\frac{\partial}{\partial s_i}\right|_{\mathbf{r}} \tag{3.13}$$

$$\partial^s_i \equiv \left.\frac{\partial}{\partial r_i}\right|_{\mathbf{s}} \tag{3.14}$$

$$\partial^t_i \equiv -\left.\frac{\partial}{\partial r_i}\right|_{\mathbf{s}} - \left.\frac{\partial}{\partial s_i}\right|_{\mathbf{r}} \tag{3.15}$$

$$\mathcal{P}^\alpha_{ij} \equiv \delta_{ij}\partial^\alpha_k\partial^\alpha_k - \partial^\alpha_i\partial^\alpha_j \tag{3.16}$$

It is straight-forward to confirm that the expression for $\mathbb{T}$ in (3.12) satisfies the relevant symmetry and continuity constraints for the third-order three-point correlation, provided that

$$\psi(r, s, t) = -\psi(s, r, t), \tag{3.17}$$

which is the analogue of (3.10). The constraints on $\mathbb{T}$ are:

$$\partial_i^t \mathbb{T}_{ijk} = \partial_j^s \mathbb{T}_{ijk} = \partial_k^r \mathbb{T}_{ijk} = 0 \tag{3.18}$$

$$\mathbb{T}_{ijk}(\mathbf{r}, \mathbf{s}) = \mathbb{T}_{ikj}(\mathbf{s}, \mathbf{r}) \tag{3.19}$$

$$\mathbb{T}_{ijk}(\mathbf{r}, \mathbf{s}) = \mathbb{T}_{jki}(-\mathbf{t}, -\mathbf{r}) \tag{3.20}$$

$$\mathbb{T}_{ijk}(\mathbf{r}, \mathbf{s}) = \mathbb{T}_{kij}(-\mathbf{s}, \mathbf{t}) \tag{3.21}$$

The tensor form given in (3.12) is clearly linear in ψ, indeed it can be expressed as:

$$\mathbb{T}_{ijk} = \mathcal{L}_{ijk}(\psi) \tag{3.22}$$

where $\mathcal{L}_{ijk}$ is the tensor-valued linear operator implied by (3.12). To complete the model of the three-point third-order correlation, we need only specify $\psi(r, s, t)$ satisfying (3.17).

3.3.4 Scalar function ψ in the inertial range

Our primary interest is a model for $\mathbb{T}$ that is valid in the inertial range, analogous to the inertial range expression for $\mathbb{S}$ (3.8). Kolmogorov's 4/5 law constrains $\mathbb{S}$ to vary linearly with separation. Since $\mathbb{T}$ must reduce to $\mathbb{S}$ when r, s or t are zero, this linearity must be reflected in $\mathbb{T}$ as well. More generally, the Kolmogorov similarity argument[21, 29] requires that in the inertial range

$$\mathbb{T}(\alpha\mathbf{r}, \alpha\mathbf{s}) = \alpha\mathbb{T}(\mathbf{r}, \mathbf{s}) \tag{3.23}$$

The simplest way to ensure this linearity is to choose $\psi(r,s,t)$ to be a polynomial in r, s and t. Since each term in (3.12) is a seventh derivative of ψ, only terms with total degree of 8, will contribute to the linear scaling of $\mathbb{T}$. This, along with the symmetry constraint on ψ (3.17) suggests that ψ be constructed from terms of the form

$$p_{a,b} \equiv (r^a s^b - r^b s^a)t^c \tag{3.24}$$

with $a+b+c=8$ and a, b, $c \geq 0$. There are only 20 expressions of this form, and of these 14 produce non-zero $\mathbb{T}$ when substituting for ψ in (3.12).

However, all of these 14 non-trivial $\mathbb{T}$ are singular when r, s or t are zero. For example, terms such as: $r_i r_j r_k r/s^3$ arise, which is clearly singular at $s=0$. In addition, terms like $\delta_{ij} s_k r/s$ arise, which is discontinuous at $s=0$. It was found, however, that there is a 5-dimensional null space of the singular and discontinuous terms. There is thus a 5-dimensional space of possible ψ functions that yield non-singular, continuous $\mathbb{T}$. The space is spanned by the following 5 functions:

$$\psi^1 = \frac{1}{5760}[-27p_{0,3} - 3p_{0,5} + 4p_{2,3} + 18p_{3,5}] \tag{3.25}$$

$$\psi^2 = \frac{1}{1155840}[-315p_{0,3} + 4p_{0,7} + 56p_{2,5} - 140p_{3,4} + 1260p_{3,5}] \tag{3.26}$$

$$\psi^3 = \frac{1}{1257600}[-4p_{0,1} - 1935p_{0,3} - 40p_{1,2} + 80p_{1,3} - 60p_{1,4} + 16p_{1,5} + 180p_{2,3} + 990p_{3,5}] \tag{3.27}$$

$$\psi^4 = \frac{1}{462720}[-4p_{0,1} - 1215p_{0,3} - 36p_{1,2} + 64p_{1,3} - 36p_{1,4} + 4p_{1,6} + 108p_{2,3} - 20p_{2,5} + 40p_{3,4} + 270p_{3,5}] \tag{3.28}$$

$$\psi^5 = \frac{1}{10684800}[-60p_{0,1} - 16065p_{0,3} - 504p_{1,2} + 840p_{1,3} - 420p_{1,4} + 24p_{1,7} + 1260p_{2,3} + 7560p_{3,5}] \tag{3.29}$$

Where $p_{i,j}$ are as defined in (3.24) above. These functions have been normalized so that each of the $\mathbb{T}^n = \mathcal{L}(\psi^n)$ satisfies

$$\mathbb{T}^n_{ijk}(0, \mathbf{r}) = \frac{1}{15}\left(\delta_{ij} r_k - \frac{3}{2}(\delta_{ik} r_j + \delta_{jk} r_i)\right) \tag{3.30}$$

which is just (3.8) with ϵ set to 1. The analytic model we seek for $\mathbb{T}$ is thus given by:

$$\mathbb{T}_{ijk}(\mathbf{r}, \mathbf{s}) = \sum_{n=1}^{5} a_n \mathbb{T}^n_{ijk}(\mathbf{r}, \mathbf{s}) \qquad \text{with} \qquad \sum_{n=1}^{5} a_n = \epsilon \tag{3.31}$$

While the scalar basis functions ψ^n are relatively simple to write down (3.25–3.29), the basis tensors $\mathbb{T}^n$ are not. Indeed the expressions are so complex (as many as 758 terms), that they will not be written out here. The process by which the calculations were performed is described in Appendix C and programs are available at http://turbulence.ices.utexas.edu to evaluate the tensor numerically.

To display the features of the five basis tensors defined above, we examine the various components of the tensor for two special arrangements of the separation vectors. First is with the separation vectors $\mathbf{r}$ and $\mathbf{s}$ colinear (parallel, designated by $\|$), which, without loss of generality, we choose to be in the x_1 direction ($\mathbf{r} = r\mathbf{e}_1$, $\mathbf{s} = s\mathbf{e}_1$). In this case, there are only seven non-zero components, of which only $\mathbb{T}^{\|}_{111}$ and $\mathbb{T}^{\|}_{122}$ are independent. The other 5 ($\mathbb{T}^{\|}_{212}$, $\mathbb{T}^{\|}_{221}$, $\mathbb{T}^{\|}_{133}$, $\mathbb{T}^{\|}_{313}$ and $\mathbb{T}^{\|}_{331}$) are related to $\mathbb{T}^{\|}_{122}$ through symmetry.

The second separation vector configuration is with $\mathbf{r}$ and $\mathbf{s}$ orthogonal (designated by $\perp$). Again, without loss of generality $\mathbf{r} = r\mathbf{e}_1$ is chosen to be in the x_1-direction, and $\mathbf{s} = s\mathbf{e}_2$ is chosen in the x_2-direction. In this configuration, there are 14 nonzero components, of which seven are independent: $\mathbb{T}^{\perp}_{111}$, $\mathbb{T}^{\perp}_{112}$, $\mathbb{T}^{\perp}_{121}$, $\mathbb{T}^{\perp}_{122}$, $\mathbb{T}^{\perp}_{133}$, $\mathbb{T}^{\perp}_{313}$, $\mathbb{T}^{\perp}_{323}$. Each of these is one of a pair of symmetrically related components.

Since the tensor functions vary linearly with separation, the tensors can be normalized by $q \equiv \max(r, s, t)$, which for the special separation configurations considered leaves only the dependence on s/r. The non-zero, non-redundant components of $\mathbb{T}^{\parallel}/q$ and $\mathbb{T}^{\perp}/q$ are shown in figure 3.1 as a function of $\theta = \arctan(s/r)$. Note that the five basis tensors have similar structure, and that two of them are quite similar ($\mathbb{T}^3{=}\times$ and $\mathbb{T}^5{=}\square$). There has been no effort to orthogonalize the basis.

3.3.5 Fitting to DNS data

To determine the 5 coefficients $\{a_1, a_2, ..., a_5\}$ in (3.31), a least-squares fit to data from a Direct Numerical Simulation (DNS) of forced isotropic turbulence at $Re_\lambda = 164$ [34] is performed. Let $\mathbb{E}(\mathbf{r}, \mathbf{s}) = \mathbb{T}^{\mathrm{DNS}} - \mathbb{T}^{\mathrm{model}}$, be the error tensor. Then the fitting was done to minimize the objective function:

$$F = \left(1 - \frac{2}{\pi}\right) \int \mathbb{E}^{\parallel}_{ijk}(r,s)\mathbb{E}^{\parallel}_{ijk}(r,s)\,dr\,ds + \frac{2}{\pi}\int \mathbb{E}^{\perp}_{ijk}(r,s)\mathbb{E}^{\perp}_{ijk}(r,s)\,dr\,ds \tag{3.32}$$

under the constraint that $\sum_n a_n = \epsilon$, where only separation vectors $\mathbf{r}$ and $\mathbf{s}$ that are parallel or perpendicular are considered, to reduce the data requirements to a manageable level, and the integrals are taken over the domain in r and s for which q is in the approximate inertial range for the DNS ($q/\lambda \in [0.72, 1.2]$) or ($q/\eta \in [19, 32]$). This objective was selected as a (crude) approximation to the integral over all $\mathbf{r}$ and $\mathbf{s}$ in the inertial range. The coefficients obtained from this fit are given in table 3.1.

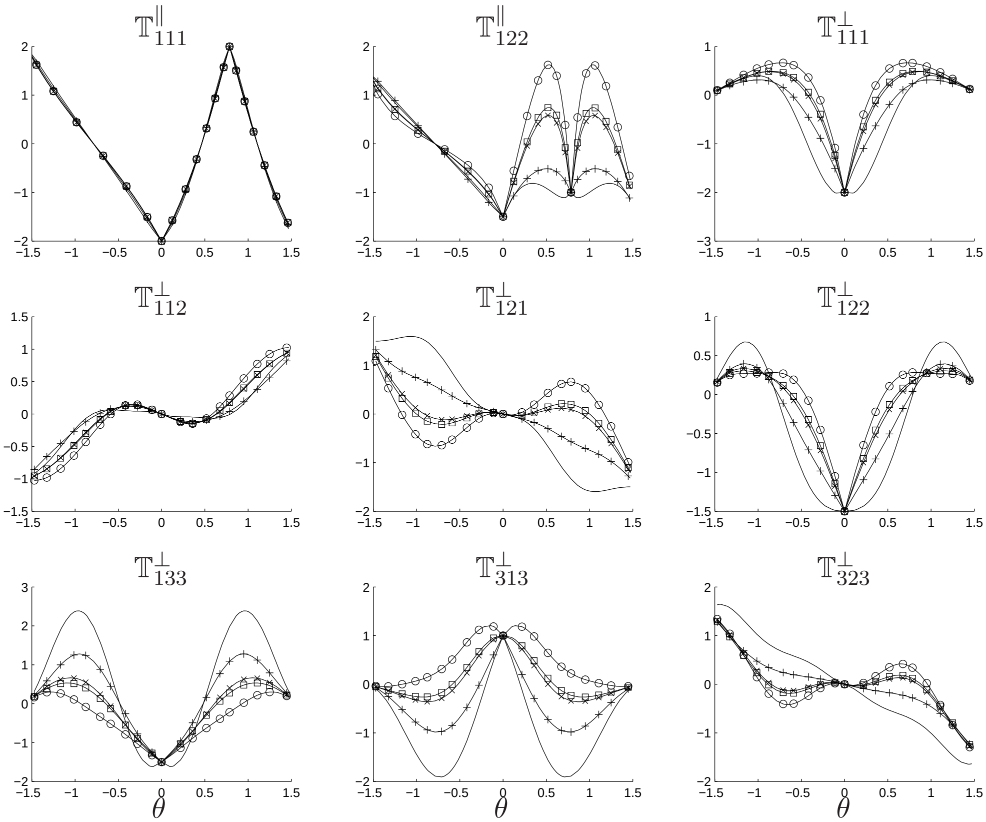

Figure 3.1: Basis functions for the non-zero, non-redundant components of $\mathbb{T}^{\parallel}/q$ and $\mathbb{T}^{\perp}/q$ (see text for definitions) as functions of $\theta = \arctan(s/r)$. $\mathbb{T}^1$=(plain curve), $\mathbb{T}^2$=+, $\mathbb{T}^3$=×, $\mathbb{T}^4$=◯, $\mathbb{T}^5$=□

a_1/ϵ	0.884
a_2/ϵ	-2.692
a_3/ϵ	-6.099
a_4/ϵ	-5.853
a_5/ϵ	14.760

Table 3.1: Values of the model coefficients in (3.31) found by fitting the DNS data of Langford & Moser[34]

The coefficient of determination is $R^2 = 0.96$, indicating that our model describes the DNS data quite well.

The ability of the model to represent the DNS correlations is shown in figure 3.2, in which non-zero components of $\mathbb{T}/q$ are plotted as a function of θ, for the parallel and perpendicular separation vectors, as in figure 3.1. The agreement between model and DNS is very good. One exception is the discrepancy in $\mathbb{T}^{\perp}_{111}$. This may be a problem with the DNS data rather than the model, because the DNS data was significantly unsymmetric which implies a lack of statistical convergence in the DNS data for this component. Further indication of the quality of the model is given in figure 3.3, where contour plots show the non-zero components of $\mathbb{T}$ as functions of r and s in both the model and the DNS. Since there is a symmetry in each term shown, the DNS and model are shown together in each frame, with a line of symmetry dividing them. The model and DNS are very similar. But, there is a minor discrepancy for r and s near zero, which is due to viscous effects not represented in the model.

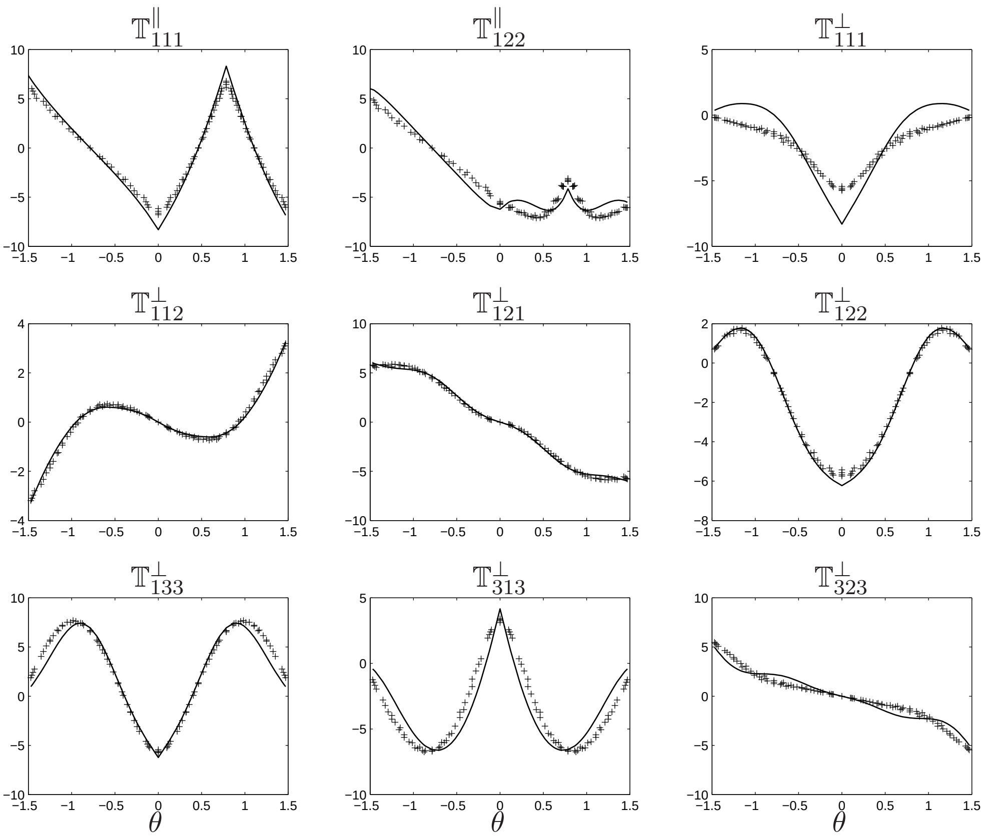

Figure 3.2: Basis functions for the non-zero, non-redundant components of $\mathbb{T}^{\parallel}/q$ and $\mathbb{T}^{\perp}/q$ (see text for definitions) as functions of $\theta = \arctan(s/r)$ from the DNS data of [34] (crosses) and the tensor model given by (3.31) and table 3.1 (curve).

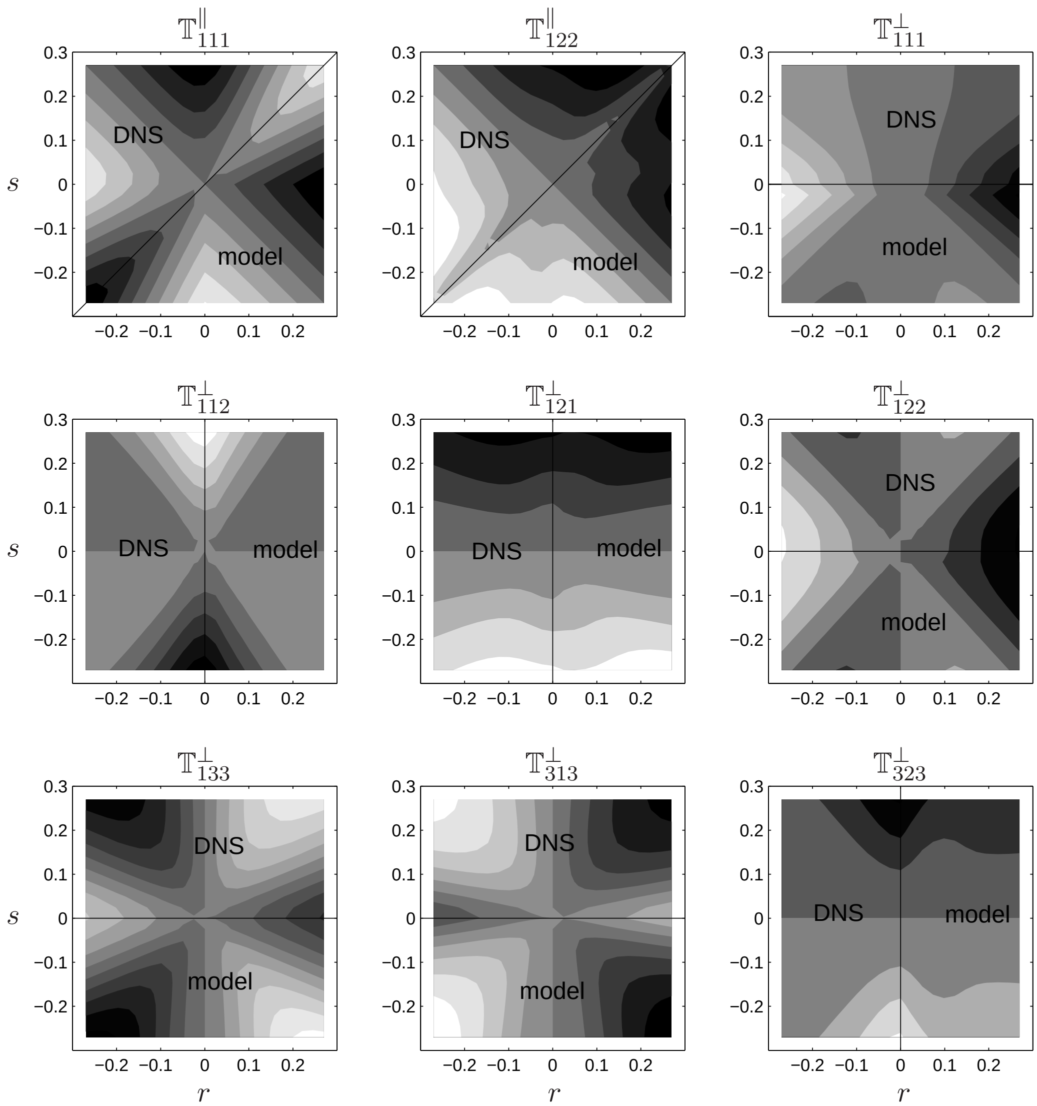

Figure 3.3: Contours of the DNS data of [34] and tensor model given by (3.31) and table 3.1 for $\mathbb{T}^{\parallel}$ and $\mathbb{T}^{\perp}$ (see text for definitions) in the r–s plane. Each component has a symmetry, which is used to allow the data and the model to be displayed side-by-side, as shown. The heavy black lines are lines of symmetry for each component.

3.4 Discussion and Implications

It is remarkable that the simple considerations of isotropy and the Kolmogorov similarity assumptions are sufficient to exactly determine the two-point third-order correlation $\mathbb{S}$, a third-ranked tensor. The three-point third-order correlation $\mathbb{T}$ is a much more complicated object, so it is equally remarkable that the same considerations, along with a plausible modeling ansatz regarding functional forms (3.24), is sufficient to specify a model for $\mathbb{T}$ in the inertial range with just four free constants. The model appears to fit low Reynolds number DNS data quite well. It would also be useful to test the model against higher Reynolds number DNS data.

While the considerations leading to the model are simple, the model itself is algebraically very complex. A special-purpose tensor algebra program was written to perform the necessary manipulations. The detailed results as well as programs used to evaluate the tensors numerically are available at http://turbulence.ices.utexas.edu. Given the complexity of the expressions, it may be that the ability to evaluate tensor components numerically will be most useful.

3.5 Performance of Theory-Based OLES Models

Multipoint correlation models described above were used to define a finite volume optimal LES model and perform LES at several grid resolutions [47]. The cases are infinite Reynolds number forced isotropic turbulence in a cubical periodic domain. Grid sizes ranging from 16^3 to 128^3, correspond to non-dimensional filter width $\gamma \approx 0.17$ to $\gamma \approx 0.02$ respectively, where $\gamma \equiv \Delta\epsilon/u^3$, Δ is the filter width or

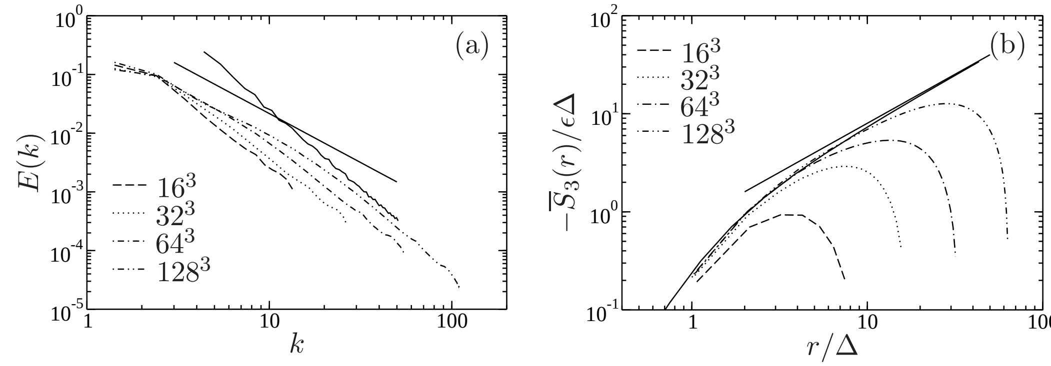

Figure 3.4: Three-dimensional energy spectra (a) and third-order structure functions (b) from OLES of isotropic turbulence at infinite Reynolds number using the finite-γ kernels, with resolutions ranging from 16^3 to 128^3 ($\gamma \approx 0.17$ to $\gamma \approx 0.02$ respectively). The solid lines in both plots are determined from Kolmogorov theory. In (a), the two solid lines are a $k^{-5/3}$ slope (shallow), and the result of filtering a $k^{-5/3}$ spectrum. In (b) the straight line is $S_3 = -\frac{4}{5}\epsilon r$, and the other solid line is the structure function of the filtered velocity.

cell size, ϵ is the dissipation rate and u^2 is the velocity variance. Excellent results are shown in figure 3.4. Shown are (a) three-dimensional energy spectra and (b) third-order structure functions. Figure 3.4(a) shows the high wavenumber portion of the LES energy spectra matching the filtered theoretical slope. Figure 3.4(b) shows the LES third-order structure functions matching the filtered theoretical curve in the inertial range for resolution greater than 32^3. These results indicate that optimal LES and the associated correlation models are a good basis for LES modeling for high Reynolds number turbulent flows that exhibit small-scale isotropy.

3.6 Relation to General LES

Multi-point velocity correlations like those described in this chapter, are central to the statistical description of homogeneous isotropic turbulence[21, 52].

The two-point second-order velocity correlation $\mathbb{R}_{ij}(\mathbf{r})$, and its Fourier transform, the spectrum tensor, are among the most commonly considered correlations, and a variety of models for their evolution have been developed[14, 31, 32, 38]. There have also been a number of theoretical and experimental efforts to analyze two-point correlations and structure functions [49, 56], including in the context of large eddy simulation modeling [60].

In homogeneous turbulence, the evolution equation for $\mathbb{R}$ contains the two-point third-order correlation $\mathbb{S}_{ijk}(\mathbf{r})$ as a result of the non-linear terms in the Navier-Stokes equations. $\mathbb{S}$ describes the transfer of energy from large-scales to small, and as such is of critical importance to the theory of the two-point statistics of turbulence. Assuming isotropy, the evolution equation for $\mathbb{R}$ reduces to the Karman-Howarth equation [67], written here in terms of $\mathbb{R}$ and $\mathbb{S}$

$$\frac{\partial \mathbb{R}_{ik}}{\partial t} = 2\nu \frac{\partial^2 \mathbb{R}_{ik}}{\partial r_j \partial r_j} + \frac{\partial \mathbb{S}_{ijk}}{\partial r_j} + \frac{\partial \mathbb{S}_{kji}}{\partial r_j} \tag{3.33}$$

Correspondingly, in homogeneous, isotropic, incompressible turbulence, the two-point correlation of the filtered velocity $\tilde{\mathbb{R}}_{ij}(\mathbf{r}) = \langle \tilde{v}_i(\mathbf{x})\tilde{v}_j(\mathbf{x}+\mathbf{r})\rangle$ evolves according to

$$\frac{\partial \tilde{\mathbb{R}}_{ik}}{\partial t} = 2\nu \frac{\partial^2 \tilde{\mathbb{R}}_{ik}}{\partial r_j \partial r_j} + \frac{\partial \tilde{\mathbb{S}}_{ijk}}{\partial r_j} + \frac{\partial \tilde{\mathbb{S}}_{kji}}{\partial r_j} + \frac{\partial \mathbb{Q}_{ijk}}{\partial r_j} + \frac{\partial \mathbb{Q}_{kji}}{\partial r_j} \tag{3.34}$$

where

$$\tilde{\mathbb{S}}_{ijk}(\mathbf{r}) = \langle \tilde{v}_i(\mathbf{x})\tilde{v}_j(\mathbf{x})\tilde{v}_k(\mathbf{x}+\mathbf{r})\rangle, \tag{3.35}$$

$$\mathbb{Q}_{ijk}(\mathbf{r}) = \langle \tau_{ij}(\mathbf{x}) \tilde{v}_k(\mathbf{x}+\mathbf{r}) \rangle. \tag{3.36}$$

The energy transfer between scales of the filtered velocity is mediated by $\tilde{\mathbb{S}}$. We can contract (3.34) to obtain the evolution equation for $\frac{1}{2}\tilde{\mathbb{R}}_{ii}$, which only depends on the magnitude of $\mathbf{r}$, and can be interpreted as the energy in the filtered field associated with scales larger than r. Then $-\partial\tilde{\mathbb{S}}_{iji}/\partial r_j(r)$ appears as the net flux of energy from scales larger than r in the filtered field to those smaller than r. This is analogous to the physical-space energy flux $-\partial S_{iji}/\partial r_j$ in the unfiltered equation [21], which is just ϵ in the inertial range. Similarly $-\partial\mathbb{Q}_{iji}/\partial r_j$ is interpreted as the net flux of energy from scales of the filtered fields larger than r to the sub-filter fluctuations $(\mathbf{v}-\tilde{\mathbf{v}})$. These average fluxes are generally positive (from large to small scales); but, this is an average of fluxes in both directions.

Because $\tilde{\mathbb{S}}$ includes the product of filtered velocities, it cannot be determined by directly filtering $\mathbb{S}$. It can, however be found by filtering $\mathbb{T}$:

$$\tilde{\mathbb{S}}_{ijk}(\mathbf{r}) = \int\int\int G(\mathbf{s})G(\mathbf{s}-\mathbf{r}')G(\mathbf{s}+\mathbf{r}-\mathbf{s}')\mathbb{T}_{ijk}(\mathbf{r}',\mathbf{s}')\, d\mathbf{s}\, d\mathbf{r}'\, d\mathbf{s}' \tag{3.37}$$

which can be derived easily by applying the filter (1.3) separately to each of the velocities in the definition of $\mathbb{T}$.

The two-point correlation equation (3.34) also includes $\mathbb{Q}$ arising from the sub-filter stress term in the LES equations. The definition of τ_{ij} (1.5) means that $\mathbb{Q}$ can be expressed

$$\mathbb{Q}_{ijk}(\mathbf{r}) = \hat{\mathbb{S}}_{ijk}(\mathbf{r}) - \tilde{\mathbb{S}}_{ijk}(\mathbf{r}) \tag{3.38}$$

where $\hat{\mathbb{S}}_{ijk}(\mathbf{r}) = \langle \widetilde{v_i v_j}(\mathbf{x})\tilde{v}_k(\mathbf{x}+\mathbf{r})\rangle$ can be determined by filtering the two-point third-order correlation of the unfiltered velocity

$$\hat{\mathbb{S}}_{ijk}(\mathbf{r}) = \int\int G(\mathbf{s})G(\mathbf{s}+\mathbf{r}-\mathbf{r}')\mathbb{S}_{ijk}(\mathbf{r}')\,d\mathbf{s}\,d\mathbf{r}'. \tag{3.39}$$

$\mathbb{T}$ was used to evaluate the third-order longitudinal structure function of the filtered velocity by using (3.37) to evaluate $\tilde{S}_3(r) = 6\tilde{\mathbb{S}}_{111}(r\mathbf{e}_1)$ for a Gaussian filter kernel given by

$$G(\mathbf{x}) = \frac{1}{\Delta\sqrt{2\pi}}e^{-|\mathbf{x}|^2/2\Delta^2}, \tag{3.40}$$

where Δ is the filter width. The result is plotted in figure 3.5 along with S_3 given by the 4/5 law. This filter is isotropic so it preserves the isotropy of the filtered field, implying that $\tilde{\mathbb{S}}_{ijk}$ is written in terms of $\tilde{S}_3$ in the same way that $\mathbb{S}_{ijk}$ is determined from S_3 (see Appendix A). Furthermore, the filter is homogeneous, and $\partial\mathbb{S}_{ijk}/\partial r_j$ is a constant in the inertial range, so (3.39) gives

$$\frac{\partial\hat{\mathbb{S}}_{ijk}}{\partial r_j} = \frac{\partial\mathbb{S}_{iji}}{\partial r_j} = -\frac{\epsilon}{3}\delta_{ik} \tag{3.41}$$

Therefore, $\mathbb{Q}$ (3.38) is directly determined from the difference between S_3 and $\tilde{S}_3$ shown in figure 3.5. In particular, using (A.3) we can write the energy fluxes $\partial\tilde{\mathbb{S}}_{iji}/\partial r_j = F(\tilde{S}_3)$ and $\partial\tilde{\mathbb{Q}}_{iji}/\partial r_j = F(S_3 - \tilde{S}_3)$, where the operator F is given by

$$F(S(r)) = \frac{2}{3r}S + \frac{7}{12}\frac{dS}{dr} + \frac{r}{12}\frac{d^2S}{dr^2}. \tag{3.42}$$

These two energy fluxes are also shown in figure 3.6. It is interesting that the flux to the sub-filter scales goes to zero so slowly with increasing r, only reaching 10% of the dissipation by $r = 15\Delta$. Further, because $S_3 - \tilde{S}_3$ goes to a constant for large r, the sub-filter flux only goes to zero like $1/r$.

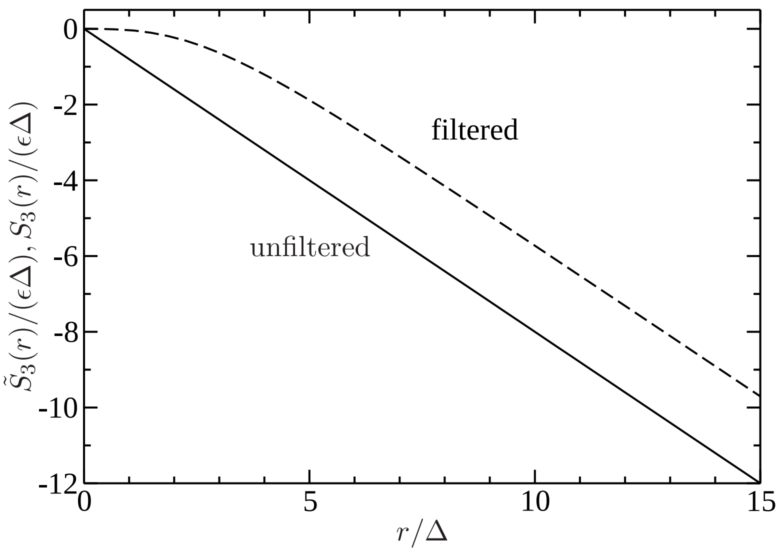

Figure 3.5: Third-order longitudinal structure function $\tilde{S}_3$ of a Gaussian filtered infinite Reynolds number isotropic turbulence computed from the tensor model described by equation (3.31) and table 3.1. Also shown is the unfiltered structure function S_3 from the Kolmogorov 4/5 law.

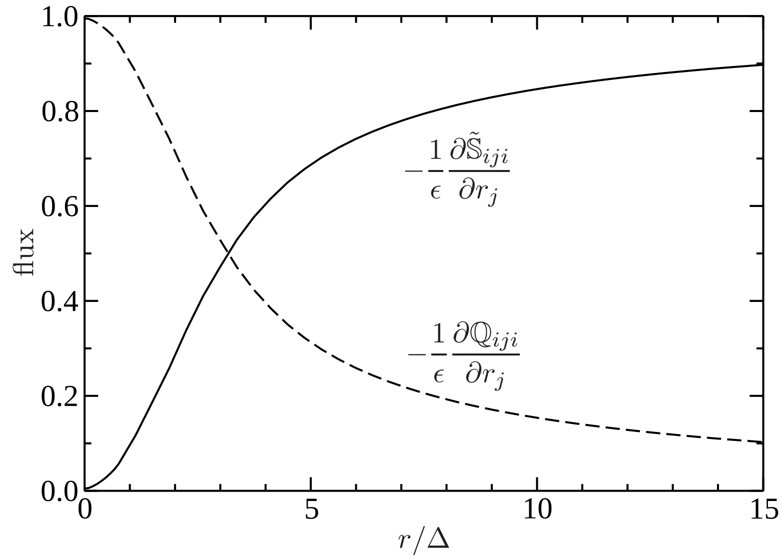

Figure 3.6: The energy flux terms in (3.34) calculated from the third-order longitudinal structure functions in figure 3.5. Both the flux to resolved scales $-\frac{\partial \tilde{\mathbb{S}}_{iji}}{\partial r_j}$ and the flux to sub-filter scales $\frac{\partial \mathbb{Q}_{iji}}{\partial r_j}$ are shown, normalized by ϵ.

Chapter 4

Wall-Bounded OLES

The optimal models and associated statistical models discussed in chapter 3 are not valid near the wall of a wall-bounded turbulent shear flow, due to the strong inhomogeneity and anisotropy there. In this case, we explore the application of finite-volume optimal LES. To avoid uncertainties associated with postulating theoretical models for multi-point correlations near the wall, the optimal LES study described here will employ correlation data derived from direct numerical simulation of a turbulent channel at $Re_\tau = 934$.

4.1 High Reynolds Number Wall-Bounded Turbulence and LES

Many flows in nature and engineering are wall-bounded. Examples are water flow through a pipe and air flow around a wing. In wall-bounded flows, the presence of the wall results in the removal of momentum and energy from the flow due to viscosity. The shear flow thickness δ (e.g. boundary layer thickness, pipe diameter, or channel height) is one important length scale. The wall also introduces a second much smaller length scale, the viscous or wall scale

$$\delta_\nu = \frac{\nu}{u_\tau} \tag{4.1}$$

where the friction velocity is

$$u_\tau = \sqrt{\frac{\tau_w}{\rho}} \tag{4.2}$$

τ_w is the mean wall shear stress ([52], pp 268-271). In a region near the wall with thickness of order δ_ν, viscosity dominates. Near the wall, turbulent eddy sizes scale with δ_ν, while far from the wall turbulence scales with the layer thickness δ. Also, a layer of order δ_ν thick near the wall is where a large fraction of the production and dissipation of turbulence occurs.

This two-scale structure of wall bounded turbulent shear flows leads to the famous log-law for the mean velocity ([52], pp 271-281). It also introduces difficult problems for LES [50]. In the near-wall layer, the dominant large-scale turbulence is of scale δ_ν which, as Reynolds number increases, becomes ever smaller compared to the turbulence scale away from the wall δ. The usual idea in LES is that the formulation will resolve the dynamics of the dominant large scales. But near the wall, this would require resolution of order the wall scale. Many LES of wall-bounded flows have been performed using this resolved wall approach, but the cost of such an LES scales with Reynolds number almost as strongly as a DNS [50].

The alternative is to not resolve the wall layer, instead only resolving scales of order δ. The cost will then scale independently or very weakly with Reynolds number. However, this requires that the LES model represent the effects of nearly all the turbulence in the near-wall layer. Figure (4.1) shows RMS velocity fluctuations as a function of distance from the wall y, with a superimposed uniform grid designed to resolve scales of order δ. Notice that the peak streamwise fluctuations u and wall-normal fluctuations v occur within the first grid cell. Figure (4.5) shows the terms

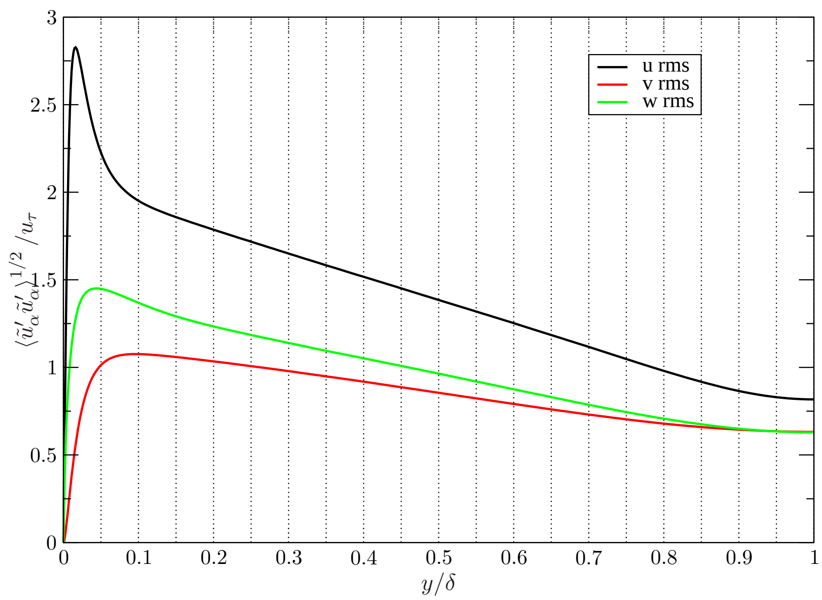

Figure 4.1: RMS velocity fluctuations from DNS of channel flow at $Re_\tau = 934$, with superimposed uniform LES grid of $\Delta_y/\delta = 1/20$. The fluctuations are not resolved in the cell adjacent to the wall. The turbulence is inhomogeneous and anisotropic.

in the streamwise energy equation (4.12) as a function of distance from the wall y, with the same superimposed grid. Notice that the peak action in each of the curves occurs within the first grid cell. The LES cell adjacent to the wall covers this region of highest turbulent dynamics. Therefore, this LES grid cannot resolve any of the turbulent physics in this region. All of these processes must then be modeled. Standard LES modeling approaches are not valid in these circumstances, but the optimal LES formulation is valid, provided correlation data is available. It is LES with these unresolved wall layers that are investigated here in the context of a finite-volume formulation of LES.

In what follows, it will be convenient to adopt the following notation for wall-bounded turbulence: the streamwise, wall-normal, and spanwise directions will be denoted x, y, and z respectively, and u, v, w will denote velocity in those directions.

4.2 Existing Wall Models and Volumetric Models

LES modeling with unresolved wall layers actually involves two modeling challenges. First, the velocity gradient at the wall is not resolved. See figure (4.2). Therefore the standard no-slip condition is not an appropriate boundary condition. Instead, the wall shear stress must be modeled. Some of the earliest work in wall modeling was done by Deardorff [17] and Schumann [59]. Schumann's wall model was later modified by Piomelli [51] to get it's current popular form

$$\tau_{xy,w}(x,z) = \frac{[\tau_w]}{[\tilde{u}(x,Y,z)]}\tilde{u}(x+\Delta_s,Y,z) \tag{4.3}$$

$$\tau_{zy,w}(x,z) = \frac{[\tau_w]}{[\tilde{u}(x,Y,z)]}\tilde{w}(x+\Delta_s,Y,z) \tag{4.4}$$

$$\tilde{v}_w(x,z) = 0 \tag{4.5}$$

where the plane averaged wall shear stress $[\tau_w]$ is estimated using the well-known log law

$$\frac{[\tilde{u}(x,Y,z)]}{u_\tau} = \frac{1}{\kappa}\ln\frac{u_\tau Y}{\nu} + B. \tag{4.6}$$

Here the $[\cdot]$ operation is an average over the plane parallel to the wall at Y, the cell adjacent to the wall. Assuming that Y is in the log law region, this model infers $[\tau_w]$, which is then used to estimate the instantaneous, local τ_w from equations (4.3) and (4.4), which state that wall stress fluctuates in proportion to the velocity in the adjacent cell, shifted downstream by some Δ_s.

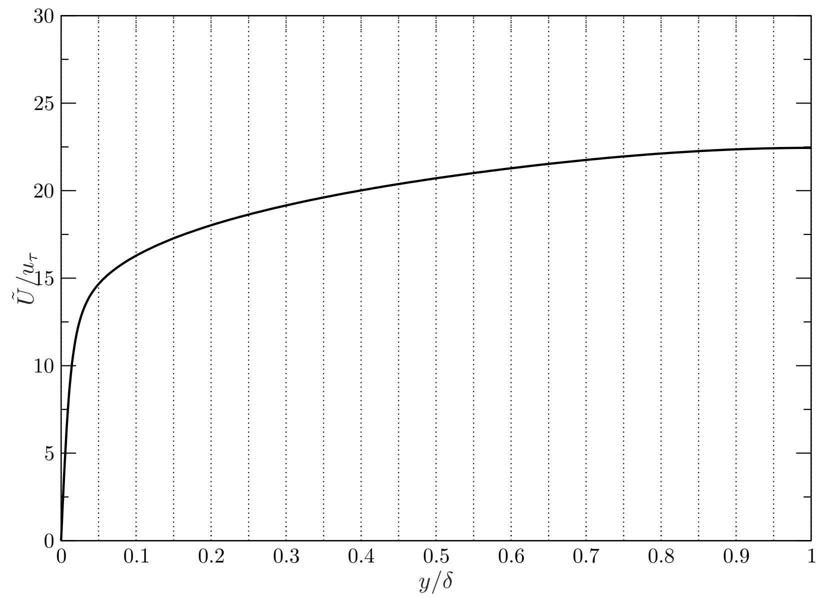

Figure 4.2: Mean velocity profile from DNS of channel flow at $Re_\tau = 934$, with superimposed LES grid, with superimposed uniform LES grid of $\Delta_y/\delta = 1/20$. The mean velocity gradient is not resolved in the cell adjacent to the wall.

Other wall models include the Two-Layer Model (TLM) by Balaras et al [6] and Detached Eddy Simulation (DES) by Spalart [62]. TLM adds an "inner" grid near the wall to resolve the wall stress, which is then fed back into the "outer" grid as a boundary condition. DES uses just one grid but two models, LES for the outer flow and RANS for the inner flow.

The cost of LES for a spatially developed flow with an unresolved wall layer using Piomelli's log law wall model is independent of Reynolds number. If the flow is spatially developing, then cost scales with $Re^{0.5}$ [50]. TLM costs marginally more. DES scales with $Re^{0.9}$ [50]. Compare then with $Re^{2.4}$ for a "resolved LES" where the important small scales near the wall are resolved, and Re^{3} for DNS where all scales are resolved. These cost scaling estimates provide strong motivation for pursuing LES models with unresolved wall layers. For a more detailed overview of wall models, see the review by Piomelli and Balaras [50]. After comparing various wall models for several wall-bounded flows, they conclude that simple wall models based on the log law work well for simple flows, such as channel flow. However, for more complex flows, such as flow over a backward facing step, more sophisticated models like TLM and DES work better. Since their review, a novel wall model has been implemented in a Fourier-spectral LES of channel flow by Bhattacharya et al [9]. Their wall model involves adding a buffer region outside the channel wall, where the kinetic energy is minimized to solve for the wall stress. When coupled with an optimal volumetric model, this gave good results.

The second challenge in near-wall modeling arises from the fact that volumetric LES models are generally not valid in the near-wall region because such models (e.g. the optimal models in chapter 3, or dynamic Smagorinsky [22, 61]) assume that the small scales are homogeneous and isotropic, and that the local turbulence Reynolds number is large. None of these is true near the wall. Notice how different the fluctuation magnitudes are in u', v', and w' and how they are strongly inhomogeneous in the y direction in figure (4.1). Nonetheless, models such as the dynamic Smagorinsky model have been widely used for near wall turbulence. Cabot and Moin [12] used a dynamic Smagorinsky subgrid model and several wall models (log law and TLM) with a second-order finite-difference code to solve for channel flow with an unresolved wall layer. Their results appear reasonable, in that velocity mean and variance profiles are comparable with DNS. However, with such coarse filtering (wall-normal grid spacing is $250\delta_\nu$), the LES variances should be much smaller, because near the wall much of the turbulent energy is not resolved. A more proper comparison is made between the LES and *filtered* DNS variances, shown in figure (4.3). This problem with high streamwise variances is prevalent in LES of wall-bounded flows with unresolved wall layers.

Optimal models, which do not depend on isotropy and homogeneity assumptions have performed well in channel flows; see Volker et al [66] and Bhattacharya et al [9], and serve as a basis for the developments pursued here. Several observations from previous OLES studies will be useful in the current development (see Section 2.3). In particular, Zandonade et al [68] demonstrated the viability of finite-volume OLES in forced isotropic turbulence, and that small local stencils are sufficient for modeling nonlinear flux. Volker et al [66] showed the importance of constructing models with appropriate dependencies, and particularly to represent

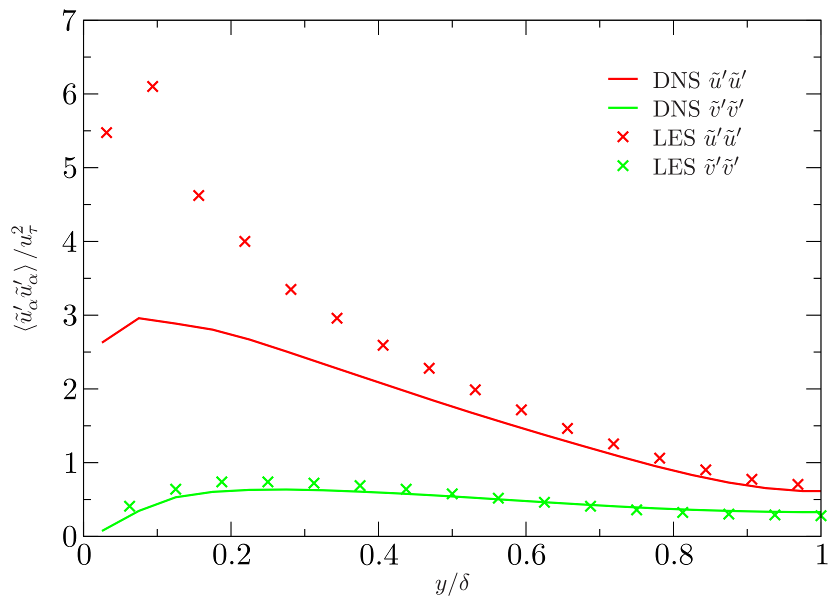

Figure 4.3: Normalized velocity variance profiles for LES of channel flow at $Re_\tau = 4000$ with dynamic Smagorinsky model and $\Delta_y/\delta = 1/16$ from paper by Cabot and Moin, [12], compared with filtered DNS at $Re_\tau = 934$ and $\Delta_y/\delta = 1/20$. Streamwise variances predicted by the LES are too high.

the subgrid contribution to critical terms in the Reynolds stress transport equation. Bhattacharya et al [9] showed that good results are acheiveable without resolving the near wall turbulence. All these results motivate and guide us in studying wall-bounded finite-volume OLES.

4.3 Finite-Volume LES for Channel Flow

We are investigating volumetric and wall modeling within the framework of finite-volume optimal LES of a full-developed turbulent channel flow. Finite-volume methods are desirable, because they are easier to extended to more complex geometries, easier than say a Fourier spectral method. We employ the optimal methodology because it generates the best coefficients for a given model form, and therefore is useful for evaluating different model forms and dependencies. Furthermore, optimal models are not limited by assumptions common to turbulence models such as homogeneity, isotropy, scale-similarity, and existence of an inertial range, all of which break down close to walls. An optimal model simply does what the turbulence statistics say it should do, with correlations to be determined in our case from DNS data. We choose to investigate turbulent channel flow, because it is one of the simplest wall-bounded flows, and because there are a lot of data for this flow geometry [26, 28, 46]. DNS results have proven to be accurate when compared with theory and experiment, and it is the best resolved and most readily available data we have access to. This data will be used for constructing and testing of our models.

The finite-volume LES will be formulated on a staggered grid; that is, grid cells for the i-component of velocity are staggered by $-\frac{\Delta_i}{2}$ in the i-direction. The

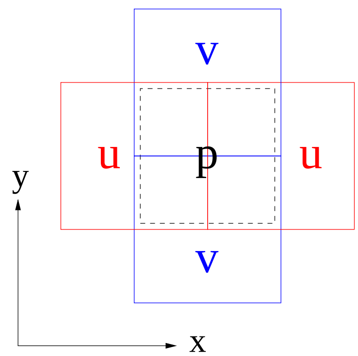

Figure 4.4: Staggered finite-volume grid, centered on pressure cell, with i-component velocity cell staggered by $-\frac{\Delta_i}{2}$ in the i-direction

pressure cell is not staggered. See figure (4.4). This is done because the modeling errors associated with representing continuity and pressure are much smaller than with a unstaggered formulation [36].

The channel flow domain $L_x/\delta = 8\pi$, $L_y/\delta = 2$, $L_z/\delta = 3\pi$ is discretized into a $384 \times 40 \times 144$ grid. This results in grid sizes $\Delta_x/\delta = 0.065$, $\Delta_y/\delta = 0.050$, $\Delta_z/\delta = 0.065$ or in wall units $\Delta_x/\delta_\nu = 61$, $\Delta_y\delta_\nu = 47$, $\Delta_z\delta_\nu = 61$. Boundary conditions are periodic in the x and z directions, and wall stresses are modeled at the y boundaries. A standard fourth-order Runge-Kutta method [24] is used in conjunction with a fractional step method [15] which imposes the divergence-free condition on the staggered finite-volume grid. Total simulation time is $\frac{Tu_\tau}{\delta} = 10$, in steps of $\frac{\Delta t u_\tau}{\delta} = 0.001$ which is less than $\frac{u_\tau \Delta_x}{u_{max}\delta} = 0.0026$ as required by the CFL condition. We are running $Re_\tau = 934$. Corresponding DNS data used for model statistics and testing come from Alamo et al [18].

4.3.1 Continuous and Filtered Equations

The Navier-Stokes momentum equations are

$$\partial_t u_i = -\partial_j u_i u_j - \partial_i p + \frac{1}{Re}\partial_j \partial_j u_i \tag{4.7}$$

For a Cartesian grid aligned with the coordinates directions x, y, and z, we can write the box-filtered Navier-Stokes equation

$$\partial_t \tilde{u}_i = -\tilde{\partial}_j \overline{u_i u_j} - \tilde{\partial}_i \overline{p} + \frac{1}{Re}\tilde{\partial}_j \overline{\partial_j u_i} \tag{4.8}$$

where

$$\tilde{u}_i = \frac{1}{V}\int_V u_i \,\mathrm{d}\mathbf{x} \tag{4.9}$$

$$\tilde{\partial}_j \overline{f} = \frac{1}{\Delta_j}(\overline{f}^{+j} - \overline{f}^{-j}) \tag{4.10}$$

$$\overline{f}^{\pm j} = \frac{1}{S}\int_{S^{\pm j}} f \,\mathrm{d}\mathbf{x} \tag{4.11}$$

For a given Cartesian volume V, S^{+j} is the face in the plus j direction, and S^{-j} is the face in the minus j direction.

Likewise the component energy equations without and with box-filtering are

$$\begin{aligned}\partial_t \left\langle u'_\alpha u'_\alpha \right\rangle = & \underbrace{-2\left\langle u'_\alpha \partial_\alpha p' \right\rangle}_{pressure\,redistribution} \underbrace{-2\left\langle u'_\alpha u'_j \right\rangle \partial_j U_\alpha}_{production} \underbrace{-U_j \partial_j \left\langle u'_\alpha u'_\alpha \right\rangle}_{convection} \\ & \underbrace{-\partial_j \left\langle u'_j u'_\alpha u'_\alpha \right\rangle}_{turbulent\,transport} \underbrace{-\frac{1}{Re}\left\langle \partial_j u'_\alpha \partial_j u'_\alpha \right\rangle}_{viscous\,dissipation} + \underbrace{\frac{1}{Re}\partial_j \partial_j \left\langle u'_\alpha u'_\alpha \right\rangle}_{viscous\,transport}\end{aligned} \tag{4.12}$$

$$\begin{aligned}\partial_t \frac{1}{2}\left\langle \tilde{u}'_\alpha \tilde{u}'_\alpha \right\rangle = & \underbrace{-\left\langle \tilde{u}'_\alpha \tilde{\partial}_\alpha \overline{p'} \right\rangle}_{pressure\,redistribution} \underbrace{-\left\langle \tilde{u}'_\alpha \tilde{\partial}_j \overline{U_\alpha u'_j} \right\rangle}_{production} \underbrace{-\left\langle \tilde{u}'_\alpha \tilde{\partial}_j \overline{u'_\alpha U_j} \right\rangle}_{convection} \\ & \underbrace{-\left\langle \tilde{u}'_\alpha \tilde{\partial}_j \overline{u'_\alpha u'_j} \right\rangle}_{turbulent\,transport/dissipation} + \underbrace{\frac{1}{Re}\left\langle \tilde{u}'_\alpha \tilde{\partial}_j \overline{\partial_j u'_\alpha} \right\rangle}_{viscous\,dissipation/transport}\end{aligned} \tag{4.13}$$

The pressure term spatially transports energy and transfers energy between components. Production transfers energy from the mean into the fluctuations (of the same component). Convection spatially transports energy. In the filtered equations, the same term can also dissipate energy. Turbulent transport transports energy in physical and wavenumber space. In the filtered equations, the same term also dissipates energy (transfers to unresolved scales). The viscous term dissipates and spatially transports energy. Figure (4.5) shows these various terms in equation (4.12). Figure (4.6) shows the corresponding terms in equation (4.13). Notice that the curves are for the most part qualitatively similar, but different in the details. As stated above, the convective and turbulent dissipation terms in the filtered component energy equation exhibit dissipation. One may also notice that in the filtered component energy equations, the viscous and turbulent transport are relatively small compared to the other terms. Although these transport effects are significant in the continuous component energy equations, they are within the first finite-volume cell adjacent to the wall and therefore their effects are integrated out in the filtered component energy equations.

The component energy equations are closely related to the Reynolds stress transport equations, which are shown below in continuous and filtered form.

$$\partial_t \left\langle u_i' u_k' \right\rangle = \underbrace{-\left\langle u_k' \partial_i p' \right\rangle - \left\langle u_i' \partial_k p' \right\rangle}_{pressure\, redistribution} \underbrace{-\left\langle u_k' u_j' \right\rangle \partial_j U_i - \left\langle u_i' u_j' \right\rangle \partial_j U_k}_{production}$$
$$\underbrace{-U_j \partial_j \left\langle u_i' u_k' \right\rangle}_{convection} \underbrace{-\partial_j \left\langle u_j' u_i' u_k' \right\rangle}_{turbulent\, transport} \underbrace{-\frac{2}{Re} \left\langle \partial_j u_i' \partial_j u_k' \right\rangle}_{viscous\, dissipation} + \underbrace{\frac{1}{Re} \partial_j \partial_j \left\langle u_i' u_k' \right\rangle}_{viscous\, transport} \tag{4.14}$$

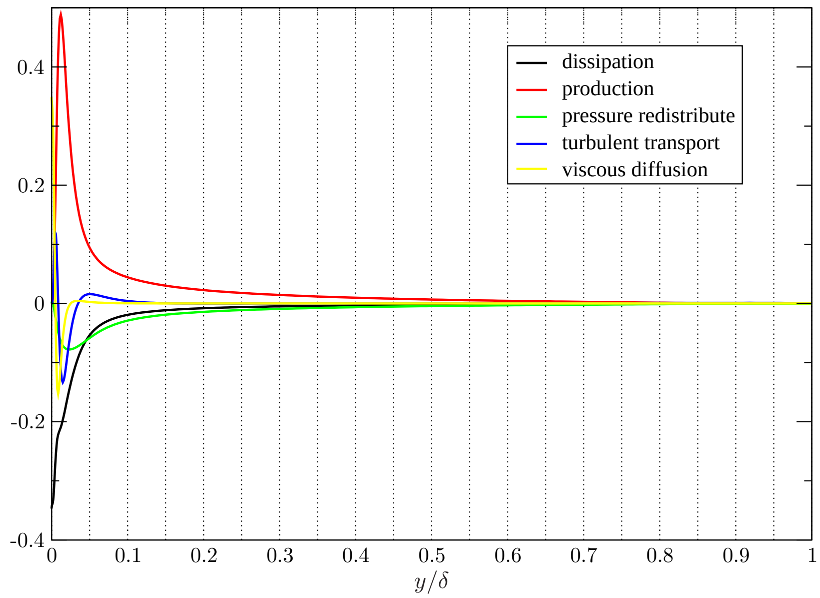

(a) channel half-width

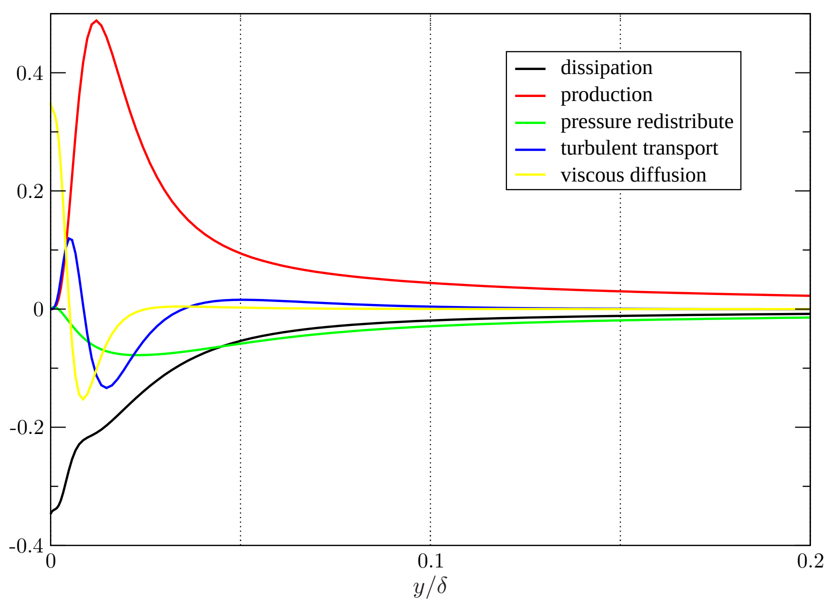

(b) near-wall region

Figure 4.5: Terms from the continous streamwise energy equation from DNS of channel flow at $Re_\tau = 934$, with superimposed uniform LES grid of $\Delta_y/\delta = 1/20$. None of these terms are resolved by the cell adjacent to the wall. Top plot shows the entire channel half-width. Bottom plot is zoomed into the near-wall region.

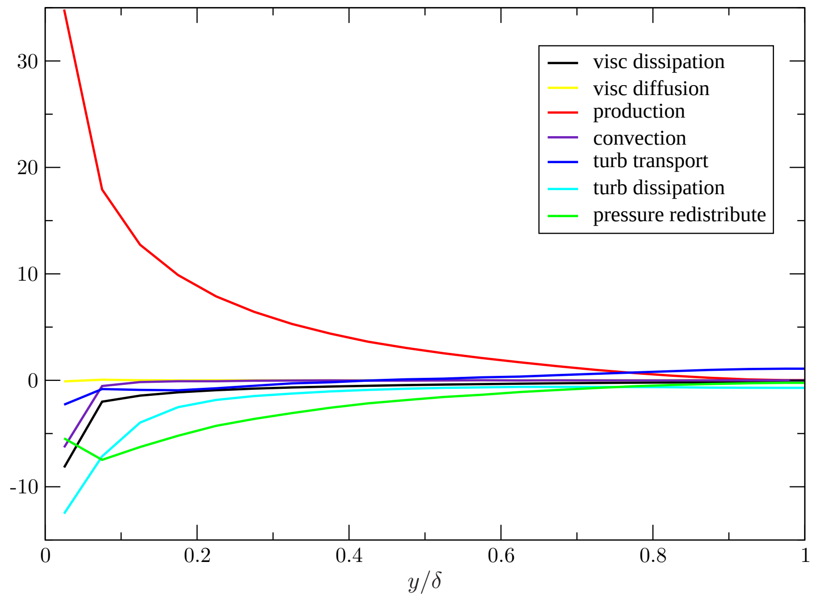

Figure 4.6: Terms from the filtered streamwise energy equation from DNS of channel flow at $Re_\tau = 934$.

$$\begin{aligned}
\partial_t \left\langle \underline{\tilde{u}'_i}_k \underline{\tilde{u}'_k}_i \right\rangle = & \underbrace{- \left\langle \underline{\tilde{u}'_k}_i \underline{\tilde{\partial}_i \overline{p'}}_k \right\rangle - \left\langle \underline{\tilde{u}'_i}_k \underline{\tilde{\partial}_k \overline{p'}}_i \right\rangle}_{pressure\,redistribution} \underbrace{- \left\langle \underline{\tilde{u}'_k}_i \underline{\tilde{\partial}_j \overline{U_i u'_j}}_k \right\rangle - \left\langle \underline{\tilde{u}'_i}_k \underline{\tilde{\partial}_j \overline{U_k u'_j}}_i \right\rangle}_{production} \\
& \underbrace{- \left\langle \underline{\tilde{u}'_k}_i \underline{\tilde{\partial}_j \overline{u'_i U_j}}_k \right\rangle - \left\langle \underline{\tilde{u}'_i}_k \underline{\tilde{\partial}_j \overline{u'_k U_j}}_i \right\rangle}_{convection} \underbrace{- \left\langle \underline{\tilde{u}'_k}_i \underline{\tilde{\partial}_j \overline{u'_i u'_j}}_k \right\rangle - \left\langle \underline{\tilde{u}'_i}_k \underline{\tilde{\partial}_j \overline{u'_k u'_j}}_i \right\rangle}_{turbulent\,transport/dissipation} \\
& + \underbrace{\frac{1}{Re} \left\langle \underline{\tilde{u}'_k}_i \underline{\tilde{\partial}_j \overline{\partial_j u'_i}}_k \right\rangle + \frac{1}{Re} \left\langle \underline{\tilde{u}'_i}_k \underline{\tilde{\partial}_j \overline{\partial_j u'_k}}_i \right\rangle}_{viscous\,dissipation/transport} \quad (4.15)
\end{aligned}$$

where the underline operator $\underline{(\cdot)}_k$ indicates an average in the k direction.

$$\underline{f}_k = \frac{1}{2}(f^{+k} - f^{-k}) \quad (4.16)$$

The variable being evolved is a filtered version of Reynolds stress

$$\underline{\tilde{u}'_i}_k \underline{\tilde{u}'_k}_i = \frac{1}{4}(\tilde{u}'^{-k}_i + \tilde{u}'^{+k}_i)(\tilde{u}'^{-i}_k + \tilde{u}'^{+i}_k) \quad (4.17)$$

This is the standard model for the nonlinear flux term $\overline{u'_i u'_k}$. $\tilde{u}_i'^{-k}$ and $\tilde{u}_i'^{+k}$ are the i component of the velocity located on the minus k and plus k sides, respectively, of the flux face. $\tilde{u}_k'^{-i}$ and $\tilde{u}_k'^{+i}$ are the k component of the velocity located on the minus i and plus i ends, respectively, of the flux face. For example, the cells involved in the filtered Reynolds stress $\underline{\tilde{u}'}_y \underline{\tilde{v}'}_x$ are shown in figure (4.10b).

4.3.2 Standard Finite-Volume Method

The terms in the filtered equation (4.8) are modeled

$$\partial_t w_i = -\tilde{\partial}_j \overline{u_i u_j}^{mod} - \tilde{\partial}_i \overline{p}^{mod} + \frac{1}{Re} \tilde{\partial}_j \overline{\partial_j u_i}^{mod} \tag{4.18}$$

where w_i is the LES velocity field. Ideally it's evolution would model that of the filtered DNS $\tilde{u}_i$ as closely as possible. The standard second-order staggered-grid finite-volume approximation ("standard approximation" or "standard model" for short) for the terms in the above equation were introduced by Harlow and Welch, [25], and are described below.

The standard approximation for the nonlinear term is

$$\overline{u_i u_j}_{std}^{mod} = \frac{1}{4}(w_i^{-j} + w_i^{+j})(w_j^{-i} + w_j^{+i}) \tag{4.19}$$

w_i^{-j} and w_i^{+j} are the i component of the velocity located on the minus j and plus j sides, respectively, of the flux face. w_j^{-i} and w_j^{+i} are the j component of the velocity located on the minus i and plus i ends, respectively, of the flux face.

The standard approximation for the viscous term is

$$\overline{\partial_j u_i}_{std}^{mod} = \frac{1}{\Delta_j}(w_i^{+j} - w_i^{-j}) \tag{4.20}$$

The LES field w is evolved using a fractional step method by Chorin [15]. The method incorporates a global solve for a discrete pressure-like field ϕ, which is the standard pressure approximation $\overline{p}^{mod}_{std} \equiv \phi$.

The fractional step method first evolves the velocity by evaluating the nonlinear and viscous models, and stepping forward in time, the result being the "auxiliary velocity" w_i^*.

$$w_i^* = w_i^n + \Delta t(-\tilde{\partial}_j \overline{u_i u_j} + \frac{1}{Re}\tilde{\partial}_j \overline{\partial_j u_i}) \tag{4.21}$$

This auxiliary velocity field is then used as the source for a Poisson-pressure equation

$$\Delta t \tilde{\partial}_i \tilde{\partial}_i \phi = \tilde{\partial}_i w_i^* \tag{4.22}$$

with boundary condition at the walls

$$\Delta t \tilde{\partial}_2 \phi = w_2^* \tag{4.23}$$

Here, $\tilde{\partial}_i \tilde{\partial}_i$ is a discrete Laplacian operator on ϕ, and $\tilde{\partial}_i w_i^*$ is a discrete divergence of the staggered velocity field w_i^*.

$$\tilde{\partial}_i w_i^* = \sum_{i=1}^{3} \frac{1}{\Delta_i}(w_i^{*+i} - w_i^{*-i}) \tag{4.24}$$

Figure (4.7) shows the configuration of the cells involved.

And finally, the evolution of the velocity field is completed by adding in the gradient of the standard pressure model.

$$w_i^{n+1} = w_i^* + \Delta t(-\tilde{\partial}_i \phi) \tag{4.25}$$

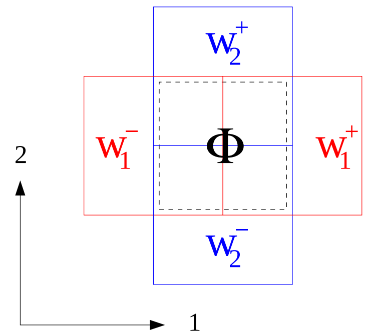

Figure 4.7: Configuration of staggered grid cells w and standard pressure model ϕ.

Chorin's method may also be expressed as a discrete divergence-free projection operator on w_i^*. Start by rewriting equation (4.22)

$$\phi = (\tilde{\partial}_j \tilde{\partial}_j)^{-1} \tilde{\partial}_k \frac{w_k^*}{\Delta t} \tag{4.26}$$

where $(\tilde{\partial}_j \tilde{\partial}_j)^{-1}$ is the inverse Laplacian. Then taking the gradient of both sides

$$\tilde{\partial}_i \phi = \underbrace{\tilde{\partial}_i (\tilde{\partial}_j \tilde{\partial}_j)^{-1} \tilde{\partial}_k}_{D_{ik}} \frac{w_k^*}{\Delta t} \tag{4.27}$$

where D_{ik} is a linear operator which returns the divergent part of it's argument. Plugging this into equation (4.25) gives

$$w_i^{n+1} = w_i^* + \Delta t(-\tilde{\partial}_i \phi) = w_i^* - D_{ik} w_k^* = \underbrace{(\delta_{ik} - D_{ik})}_{P_{ik}} w_k^* \tag{4.28}$$

where P_{ik} is the divergence-free projection operator.

In essence, the gradient of the standard pressure model removes the divergent part of the nonlinear and viscous fields. The filtered viscous field is almost divergence-free and therefore can be neglected in development of the pressure model. The standard pressure model can be applied to the actual filtered fields or to their

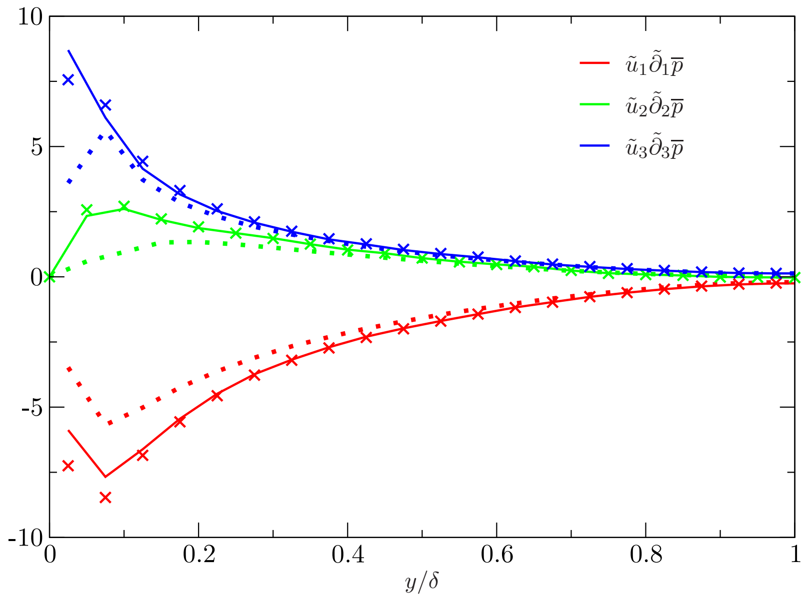

Figure 4.8: Actual filtered pressure $\overline{p}$ (solid curve), standard pressure model ϕ applied to actual nonlinear term ($\times$'s), and standard pressure model ϕ applied to standard nonlinear model (dotted curve) in filtered component energy equations for channel flow at $Re_\tau = 934$. The gradient of the standard pressure model is the divergent part of the nonlinear term it acts upon, $\tilde{\partial}_i\phi = -D_{ik}\tilde{\partial}_j\overline{u_k u_j}$.

models. The standard pressure model ϕ applied to the actual filtered nonlinear fields quite closely models the actual filtered pressure $\overline{p}$, as shown in figure (4.8). Also shown is the standard pressure model applied to the standard nonlinear *model*. Notice the errors in all three component energy equations. We infer from this that errors in "pressure modeling" result primarily from problems with the nonlinear model and not with the standard pressure model itself. This means the standard pressure model will be a good model for the actual filtered pressure as long as we have a "good enough" model for the nonlinear term.

To decrease the computation cost of the standard pressure solver, we actually Fourier transform equation (4.22) in the streamwise and spanwise, x and z, directions. (These directions are homogeneous with periodic boundaries.)

$$\Delta t\left(-(k_x^2+k_z^2)+\tilde{\partial}_y\tilde{\partial}_y\right)\hat{\phi}=\hat{H} \tag{4.29}$$

where $H=\tilde{\partial}_i w_i^*$, and $\tilde{\partial}_y\tilde{\partial}_y\hat{\phi}(y)=\frac{1}{\Delta_y^2}(\hat{\phi}(y+\Delta_y)-2\hat{\phi}(y)+\hat{\phi}(y-\Delta_y))$ is a standard second-order second-derivative approximation, and (k_x^2,k_z^2) are numerical eigenvalues corresponding to the standard second-order second-derivative approximation. This system is then solved one Fourier mode at a time for all y. Then the standard pressure field is attained by an inverse Fourier transform.

The standard pressure model described thusfar is for the fluctuating part of the pressure. The mean pressure gradient model adds streamwise momentum to the flow at each timestep. This momentum source is uniform in space but is not necessarily constant in time. Instead, the momentum source is adjusted such that the bulk streamwise velocity $\int_\Omega w_1$ remains fixed in time.

When the standard finite-volume models are substituted into the filtered component energy equation and evaluated *a priori* using filtered DNS fields, the resulting terms are shown in Figure (4.9). The standard models are good approximations for the actual budget terms, except for close to the wall and for the turbulent dissipation and transport. The standard approximation to the nonlinear term conserves energy, both in total and component-wise. (See Appendix E for proof.) Therefore it is reasonable for the standard approximation to be a good model for production, which transfers energy from mean to fluctuations, caviat discrepancies near the wall. It also make sense that the rest of the nonlinear terms, convection, turbulent transport, and turbulent "dissipation" to be energy conserving as well. Therefore it is not a good model for turbulent "dissipation" or for dissipation by convection. In this sense, the nonlinear standard approximation terms behave qualitatively less like the terms in the filtered component energy equation and more like the terms in the continuous component energy equation.

Because of the discrepancies between the standard models and the actual terms, running the LES with these standard models alone gives poor predictions of velocity mean and variance. For more discussion on why LES without volumetric and wall modeling is inadequate, see section 4.3.5.1.

4.3.3 General Principles and Methodology for Constructing Models

The models described in the following sections may be interpreted as corrections or generalizations to the standard finite-volume models introduced in the previous section 4.3.2. We endeavour to hypothesize model forms/stencils based on the physical processes being modeled, solve for model coefficients based on DNS statistics, and test models in LES. These models for channel flow LES are customized for a particular discretization and numerical method and are potentially better than existing models. Before describing these improved models, we outline the general principles and procedure taken for constructing them.

4.3.3.1 Optimal LES

A model may have linear or quadratic or even higher order dependence on w_i. We have only studied up to quadratic dependence on w_i, because the actual non-

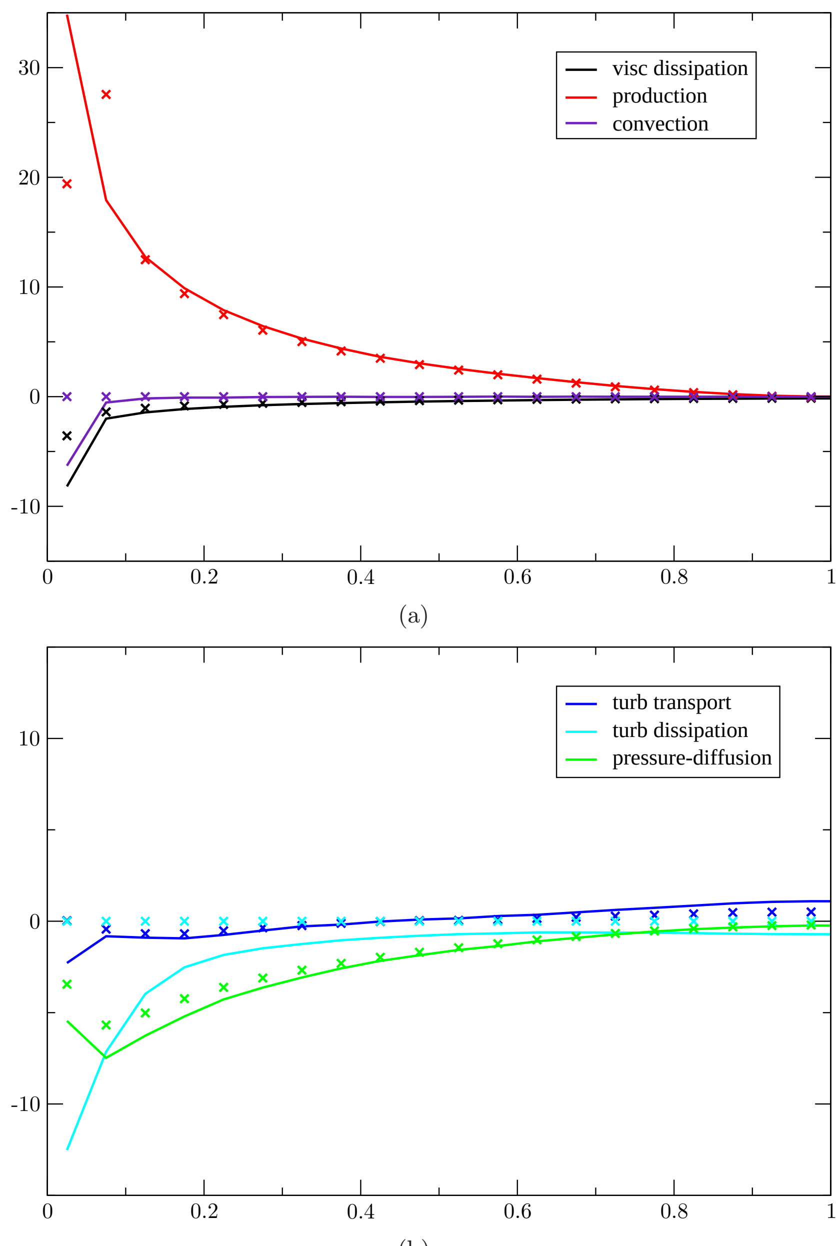

Figure 4.9: Terms in the filtered streamwise energy equation, actual (solid lines) versus standard models *a priori* ($\times$'s), for channel flow at $Re_\tau = 934$.

linear term has quadratic dependence on the velocities. The most general quadratic model for flux $\overline{u_i u_j}$ is

$$\overline{u_i u_j}^{mod} = \mathcal{A}_{ij} + \sum_{v_1} \mathcal{L}_{ijk}^{v_1} w_k^{v_1} + \sum_{v_1,v_2} \mathcal{Q}_{ijkl}^{v_1,v_2} w_k^{v_1} w_l^{v_2} \tag{4.30}$$

For the linear part of the model, each volume v_1 has an associated velocity component k. For the quadratic part of the model, volumes come in pairs v_1 and v_2, which have associated velocity components k and l respectively.

In the optimal LES formulation, the model is constructed in terms of $\tilde{u}_k$ instead of w_k, and error $(\overline{u_i u_j}^{mod} - \overline{u_i u_j})$ is minimized with respect to the model coefficients. The result is the following system of linear equations to determine the coefficients of the optimal model.

$$\langle \overline{u_i u_j} \rangle = \mathcal{A}_{ij} + \sum_{v_1} \mathcal{L}_{ijk}^{v_1} \langle \tilde{u}_k^{v_1} \rangle + \sum_{v_1,v_2} \mathcal{Q}_{ijkl}^{v_1,v_2} \langle \tilde{u}_k^{v_1} \tilde{u}_l^{v_2} \rangle \tag{4.31}$$

$$\langle \overline{u_i u_j} \tilde{u}_m^{v_3} \rangle = \mathcal{A}_{ij} \langle \tilde{u}_m^{v_3} \rangle + \sum_{v_1} \mathcal{L}_{ijk}^{v_1} \langle \tilde{u}_k^{v_1} \tilde{u}_m^{v_3} \rangle + \sum_{v_1,v_2} \mathcal{Q}_{ijkl}^{v_1,v_2} \langle \tilde{u}_k^{v_1} \tilde{u}_l^{v_2} \tilde{u}_m^{v_3} \rangle \tag{4.32}$$

$$\langle \overline{u_i u_j} \tilde{u}_m^{v_3} \tilde{u}_n^{v_4} \rangle = \mathcal{A}_{ij} \langle \tilde{u}_m^{v_3} \tilde{u}_n^{v_4} \rangle + \sum_{v_1} \mathcal{L}_{ijk}^{v_1} \langle \tilde{u}_k^{v_1} \tilde{u}_m^{v_3} \tilde{u}_n^{v_4} \rangle + \sum_{v_1,v_2} \mathcal{Q}_{ijkl}^{v_1,v_2} \langle \tilde{u}_k^{v_1} \tilde{u}_l^{v_2} \tilde{u}_m^{v_3} \tilde{u}_n^{v_4} \rangle \tag{4.33}$$

An optimal model, one with coefficients satisfying the above equations, shall be denoted with superscript *opt*: $\overline{u_i u_j}^{opt}$.

4.3.3.2 Stencils and Matching Statistics

Volker et al [66] showed the importance of constructing models with appropriate dependencies, and particularly to represent the subgrid contribution to critical terms in the filtered Reynolds stress transport equation and the filtered component energy equations (4.13). Zandonade [68] and Volker [66] found that local models are sufficient for LES modeling in forced isotropic turbulence and channel flow, respectively. Furthermore, local models are far less computationally expensive than global models. Therefore, we have focused our efforts on local models. These are the simplest linear model "$L20$", the simple linear model "$L22$", the linear Reynolds stress matching model "LRS", and the simple quadratic model "$Q22$".

Notice that the standard model $\overline{u_i u_j}^{mod}_{std}$, from equation (4.19), is just the general model, equation (4.30) with $\mathcal{A}_{ij} = 0$, $\mathcal{L}_{ijk} = 0$, and $\mathcal{Q}_{ijkl} = \frac{1}{4}$ for the following volume pairs: $\tilde{u}_i^{-j}\tilde{u}_j^{-i}$, $\tilde{u}_i^{-j}\tilde{u}_j^{+i}$, $\tilde{u}_i^{+j}\tilde{u}_j^{-i}$, $\tilde{u}_i^{+j}\tilde{u}_j^{+i}$. And therefore, the optimal model may be interpreted as a correction to the standard second-order approximation.

Now, consider adding constant and linear terms to the standard model. It is reasonable to assume that the model for $\overline{u_\alpha u_\beta}$ depends only on filtered velocities $\tilde{u}_\alpha$ and $\tilde{u}_\beta$. Let's further consider the smallest symmetric stencil associated with these components, which is composed of $\tilde{u}_\alpha^{+\beta}$, $\tilde{u}_\alpha^{-\beta}$, $\tilde{u}_\beta^{+\alpha}$, and $\tilde{u}_\beta^{-\alpha}$. (These are exactly the same cells used in the standard second-order approximation $\overline{u_\alpha u_\beta}^{mod}_{std}$.) This will be called the "simple" linear model or $L22$ and is shown in figure (4.10b).

$$\overline{u_\alpha u_\beta}^{mod}_{L22} = \mathcal{A}_{\alpha\beta} + \mathcal{L}^{-\beta}_{\alpha\beta\alpha}\tilde{u}_\alpha^{-\beta} + \mathcal{L}^{+\beta}_{\alpha\beta\alpha}\tilde{u}_\alpha^{+\beta} + \mathcal{L}^{-\alpha}_{\alpha\beta\beta}\tilde{u}_\beta^{-\alpha} + \mathcal{L}^{+\alpha}_{\alpha\beta\beta}\tilde{u}_\beta^{+\alpha} + \overline{u_\alpha u_\beta}^{mod}_{std} \tag{4.34}$$

The simple linear model $\overline{u_\alpha u_\beta}^{mod}_{L22}$ could in general have any value for its coefficients $\mathcal{A}_{\alpha\beta}$ and $\mathcal{L}_{\alpha\beta\gamma}$. If the coefficients solve the equations (4.31, 4.32, 4.33), then it is an "optimal" simple linear model, which we will denote with superscript *opt*: $\overline{u_\alpha u_\beta}^{opt}_{L22}$.

Optimal models which include dependence on $\tilde{u}_\alpha$ cells to either side of the flux face, $\tilde{u}_\alpha^{+\beta}$ and $\tilde{u}_\alpha^{-\beta}$, are guaranteed to statistically match *a priori* their respective terms in the component energy equations. (See Appendix D for proof.) A model

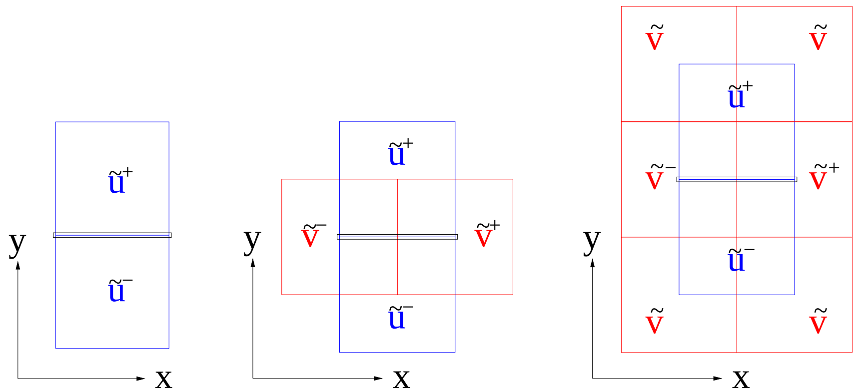

Figure 4.10: Three stencils for flux $\overline{uv}$ (left to right): (a) $L20$ simplest linear stencil which matches *a priori* the $\overline{uv}$ term in the $\langle \tilde{u}'\tilde{u}' \rangle$ component energy equation, (b) $L22$ simple linear stencil which includes dependency on both velocities $\tilde{u}$ and $\tilde{v}$, (c) LRS stencil which matches *a priori* the $\overline{uv}$ term in the Reynolds stress transport equation.

which depends linearly only on these two cells will be called the "simplest" linear model or $L20$.

$$\overline{u_\alpha u_\beta}^{mod}_{L20} = \mathcal{A}_{\alpha\beta} + \mathcal{L}^{-\beta}_{\alpha\beta\alpha}\tilde{u}^{-\beta}_\alpha + \mathcal{L}^{+\beta}_{\alpha\beta\alpha}\tilde{u}^{+\beta}_\alpha + \overline{u_\alpha u_\beta}^{mod}_{std} \tag{4.35}$$

Figure (4.10a) shows the stencil associated with the simplest linear model.

There are other more complex linear stencils. For instance, figure (4.10c) shows the Reynolds stress matching stencil LRS. It is the smallest stencil that is guaranteed, when optimized, to statistically match *a priori* the $\overline{uv}$ term in the filtered Reynolds stress transport equation (4.15).

Using the same stencil as for $L22$ but allowing the quadratic coefficients to be optimized (instead of standard) will be denoted $Q22$.

$$\begin{aligned}\overline{u_\alpha u_\beta}^{mod}_{Q22} &= \mathcal{A}_{\alpha\beta} + \mathcal{L}^{-\beta}_{\alpha\beta\alpha}\tilde{u}^{-\beta}_\alpha + \mathcal{L}^{+\beta}_{\alpha\beta\alpha}\tilde{u}^{+\beta}_\alpha + \mathcal{L}^{-\alpha}_{\alpha\beta\beta}\tilde{u}^{-\alpha}_\beta + \mathcal{L}^{+\alpha}_{\alpha\beta\beta}\tilde{u}^{+\alpha}_\beta \\ &+ \mathcal{Q}^{-\beta,-\alpha}_{\alpha\beta\alpha\beta}\tilde{u}^{-\beta}_\alpha\tilde{u}^{-\alpha}_\beta + \mathcal{Q}^{-\beta,+\alpha}_{\alpha\beta\alpha\beta}\tilde{u}^{-\beta}_\alpha\tilde{u}^{+\alpha}_\beta + \mathcal{Q}^{+\beta,-\alpha}_{\alpha\beta\alpha\beta}\tilde{u}^{+\beta}_\alpha\tilde{u}^{-\alpha}_\beta + \mathcal{Q}^{+\beta,+\alpha}_{\alpha\beta\alpha\beta}\tilde{u}^{+\beta}_\alpha\tilde{u}^{+\alpha}_\beta\end{aligned} \tag{4.36}$$

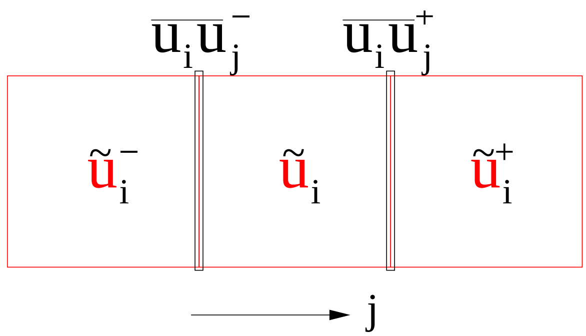

Figure 4.11: Configuration of simplest stencil cells $\tilde{u}_i$ with respect to the fluxes $\overline{u_i u_j}$.

4.3.3.3 Transport and Dissipation

The simplest way to decompose $\overline{u'_\alpha u'_\beta}$ into transport and dissipation in the component energy equations is

$$\tilde{u}'_\alpha \frac{\overline{u'_\alpha u'_\beta}^{+\beta} - \overline{u'_\alpha u'_\beta}^{-\beta}}{\Delta_\beta} = \underbrace{\frac{\frac{\tilde{u}'^{+\beta}_\alpha + \tilde{u}'_\alpha}{2}\overline{u'_\alpha u'_\beta}^{+\beta} - \frac{\tilde{u}'_\alpha + \tilde{u}'^{-\beta}_\alpha}{2}\overline{u'_\alpha u'_\beta}^{-\beta}}{\Delta_\beta}}_{transport} - \underbrace{\frac{\overline{u'_\alpha u'_\beta}^{+\beta}\frac{\tilde{u}'^{+\beta}_\alpha - \tilde{u}'_\alpha}{\Delta_\beta} + \overline{u'_\alpha u'_\beta}^{-\beta}\frac{\tilde{u}'_\alpha - \tilde{u}'^{-\beta}_\alpha}{\Delta_\beta}}{2}}_{dissipation} \tag{4.37}$$

Figure (4.11) shows the configuration for the involved cells and faces. With the discrete average $\underline{(\cdot)}_k$, defined in equation (4.16), this can be written more succinctly

$$\tilde{u}'_\alpha \tilde{\partial}_\beta \overline{u'_\alpha u'_\beta} = \tilde{\partial}_\beta(\overline{u'_\alpha u'_\beta}\,\underline{\tilde{u}'_\alpha}_{\beta}) - \underline{\overline{u'_\alpha u'_\beta}\tilde{\partial}_\beta \tilde{u}'_\alpha}_{\beta} \tag{4.38}$$

Transport and dissipation are two of the terms shown in figure (4.6). Substituting $\overline{u'_\alpha u'_\beta}^{mod}_{std}$ into the above equation (4.37), we calculated the two corresponding terms in figure (4.9). In the stencils section 4.3.3.2, it was noted that an optimal model with simplest stencil $\overline{u'_\alpha u'_\beta}^{opt}_{L20}$ will statistically match *a priori* the corresponding term in the component energy equations. It can further be shown that $\overline{u'_\alpha u'_\beta}^{opt}_{L20}$ will statistically match *a priori* transport and dissipation individually. This is because the same decomposition is used for the actual term and its model.

The viscous terms in the mean energy equation and component energy equations can be decomposed in the same way.

4.3.3.4 Dissipation and Stability

It is very important to consider stability when constructing models. An unstable model is useless in LES, even if it matches all the statistics of interest *a priori*.

Consider model terms on the right hand side of the filtered Navier Stokes equation (4.8). If the net linear coefficient on $\tilde{u}'_i$ is positive, then the LES may be unstable. If the net linear coefficient is negative, then the LES will likely be stable; if in addition the quadratic model is the standard model, then the LES will be stable.

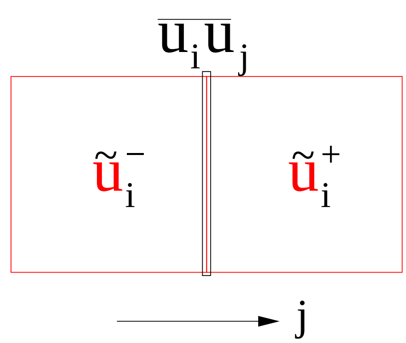

Figure 4.12: Configuration of simplest stencil cells $\tilde{u}_i$ with respect to flux $\overline{u_i u_j}$, which statistically matches the $\overline{u_i u_j}$ term in the component energy equations.

Now consider the simplest stencil ($L20$) for $\overline{u_i u_j}$ shown in figure (4.12). The following analysis is for j in a homogeneous direction. The nonlinear flux terms are shown on the right hand side of the Navier Stokes equation

$$\frac{\partial \tilde{u}_i}{\partial t} = \frac{1}{\Delta_j} \sum_{j=1}^{3} (\overline{u_i u_j}^- - \overline{u_i u_j}^+) + ... \tag{4.39}$$

Figure (4.13) shows the configuration of the simplest stencil relative to the fluxes, where notation has slightly changed because we are dealing with fluxes both in and out of cell $\tilde{u}'$.

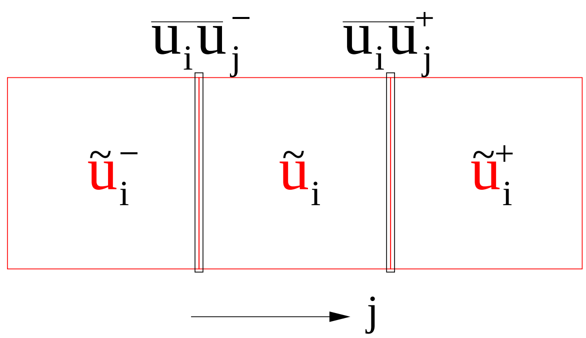

Figure 4.13: Configuration of simplest stencil cells $\tilde{u}_i$ with respect to the fluxes $\overline{u_i u_j}$.

Substituting the simplest optimal model ($L20$) on the right hand side yields

$$\begin{aligned} \overline{u_i u_j}^- - \overline{u_i u_j}^+ \approx \overline{u_i u_j}^{opt-}_{L20} - \overline{u_i u_j}^{opt+}_{L20} &= L^- \tilde{u}_i'^- + L^+ \tilde{u}_i' - L^- \tilde{u}_i' - L^+ \tilde{u}_i'^+ \\ &+ \overline{u_i u_j}^{mod-}_{std} - \overline{u_i u_j}^{mod+}_{std} \end{aligned} \tag{4.40}$$

$(L^+ - L^-)$ is the coefficient on $\tilde{u}_i'$ from the right hand side of equation (4.40) and should be non-positive to ensure stability. To look at it another way, rearrange the linear part of the model

$$\begin{aligned} \overline{u_i u_j}^{opt-}_{L20} - \overline{u_i u_j}^{opt+}_{L20} &= \underbrace{\frac{L^- - L^+}{2}}_{D\ diffusivity} (\tilde{u}_i'^- - 2\tilde{u}_i' + \tilde{u}_i'^+) + \underbrace{\frac{L^- + L^+}{2}}_{C\ convectivity} (\tilde{u}_i'^- - \tilde{u}_i'^+) \\ &+ \overline{u_i u_j}^{mod-}_{std} - \overline{u_i u_j}^{mod+}_{std} \end{aligned} \tag{4.41}$$

The first term on the right hand side is a diffusion term, and the second a convection term. Of particular concern is that the "diffusivity" factor $D = \frac{L^- - L^+}{2}$ in front of the first term be non-negative, because a negative factor represents anti-diffusion which may lead to linear instability.

We will now show that the sign of D in equation (4.41) is opposite the sign of the budget term for the linear part of the model. Multiplying the linear part of the model from equation (4.41) by $\tilde{u}'_i$ and taking the expected value yields the budget term for the linear part of the model (no summation in i)

$$D \underbrace{\left\langle \tilde{u}'_i(\tilde{u}'^-_i - 2\tilde{u}'_i + \tilde{u}'^+_i)\right\rangle}_{2\left\langle \tilde{u}'_i \tilde{u}'^-_i \right\rangle - 2\left\langle \tilde{u}'_i \tilde{u}'_i \right\rangle < 0} + C \underbrace{\left\langle \tilde{u}'_i(\tilde{u}'^-_i - \tilde{u}'^+_i)\right\rangle}_{\left\langle \tilde{u}'_i \tilde{u}'^-_i \right\rangle - \left\langle \tilde{u}'_i \tilde{u}'^+_i \right\rangle = 0} \tag{4.42}$$

where the individual expressions multiplying D and C are negative and zero respectively if j is a direction of homogeneity. Therefore, $D > 0$ corresponds to a dissipative linear model, and $D < 0$ corresponds to an anti-dissipative linear model.

The preceeding statement can often, but not always, be extended to the dissipativeness or anti-dissipativeness of the actual nonlinear term. Multiplying through equation (4.41) by $\tilde{u}'_i$, taking the expected value, and dividing by Δ_j yields (no summation in i or j)

$$-\left\langle \tilde{u}'_i \tilde{\partial}_j \overline{u_i u_j} \right\rangle = -\left\langle \tilde{u}'_i \tilde{\partial}_j \overline{u_i u_j}^{opt}_{L20} \right\rangle = \frac{D}{\Delta_j} \underbrace{\left\langle \tilde{u}'_i(\tilde{u}'^-_i - 2\tilde{u}'_i + \tilde{u}'^+_i)\right\rangle}_{<0} - \left\langle \tilde{u}'_i \tilde{\partial}_j \overline{u_i u_j}^{mod}_{std} \right\rangle \tag{4.43}$$

where the left equality results from the optimal model matching the budget terms (proven in Appendix D). The convection term (not shown) is zero. The budget term for the standard nonlinear model tends to be similar to the actual term but smaller in magnitude (no summation in i or j)

$$0 < \frac{\left\langle \tilde{u}_i' \tilde{\partial}_j \overline{u_i u_j}^{mod}_{std} \right\rangle}{\left\langle \tilde{u}_i' \tilde{\partial}_j \overline{u_i u_j} \right\rangle} < 1 \tag{4.44}$$

When this is the case, the sign of D will be opposite the sign of the actual budget term in equation (4.43).

4.3.3.5 Pressure Modeling

The pressure term in the component energy equations (4.13) transfers energy among the fluctuating components. As such, it is important for correctly predicting the LES velocity variances. In section 4.3.2, the standard pressure model was shown to be a good approximation for the actual pressure term.

The standard pressure model applied to the actual filtered nonlinear fields $D_{ki}\tilde{\partial}_j\overline{u_i u_j}$ quite closely models the actual filtered pressure gradient $\tilde{\partial}_k\overline{p}$, as shown in figure (4.14). Here, the operator D_{ki} defined by

$$D_{ki} = \tilde{\partial}_k(\tilde{\partial}_m\tilde{\partial}_m)^{-1}\tilde{\partial}_i \tag{4.45}$$

returns the divergent part of vector argument and involves the solution of a Poisson equation with specific boundary conditions described in section 4.3.2.

Figure (4.14) also shows the standard pressure model applied to the standard nonlinear *model*, $D_{ki}\tilde{\partial}_j\overline{u_i u_j}^{mod}_{std}$. Notice the errors in all three component energy equations. We infer from this that errors in "pressure modeling" result primarily from problems with the nonlinear model and not with the standard pressure model itself. This means the standard pressure model will be a good model for the actual

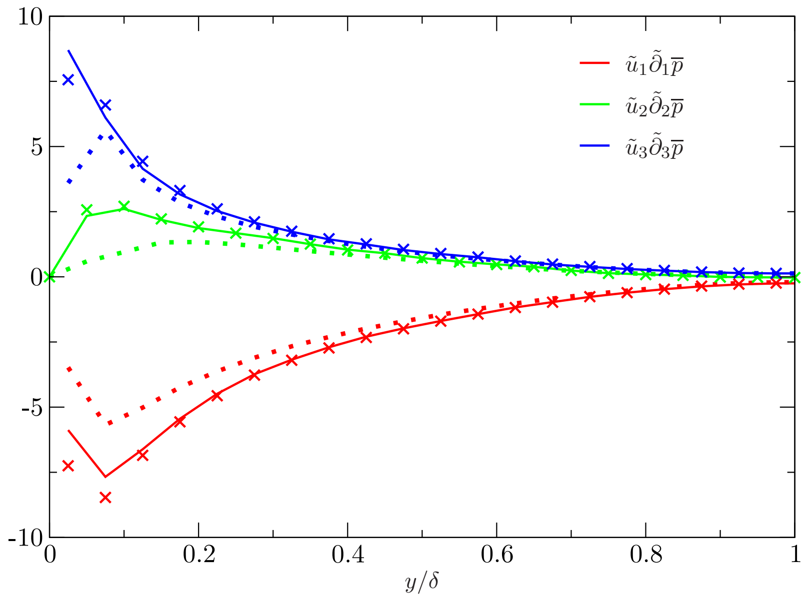

Figure 4.14: Actual filtered pressure $\overline{p}$ (solid curve), standard pressure model applied to actual nonlinear term ($\times$'s), and standard pressure model applied to standard nonlinear model (dotted curve) in filtered component energy equations for channel flow at $Re_\tau = 934$. The gradient of the standard pressure model is the divergent part of the nonlinear term it acts upon, $\tilde{\partial}_k\phi = -D_{ki}\tilde{\partial}_j\overline{u_i u_j}$.

filtered pressure as long as we have a "good enough" model for the nonlinear term. Therefore, the standard pressure model was not modified.

To evaluate the "pressure model", we actually compare budget terms for the divergent part of the nonlinear models $\left\langle \tilde{u}'_k D_{ki}(-\tilde{\partial}_j\overline{u_i u_j}^{mod})\right\rangle$ with the divergent part of the actual nonlinear terms $\left\langle \tilde{u}'_k D_{ki}(-\tilde{\partial}_j\overline{u_i u_j})\right\rangle$, just as we have done in figure (4.14). In some cases, it is sufficient to construct models for the nonlinear term without explicitly considering it's divergent part, with the result that it's divergent part would turn out close to correct. But this was not always the case.

In section 4.3.3.2, it was shown that models can be constructed in order to match *a priori* the nonlinear term in the component energy equations.

$$\left\langle \tilde{u}'_\alpha \tilde{\partial}_\beta \overline{u_\alpha u_\beta} \right\rangle = \left\langle \tilde{u}'_\alpha \tilde{\partial}_\beta \overline{u_\alpha u_\beta}^{mod} \right\rangle \tag{4.46}$$

This can also be done for the divergent part of the nonlinear term.

$$\left\langle \tilde{u}'_\gamma D_{\gamma\alpha}(\tilde{\partial}_\beta \overline{u_\alpha u_\beta}) \right\rangle = \left\langle \tilde{u}'_\gamma D_{\gamma\alpha}(\tilde{\partial}_\beta \overline{u_\alpha u_\beta}^{mod}) \right\rangle \tag{4.47}$$

Solving for such a model is much more complicated because the pressure term has global effect. See section 4.3.4.8 for details.

4.3.3.6 Reynolds Decomposition

The Reynolds decomposition of velocity u is

$$u = \langle u \rangle + u' \tag{4.48}$$

where $U \equiv \langle u \rangle$ is the mean, and the remainder u' is the fluctuation.

Decomposing the viscous term gives

$$\overline{\partial_j u_i} = \underbrace{\overline{\partial_j U_i}}_{mean} + \underbrace{\overline{\partial_j u'_i}}_{fluctuating} \tag{4.49}$$

It is important to model these two parts separately, because the mean part effects the mean momentum equation, while the fluctuating part effects the component energy equations. Furthermore, the mean part is deterministic while the fluctuating part is stochastic. Therefore the mean part can be modeled exactly (given exact statistics), but the stochastic fluctuating part cannot, because small scale information is missing from the LES. Optimal models, described in section 4.3.3.1, minimize the error in the fluctuating models based on filtered turbulence statistics. The mean model will be written in terms of the filtered mean velocities $\tilde{U}_i$, while the fluctuating model will be written in terms of the filtered fluctuating velocities $\tilde{u}'_i$.

Likewise, decomposing the nonlinear term gives

$$\overline{u_i u_j} = \overline{U_i U_j} + \underbrace{\overline{U_i u'_j}}_{production} + \underbrace{\overline{u'_i U_j}}_{convection} + \underbrace{\overline{u'_i u'_j}}_{turbulent\, transport/dissipation} \tag{4.50}$$

The first term $\overline{U_i U_j}$ acts only in the mean momentum equation, while the latter three act in the component energy equations (4.13), with corresponding labels. It is important to model each term separately because of the different physical processes they represent.

$\overline{U_i U_j}$ is deterministic and will be modeled in terms of the filtered mean velocities $\tilde{U}_i$ and $\tilde{U}_j$. The last term $\overline{u'_i u'_j}$ is stochastic and will be modeled in terms of the filtered fluctuating velocities $\tilde{u}'_i$ and $\tilde{u}'_j$. The production term $\overline{U_i u'_j}$ is stochastic, although it has a deterministic factor U_i. It is modeled in terms of $\tilde{U}_i$ and $\tilde{u}'_j$. The convection term $\overline{u'_i U_j}$ is stochastic, with deterministic factor U_j, and should be modeled in terms of $\tilde{u}'_i$ and $\tilde{U}_j$.

Figure (4.15) shows the nonlinear mean-fluctuating (convection plus production) and fluctuating-fluctuating (turbulent transport/dissipation) terms and corresponding pressure terms in the filtered component energy equations, actual versus standard nonlinear model. Notice that the mean-fluctuating terms are fairly well-approximated by the standard nonlinear model. The pressure terms are quite accurate down to one cell from the wall. And the nonlinear term in the $\langle \tilde{u}'\tilde{u}' \rangle$ equation is fairly accurate down to two cells away from the wall. In the $\langle \tilde{v}'\tilde{v}' \rangle$ and $\langle \tilde{w}'\tilde{w}' \rangle$ equations, there is no convective energy removal by the standard nonlinear term, but this should be readily fixed using linear models in $\tilde{v}'$ and $\tilde{w}'$ respectively. In constrast, the fluctuating-fluctuating terms, nonlinear and pressure, are quite poorly approximated by the standard nonlinear model, which provides additional motivation for separately modeling the mean-fluctuating and fluctuating-fluctuating terms. This also indicates how similar or different an improved model will be from the standard nonlinear model.

4.3.4 Improved Models

Having laid out the general principles and procedures for constructing models, we will now describe our models for the Reynolds decomposed viscous and nonlinear terms.

4.3.4.1 Mean Viscous Model

The mean momentum equation comes from taking the expected value of the Navier Stokes equation (4.8)

$$\partial_t \tilde{U}_i = -\tilde{\partial}_j \overline{U_i U_j} - \tilde{\partial}_j \left\langle \overline{u_i' u_j'} \right\rangle - \tilde{\partial}_i \overline{P} + \frac{1}{Re} \tilde{\partial}_j \overline{\partial_j U_i} \tag{4.51}$$

The mean viscous model represents the right most term in this equation as the sum of the standard model plus a constant

$$\overline{\partial_j U_i}_A^{mod} = \mathcal{A}_{ij} + \overline{\partial_j U_i}_{std}^{mod} \tag{4.52}$$

Figure (4.16) shows the actual filtered term $\overline{\partial_2 U_1}$ and the standard model $\overline{\partial_2 U_1}_{std}^{mod}$. The standard model predicts well the velocity gradient throughout the channel, except for the two points closest to the wall. In an optimal model, the constant $\mathcal{A}_{ij}$ equals the difference between the actual and standard models evaluated *a priori.*

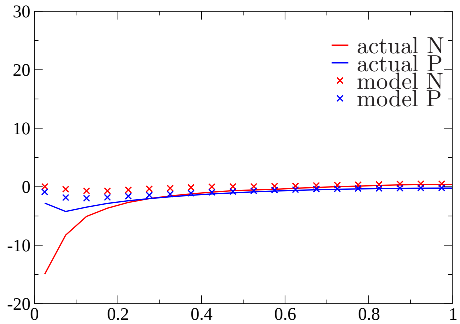

(a) fluctuating-fluctuating term in $\tilde{u}'\tilde{u}'$ eqn

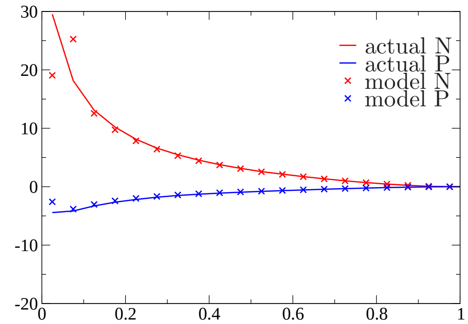

(b) mean-fluctuating term in $\tilde{u}'\tilde{u}'$ equation

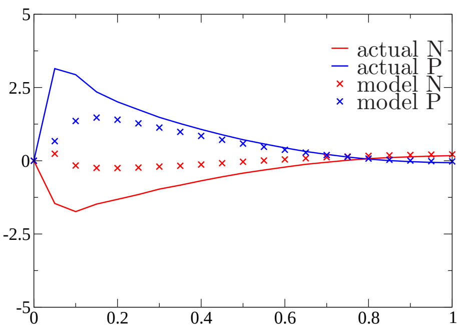

(c) fluctuating-fluctuating term in $\tilde{v}'\tilde{v}'$ eqn

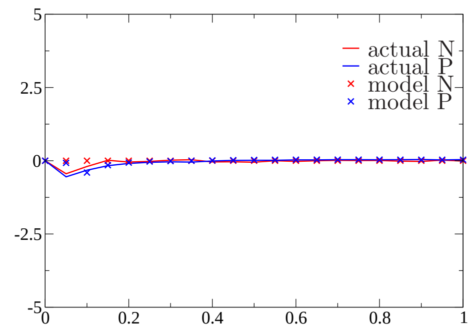

(d) mean-fluctuating term in $\tilde{v}'\tilde{v}'$ equation

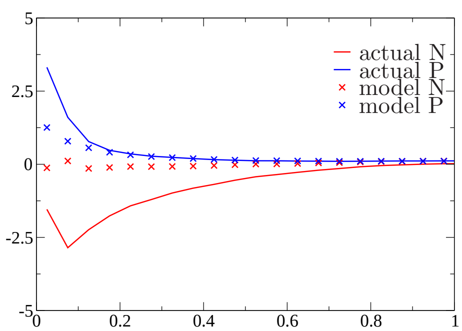

(e) fluctuating-fluctuating term in $\tilde{w}'\tilde{w}'$ eqn

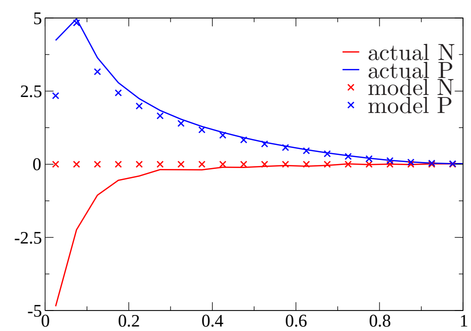

(f) mean-fluctuating term in $\tilde{w}'\tilde{w}'$ equation

Figure 4.15: Actual and standard model *a priori* terms for nonlinear (N) and pressure (P) terms in component energy equations for filtered DNS of channel flow at $Re_\tau = 934$. The left column is for the fluctuating-fluctuating parts of the nonlinear term, and the right column is for the mean-fluctuating parts of the nonlinear term.

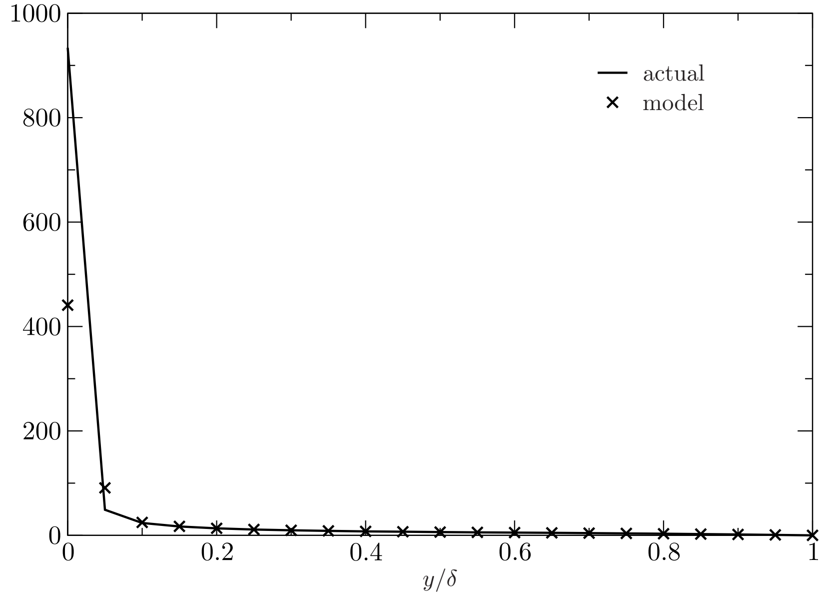

Figure 4.16: Profiles for mean velocity gradient, actual $\overline{\partial_2 U_1}$ and standard model $\overline{\partial_2 U_1}^{mod}_{std}$ *a priori*, for channel flow at $Re_\tau = 934$.

Recall that in the Reynolds decomposition section 4.3.3.6, we had determined that the mean viscous flux term $\overline{\partial_\beta U_\alpha}$ should be modeled in terms of neighboring mean velocities $\tilde{U}_\alpha$. The simplest local model linear in $\tilde{U}_\alpha$ is

$$\overline{\partial_\beta U_\alpha}^{mod}_{L20} = \mathcal{L}^{-\beta}_{\alpha\beta\alpha} \tilde{U}^{-\beta}_\alpha + \mathcal{L}^{+\beta}_{\alpha\beta\alpha} \tilde{U}^{+\beta}_\alpha \tag{4.53}$$

which subsumes the standard viscous model $\overline{\partial_\beta U_\alpha}^{mod}_{std}$, because $\overline{\partial_\beta U_\alpha}^{mod}_{std}$ is also local and linear in $\tilde{U}_\alpha$. If the mean velocities $\tilde{U}_\alpha$ do not deviate significantly from the initial filtered DNS field, the two models $\overline{\partial_\beta U_\alpha}^{mod}_{A}$ and $\overline{\partial_\beta U_\alpha}^{mod}_{L20}$ should give similar LES results. However, if there is significant deviation, $\overline{\partial_\beta U_\alpha}^{mod}_{L20}$ should be the better, more responsive LES model.

4.3.4.2 Fluctuating Viscous Model

The fluctuating viscous term is modeled as follows

$$\overline{\partial_\beta u'_\alpha}^{mod}_{L20} = \mathcal{L}^{-\beta}_{\alpha\beta\alpha}\tilde{u}'^{-\beta}_\alpha + \mathcal{L}^{+\beta}_{\alpha\beta\alpha}\tilde{u}'^{+\beta}_\alpha \qquad (4.54)$$

Notice that this model subsumes the standard model $\overline{\partial_\beta u'_\alpha}^{mod}_{std}$, which is also linear in the neighboring velocities $\tilde{u}'_\alpha$. Figure (4.17) shows the actual viscous term and the corresponding viscous model term in the component energy equations (4.13).

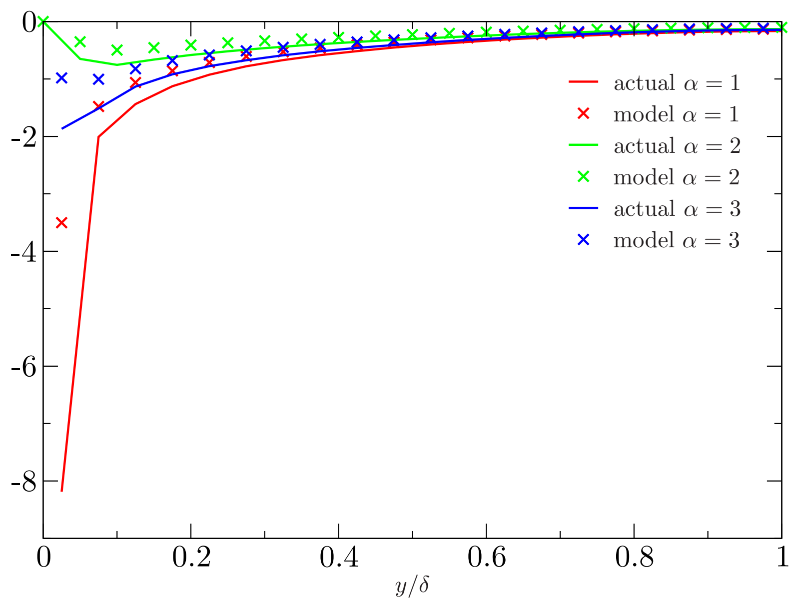

Figure 4.17: Profiles for actual filtered viscous term $\left\langle \tilde{u}_\alpha \tilde{\partial}_j \overline{\partial_j u'_\alpha} \right\rangle$ and standard viscous model term $\left\langle \tilde{u}_\alpha \tilde{\partial}_j \overline{\partial_j u'_\alpha}^{mod}_{std} \right\rangle$ *a priori* in the component energy equations for channel flow at $Re_\tau = 934$.

The standard model consistently underpredicts the magnitude of the viscous term in the component energy equations, and thus underrepresents the amount of energy removal due to these terms. A linear optimal model statistically matches the actual term *a priori*.

$$\left\langle \tilde{u}'_\alpha \tilde{\partial}_\beta \overline{\partial_\beta u'_\alpha}^{opt}_{L20} \right\rangle = \left\langle \tilde{u}'_\alpha \tilde{\partial}_\beta \overline{\partial_\beta u'_\alpha} \right\rangle \tag{4.55}$$

This is proven in Appendix D.

Modeling the viscous terms (mean and fluctuating) is relatively straightforward. We use the simplest linear models, as nothing more is necessary according to the form of the actual term. Since all of the viscous terms are dissipative, their optimal models are also dissipative and therefore stable. The relationship between dissipation and stability is discussed in greater detail in section 4.3.3.4.

Models for the viscous terms $\overline{\partial_j U_i}$ and $\overline{\partial_j u'_i}$ are constructed all the way to the wall, where they represent the wall shear stress τ_w. We also implemented a log law model and found that the choice of wall model does affect the LES solution but not greatly. This is similar to the findings of Cabot and Moin, [12].

4.3.4.3 Nonlinear Mean-Mean Model

A model for the mean-mean flux term $\overline{U_i U_j}$ should depend on products of local filtered mean velocities $\tilde{U}_i^{\pm j}$ and $\tilde{U}_j^{\pm i}$. This term was not actually modeled, because the associated force term $\tilde{\partial}_j \overline{U_i U_j}$ is zero for channel flow.

4.3.4.4 Nonlinear Mean-Fluctuating Model

The nonlinear mean-fluctuating term is $\overline{U_i u'_j}$. This term is responsible for production in the filtered component energy equations (4.13). On the other hand, the fluctuating-fluctuating term $\overline{u'_i u'_j}$ is responsible for production in the filtered mean momentum equation (4.51). Figure (4.18) shows the production terms in the two equations. Notice that more energy leaves the mean $\underline{\left\langle \overline{u'v'} \right\rangle \tilde{\partial}_2 \tilde{U}}_2$ than enters the fluctuating $\left\langle \tilde{u}_1' \tilde{\partial}_j \overline{U_1 u_j'} \right\rangle$; the difference represents the energy that goes directly from mean to subgrid fluctuations.

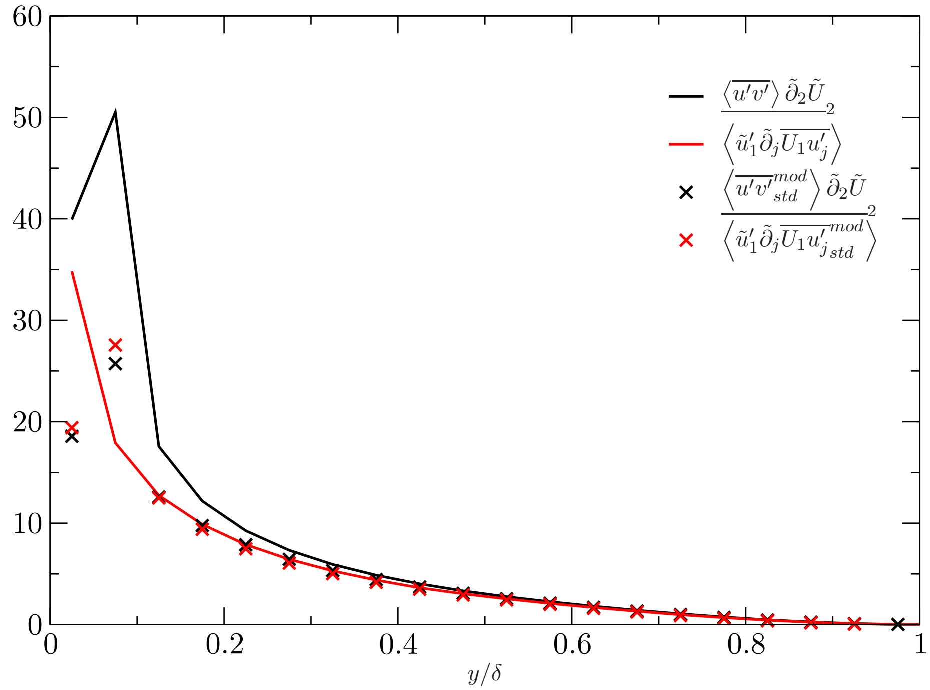

Figure 4.18: Production in mean equation $\left\langle \overline{u'v'} \right\rangle \tilde{\partial}_2 \tilde{U}$ and streamwise energy equation $\left\langle \tilde{u}_1' \tilde{\partial}_j \overline{U_1 u_j'} \right\rangle$, compared with the same production terms evaluated *a priori* using standard nonlinear models $\left\langle \overline{u'v'}_{std}^{mod} \right\rangle \tilde{\partial}_2 \tilde{U}$ and $\left\langle \tilde{u}_1' \tilde{\partial}_j \overline{U_1 u_j'}_{std}^{mod} \right\rangle$, for channel flow at $Re_\tau = 934$.

The production term in the filtered mean equation is indeed consistent with production, as it has exactly the same form as the unfiltered production $\langle u'v' \rangle \partial_2 U$. The term in the filtered component energy equation is less clear, but we can show that the analogous term becomes the production in the continuous component energy equation.

$$\left\langle u_i'\partial_j(U_iu_j')\right\rangle = \left\langle u_i'(u_j'\partial_jU_i + U_i\underbrace{\partial_ju_j'}_{0})\right\rangle = \left\langle u_i'u_j'\right\rangle\partial_jU_i = \left\langle u_1'u_2'\right\rangle\partial_2U_1 \qquad (4.56)$$

The last equality is a simplification for channel flow. Likewise, the filtered production term can be manipulated to a form similar to the familiar form shown above.

$$\tilde{u}_1'\tilde{\partial}_j\overline{U_1u_j'} = \tilde{u}_1'\widetilde{\partial_jUu_j'} = \tilde{u}_1'[\widetilde{u_j'\partial_jU + U\underbrace{\partial_ju_j'}_{0}}] = \tilde{u}_1'\widetilde{u_j'\partial_jU} = \tilde{u}_1'\widetilde{u_2'\partial_2U_1} \qquad (4.57)$$

Production resulting from the standard nonlinear model is also shown in figure (4.18). One can see that the difference between the actual production terms (mean and fluctuating) is large, while the difference between the respective standard models is small. In fact, one might expect the standard model for these two terms be to close since the standard nonlinear model conserves energy, both total and component-wise, integrated over the domain. (Proof of energy conservation is shown in Appendix E.)

Following similar steps to that for the continous equation (4.56), we will now show (in 2-D), how the discrete divergence-free condition simplifies the standard nonlinear model. Consider $\tilde{\partial}_k\overline{U_1u_k'}^{mod}_{std}$ on the center cell of the stencil shown in figure (4.19).

$$\tilde{\partial}_k\overline{U_1u_k'}^{mod}_{std} = \tilde{U}^{i,j}\frac{(\tilde{u}'^{i+1,j}+\tilde{u}'^{i,j})-(\tilde{u}'^{i,j}+\tilde{u}'^{i-1,j})}{2\Delta_x}$$
$$+\frac{(\tilde{U}^{i,j+1}+\tilde{U}^{i,j})(\tilde{v}'^{i,j+1}+\tilde{v}'^{i-1,j+1})}{4\Delta_y}-\frac{(\tilde{U}^{i,j}+\tilde{U}^{i,j-1})(\tilde{v}'^{i,j}+\tilde{v}'^{i-1,j})}{4\Delta_y} \qquad (4.58)$$

where superscripts i and j indicate position. Incorporating the discrete divergence-free condition $\frac{\tilde{u}'^{i+1,j}+\tilde{u}'^{i,j}}{\Delta_x} + \frac{\tilde{v}'^{i,j+1}+\tilde{v}'^{i,j}}{\Delta_y} = 0$ simplifies the above equation

$$\tilde{\partial}_k \overline{U_1 u'_k}^{mod}_{std} = \frac{(\tilde{U}^{i,j+1} - \tilde{U}^{i,j})(\tilde{v}'^{i,j+1} + \tilde{v}'^{i-1,j+1})}{4\Delta_y} + \frac{(\tilde{U}^{i,j} - \tilde{U}^{i,j-1})(\tilde{v}'^{i,j} + \tilde{v}'^{i-1,j})}{4\Delta_y} \tag{4.59}$$

The discrete divergence-free condition removes the $\overline{U_1 u'_j}^{mod}_{std}$ components in directions j where the field is homogeneous, leaving only the term like $u'_2\partial_2 U_1$, two being the direction of inhomogeneity. Figure (4.18) had shown the sum over the components j of $\left\langle \tilde{u}'_1 \tilde{\partial}_j \overline{U_1 u'_j} \right\rangle$ and $\left\langle \tilde{u}'_1 \tilde{\partial}_j \overline{U_1 u'_j}^{mod}_{std} \right\rangle$. Figure (4.20) shows each component. Notice (with both actual and model) that the components $j = 2$ and $j = 3$ are large with opposite signs, such that the sum has much smaller magnitude than either one. Further, the primary error between actual and model is for $j = 2$.

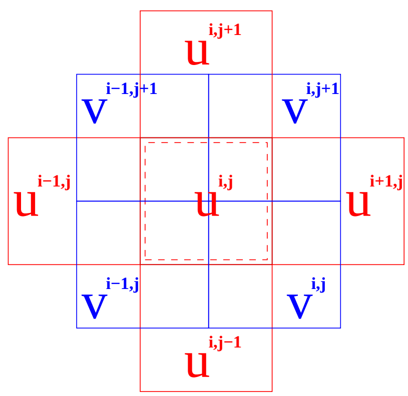

Figure 4.19: Configuration of cells used in standard nonlinear model for calculation of energy centered on cell $\tilde{u}^{i,j}$

We are now in a position to propose a modified model for the mean-fluctuating term

$$\overline{U_\alpha u'_\beta}^{mod} = \mathcal{L}^{-\alpha}_{\alpha\beta\beta} \tilde{u}'^{-\alpha}_\beta + \mathcal{L}^{+\alpha}_{\alpha\beta\beta} \tilde{u}'^{+\alpha}_\beta + \overline{U_\alpha u'_\beta}^{mod}_{std} \tag{4.60}$$

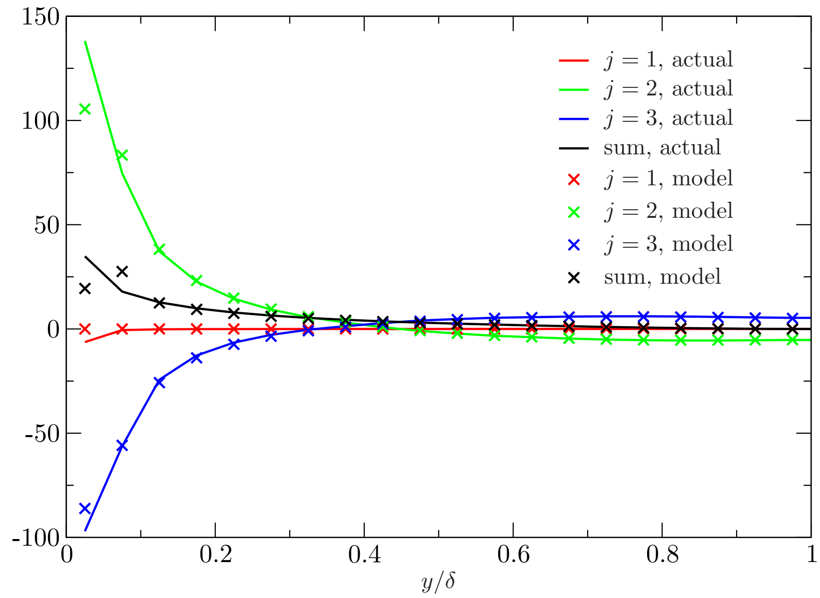

Figure 4.20: Components of $\left\langle \tilde{u}_1' \tilde{\partial}_j \overline{U_1 u_j'} \right\rangle$ and $\left\langle \tilde{u}_1' \tilde{\partial}_j \overline{U_1 u_j'}^{mod}_{std} \right\rangle$, for channel flow at $Re_\tau = 934$.

Notice that the linear terms in the above equation may be subsumed as part of a general quadratic model $\overline{U_\alpha u_\beta'}^{mod}_{Q22}$, or vice versa (quadratics subsumed by the linears). We will do the first, because the quadratic model contains explicit dependence on $\tilde{U}_i$ and therefore should have better dynamic behavior.

$$\overline{U_\alpha u_\beta'}^{mod}_{Q22} = \mathcal{Q}^{-\beta,-\alpha}_{\alpha\beta\alpha\beta} \tilde{U}^{-\beta}_\alpha \tilde{u}'^{-\alpha}_\beta + \mathcal{Q}^{-\beta,+\alpha}_{\alpha\beta\alpha\beta} \tilde{U}^{-\beta}_\alpha \tilde{u}'^{+\alpha}_\beta + \mathcal{Q}^{+\beta,-\alpha}_{\alpha\beta\alpha\beta} \tilde{U}^{+\beta}_\alpha \tilde{u}'^{-\alpha}_\beta + \mathcal{Q}^{+\beta,+\alpha}_{\alpha\beta\alpha\beta} \tilde{U}^{+\beta}_\alpha \tilde{u}'^{+\alpha}_\beta \tag{4.61}$$

Here the standard quadratic model will be modified only for the term $\beta = 2$ for the following reasons. (1) Only the $\beta = 2$ term in $\overline{U_\alpha u_\beta'}^{mod}_{std}$ survives after accounting for the divergence-free condition. (2) The standard model for the $\beta = 2$ commits the largest error. (3) The net production is a result of cancelation of large magnitude components ($\beta = 2$ positive and $\beta = 3$ negative), which if modeled separately may result in stability problems for $\beta = 2$ since it is energy producing. Therefore we will model the net production $\sum_{\beta=1}^{3} \left\langle \tilde{u}_1' \tilde{\partial}_\beta \overline{U_1 u_\beta'} \right\rangle$ by modifying only the $\beta = 2$ term.

In the case of channel flow

$$\overline{Uv'} = \overline{U} \cdot \overline{v'} \tag{4.62}$$

Therefore, modeling $\overline{Uv'}$ can be very cleanly decomposed into modeling it's two components $\overline{U}$ and $\overline{v'}$ separately. In fact, the standard model $\overline{Uv'}_{std}^{mod}$ is the product of two other standard models

$$\overline{Uv'}_{std}^{mod} = \overline{U}_{std}^{mod} \cdot \overline{v'}_{std}^{mod} \tag{4.63}$$

where

$$\overline{U}_{std}^{mod} = 0.5(\tilde{U}^{+} + \tilde{U}^{-}) \tag{4.64}$$

and

$$\overline{v'}_{std}^{mod} = 0.5(\tilde{v}'^{+} + \tilde{v}'^{-}) \tag{4.65}$$

The stencil is shown in figure (4.10).

It has been found that much of the error in the standard flux model $\overline{Uv'}_{std}^{mod}$ is related to not correctly approximating $\overline{U}$. Figure (4.21) shows profiles of $\overline{U}$ and it's standard model. The standard model approximates $\overline{U}$ quite well throughout most of the channel, but not close to the wall. A corrected model for $\overline{U}$ may be written

$$\overline{U}_{\gamma}^{mod} = \gamma(\tilde{U}^{+} + \tilde{U}^{-}) \tag{4.66}$$

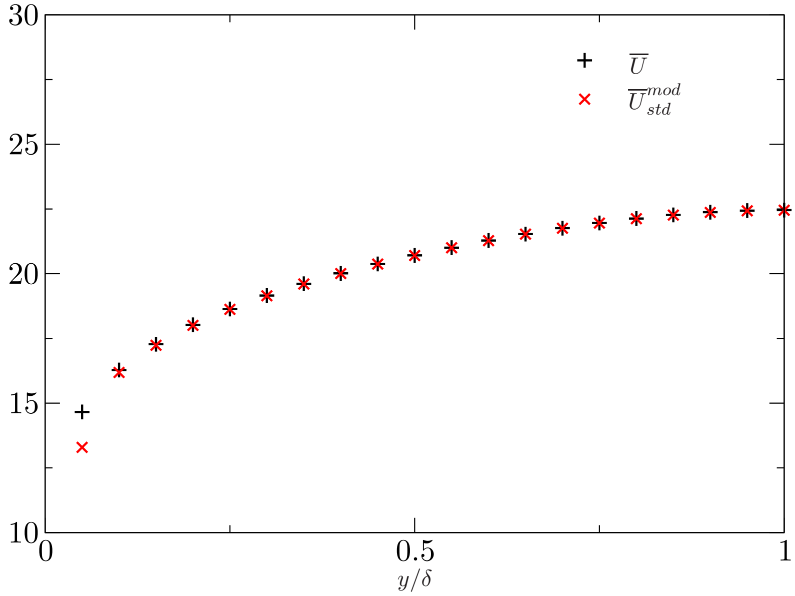

Figure 4.21: Mean velocity profiles, face filtered $\overline{U}$ and standard model $\overline{U}_{std}^{mod}$ *a priori*, for channel flow at $Re_\tau = 934$.

where γ is chosen to exactly match $\overline{U}$. For example, $\gamma = 0.55$ at $y/\delta = 0.05$.

Using $\overline{U}_{\gamma}^{mod}\overline{v'}_{std}^{mod}$ to model $\overline{U_1 u'_\beta}$ for $\beta = 2$, and standard nonlinear models for $\beta \neq 2$ results in a better overall production model, which we will call the "$Q\gamma$ model". Figure (4.22) shows production resulting from the $Q\gamma$ model, the standard model, and the actual mean-fluctuating term. Notice that $\left\langle \tilde{u}'_1 \tilde{\partial}_\beta \overline{U_1 u'_\beta}_{Q\gamma}^{mod} \right\rangle$ for $\beta = 2$, as well as the sum over β, are greatly improved over the standard nonlinear model.

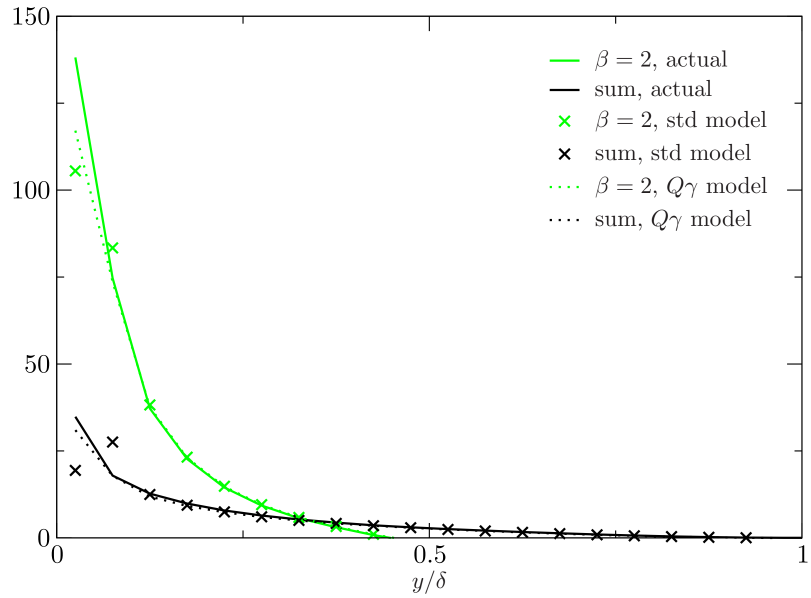

Figure 4.22: Actual production $\left\langle \tilde{u}'_1 \tilde{\partial}_\beta \overline{U_1 u'_\beta} \right\rangle$ terms, compared with *a priori* evaluation of production using the standard nonlinear model $\left\langle \tilde{u}'_1 \tilde{\partial}_\beta \overline{U_1 u'_\beta}^{mod}_{std} \right\rangle$ and the $Q\gamma$ model $\left\langle \tilde{u}'_1 \tilde{\partial}_\beta \overline{U_1 u'_\beta}^{mod}_{Q\gamma} \right\rangle$, for channel flow at $Re_\tau = 934$.

4.3.4.5 Nonlinear Fluctuating-Mean Model

The analog of the fluctuating-mean term in the continuous component energy equations results in the convective term.

$$-\left\langle u'_\alpha \partial_j (u'_\alpha U_j) \right\rangle = -\left\langle u'_\alpha (U_j \partial_j u'_\alpha + u'_\alpha \underbrace{\partial_j U_j}_{0}) \right\rangle = -U_j \left\langle u'_\alpha \partial_j u'_\alpha \right\rangle = U_j \partial_j \frac{1}{2} \left\langle u'_\alpha u'_\alpha \right\rangle \tag{4.67}$$

Note that in the continuous equations, this term conserves energy. However, in the filtered equations, $-\left\langle \tilde{u}'_\alpha \tilde{\partial}_j \overline{u'_\alpha U_j} \right\rangle$ removes energy at a significant rate, especially close to the walls. Figure (4.23) shows the convective term in the three component energy equations.

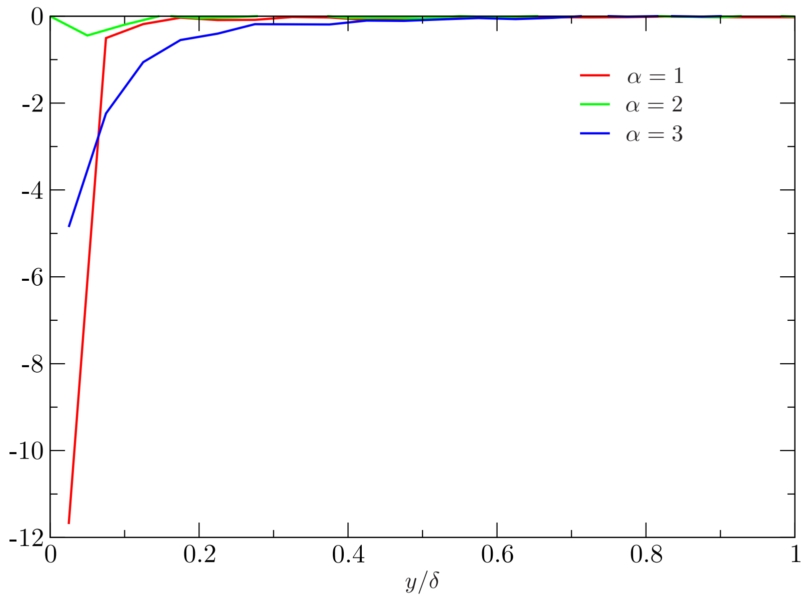

Figure 4.23: Convective term in component energy equations $\left\langle \tilde{u}'_\alpha \tilde{\partial}_1 \overline{u'_\alpha U_1} \right\rangle$, for channel flow at $Re_\tau = 934$.

To see why this is so, consider the convective term expressed in terms of the filtered turbulent velocities

$$\begin{aligned} -\tilde{u}'_\alpha \tilde{\partial}_1 \overline{u'_\alpha U_1} &= -\int_v u'_\alpha(\boldsymbol{\xi}) d\boldsymbol{\xi} \int_v \partial_{x_1}(u'_\alpha(\mathbf{x}) U_1(\mathbf{x})) d\mathbf{x} \\ &= -\int_v \int_v u'_\alpha(\boldsymbol{\xi}) \partial_{x_1}(u'_\alpha(\mathbf{x}) U_1(\mathbf{x})) d\mathbf{x} d\boldsymbol{\xi} \end{aligned} \tag{4.68}$$

where $\partial_{x_1}(u'_\alpha(\mathbf{x})U_1(\mathbf{x})) = U_1(\mathbf{x})\partial_{x_1} u'_\alpha(\mathbf{x}) + u'_\alpha(\mathbf{x}) \cancelto{0}{\partial_{x_1} U_1(\mathbf{x})}$ yields

$$-\left\langle \tilde{u}'_\alpha \tilde{\partial}_1 \overline{u'_\alpha U_1} \right\rangle = -\int_v \int_v U_1(\mathbf{x}) \partial_{x_1} \underbrace{\langle u'_\alpha(\boldsymbol{\xi}) u'_\alpha(\mathbf{x}) \rangle}_{\mathbb{R}_{\alpha\alpha}(\boldsymbol{\xi},\mathbf{x})} d\mathbf{x} d\boldsymbol{\xi} \tag{4.69}$$

where we brought $u'_\alpha(\boldsymbol{\xi})$ inside the partial derivative ∂_{x_1}, because $\boldsymbol{\xi}$ and x are independent, and $\mathbb{R}_{\alpha\alpha}(\boldsymbol{\xi}, \mathbf{x})$ is the two-point correlation.

Define $F_{\alpha\alpha}(\xi_2, x_2)$

$$F_{\alpha\alpha}(\xi_2, x_2) \equiv \int_0^{\Delta_1} \mathbb{R}_{\alpha\alpha}(r_1, \xi_2, x_2) dr_1 - \int_{-\Delta_1}^{0} \mathbb{R}_{\alpha\alpha}(r_1, \xi_2, x_2) dr_1 \tag{4.70}$$

where $\mathbb{R}_{\alpha\alpha}$ is now written as a function of streamwise separation $r_1 \equiv \xi_1 - x_1$ and wall normal locations ξ_2 and x_2, and Δ_1 is the filter width in the streamwise direction. Note that F is antisymmetric $F(\xi_2, x_2) = -F(x_2, \xi_2)$.

Figure (4.24) shows $\mathbb{R}_{33}$ as a function of separations $r_1 \equiv \xi_1 - x_1$ and $r_2 \equiv \xi_2 - x_2$ as found by Bhattacharya, etal [10]. Notice that the correlation falls off most rapidly from a maximum at $r_1 = r_2 = 0$ along a direction inclined from the horizontal. The inclination is due to coherent structures in the flow being tilted by the mean shear. Therefore, $F_{\alpha\alpha}(\xi_2, x_2)$ in equation (4.70) has the same sign as $r_2 \equiv \xi_2 - x_2$.

Having defined $F_{\alpha\alpha}$, we can write the filtered convective term

$$-\left\langle \tilde{u}'_\alpha \tilde{\partial}_1 \overline{u'_\alpha U_1} \right\rangle = \int_0^{\Delta_2} \int_0^{\Delta_2} U_1(x_2) F_{\alpha\alpha}(\xi_2, x_2) dx_2 d\xi_2 \tag{4.71}$$

where Δ_2 is the filter width in the wall-normal direction. The square domain of integration $[0, \Delta_2] \times [0, \Delta_2]$ is divided into two as shown in figure 4.25. The regions of positive and negative F being separated by the line of antisymmetry $\xi_2 = x_2$. Also shown is the direction of increasing U. Because the larger U corresponds to the region of negative F, the resulting correlation is negative. In summary, the mean shear and resulting inclination of coherent structures cause the convection term to be dissipative in the filtered component energy equations.

The simplest model ($L20$) was found to work well for dissipating energy in the viscous terms. Therefore, it is reasonable that it will also work well here for the

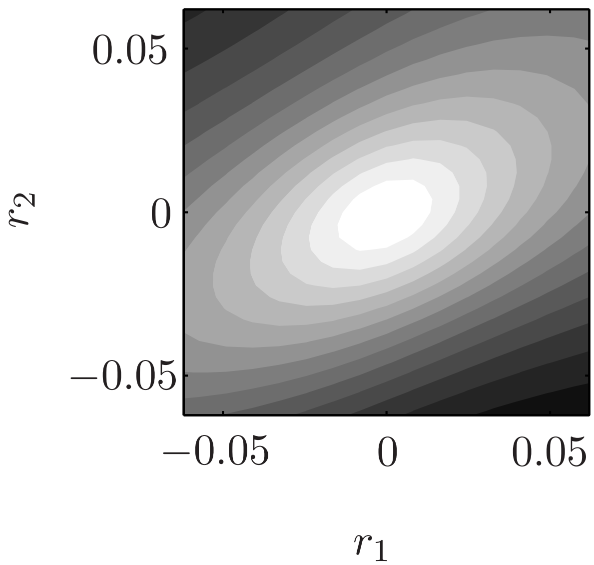

Figure 4.24: Two point correlation $\mathbb{R}_{33}(r_1, r_2)$ at $y^+ = 114$ from DNS of channel flow at $Re_\tau = 940$.

convective term

$$\overline{u'_\alpha U_\beta}^{mod}_{L20} = \mathcal{L}^{-\beta}_{\alpha\beta\alpha}\tilde{u}'^{-\beta}_\alpha + \mathcal{L}^{+\beta}_{\alpha\beta\alpha}\tilde{u}'^{+\beta}_\alpha + \overline{u'_\alpha U_\beta}^{mod}_{std} \tag{4.72}$$

Since the standard nonlinear model conserves energy, it cannot dissipate energy. Therefore dissipation is accomplished entirely by the linear terms. With optimal coefficients $\mathcal{L}$, the model matches the actual fluctuating-mean term in the component energy equations *a priori* (as proven in Appendix D) and closely approximates the corresponding pressure term *a priori* as will be shown in the following section. Recall that for the mean-fluctuating nonlinear model, we subsumed the linear terms into a general quadratic term. However, this was not done for the convective terms, and as long as the mean velocity does not deviate significant from the initial DNS profile,

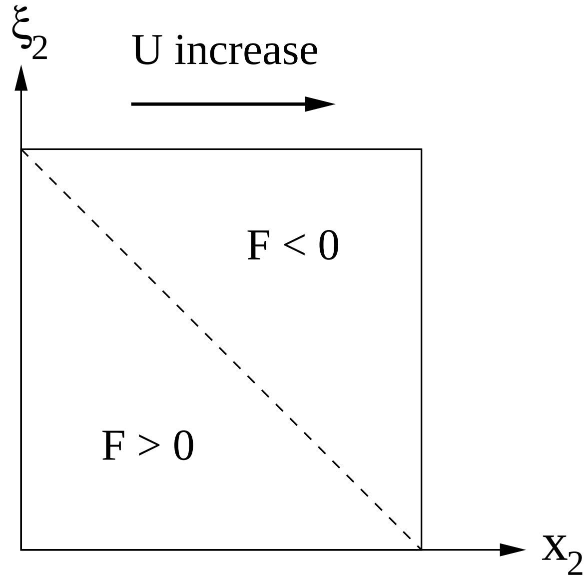

Figure 4.25: Domain of integration for equation (4.71). The dashed line of antisymmetry $\xi_2 = x_2$ separates the regions of positive and negative F. Also shown is the direction of increasing U.

this linear model should be sufficient. As an area for future work, we recommend that these linear models be recast into quadratics, including dependence on local mean velocity gradients.

4.3.4.6 Pressure Term for Nonlinear Mean-Fluctuating and Fluctuating-Mean Models

As stated in section 4.3.3.5, the viscous models have little effect on the pressure model, but the nonlinear models do effect the pressure model, and therefore we have to compare the pressure model for the nonlinear model $D_{ik}(\tilde{\partial}_j \overline{u'_k U_j}^{opt}_{L20})$ with the pressure model for the actual nonlinear term $D_{ik}(\tilde{\partial}_j \overline{u'_k U_j})$. The operator D_{ik} returns the divergent part of its argument and is defined in section 4.3.2, equation

(4.27). Actually, we will examine $D_{ik}(\tilde{\partial}_j(\overline{U_k u'_j} + \overline{u'_k U_j}))$. $\overline{U_i u'_j}$ (production) and $\overline{u'_i U_j}$ (convection) play very different roles in the component energy equations, but their associated pressure terms are approximately the same. To understand why, consider the continuous pressure Poisson equation

$$\partial_k \partial_k p = -\partial_i \partial_j u_i u_j \tag{4.73}$$

Clearly the contribution to the right hand side by the mean-fluctuating term $(-\partial_i \partial_j U_i u'_j)$ and the fluctuating-mean term $(-\partial_i \partial_j u'_i U_j)$ are identical. What is exactly true in the continuous equations is approximately true in the filtered equations. Therefore we will examine the mean-fluctuating and fluctuating-mean pressure models together.

Figure (4.26) shows the pressure models resulting from the actual mean-fluctuating and fluctuating-mean nonlinear terms and their models. This is sometimes called the rapid pressure. Notice that the standard model already produces a reasonable approximation to the actual pressure. "$Q\gamma + L20$" is the combination of models previously described for the mean-fluctuating 4.3.4.4 and fluctuating-mean 4.3.4.5 terms. The "simple $L22$" model refers to applying the simple $L22$ stencil to the mean-fluctuating and fluctuating-mean terms and optimizing. This actually produces the worst results, with a particularly large energy sink in the $\tilde{v}'\tilde{v}'$ equation. The "$Q\gamma + L20$" model produces the best results. Though it is not perfect, it is closest to the actual pressure.

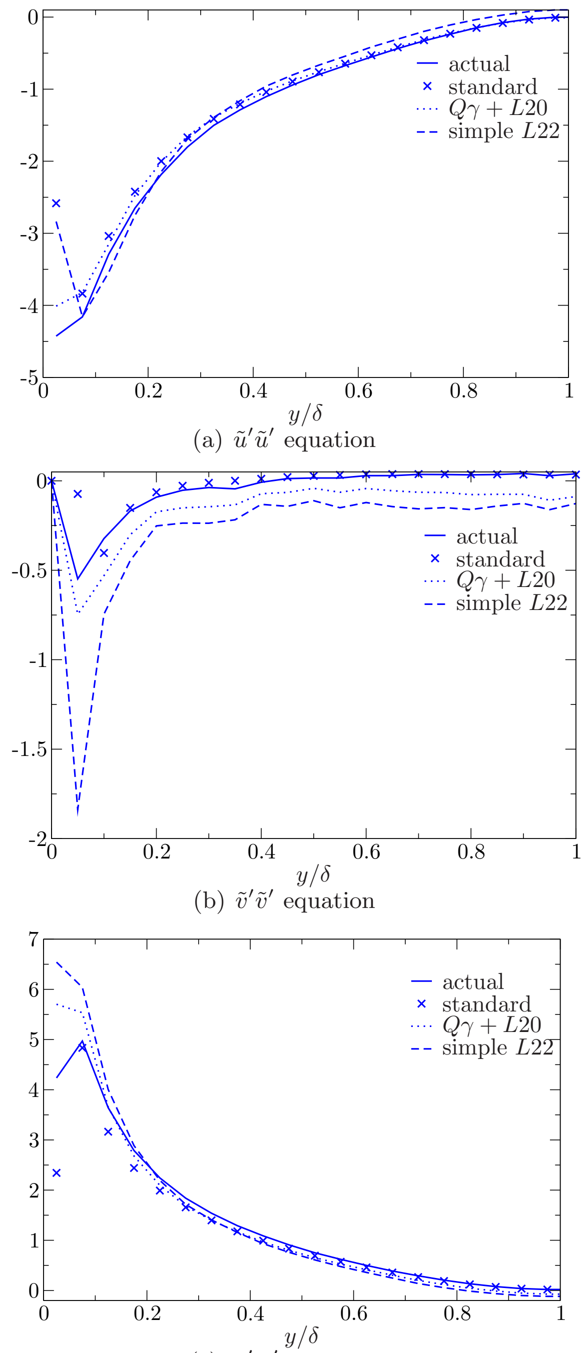

(a) $\tilde{u}'\tilde{u}'$ equation

(b) $\tilde{v}'\tilde{v}'$ equation

(c) $\tilde{w}'\tilde{w}'$ equation

Figure 4.26: Mean-fluctuating plus fluctuating-mean pressure model in the component energy equations for actual nonlinear term and it's models evaluated *a priori*, for channel flow at $Re_\tau = 934$.

4.3.4.7 Nonlinear Fluctuating-Fluctuating Model and Associated Pressure Term

The fluctuating-fluctuating term is responsible for subgrid dissipation and transport. The analogous term in the continuous equations transports but does not dissipate energy; it simply transfers energy down to the small scales to then be dissipated viscously. However, in these filtered equations, with filter widths much larger than the Kolmogorov scales, the fluctuating-fluctuating term must model dissipation.

As described in section 4.3.3.3, the fluctuating-fluctuating term in the component energy equations can be decomposed

$$\tilde{u}'_\alpha \tilde{\partial}_\beta \overline{u'_\alpha u'_\beta} = \tilde{\partial}_\beta(\overline{u'_\alpha u'_\beta}\underline{\tilde{u}'_\alpha}_\beta) - \underline{\overline{u'_\alpha u'_\beta}\tilde{\partial}_\beta \tilde{u}'_\alpha}_\beta \tag{4.74}$$

where the terms on the right are identified as transport and dissipation respectively. Figure (4.27) shows turbulent transport and subgrid dissipation in the filtered component energy equations. For channel flow, where x and z are directions of homogeneity, only the components $\overline{u'_\alpha v'}$ transport energy on average. However, all components $\overline{u'_\alpha u'_\beta}$ contribute to dissipation. Notice that there are components of $\overline{u'_\alpha u'_\beta}$ labeled "dissipation" that actually add energy instead of removing it. These components are $(\alpha, \beta) = (1, 2), (2, 3), (3, 1)$. However, the total dissipation (summed over β) removes energy everywhere and for each component α. The transport sums in y to zero as expected.

Figure (4.28) shows the overall nonlinear fluctuating-fluctuating term (transport plus dissipation) and it's standard nonlinear model in the component energy

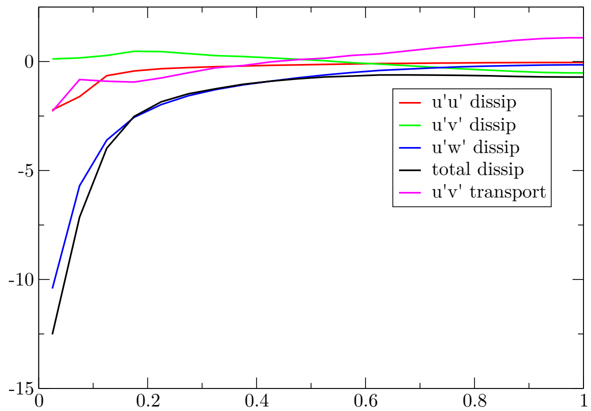

(a) $\tilde{u}'\tilde{u}'$ equation

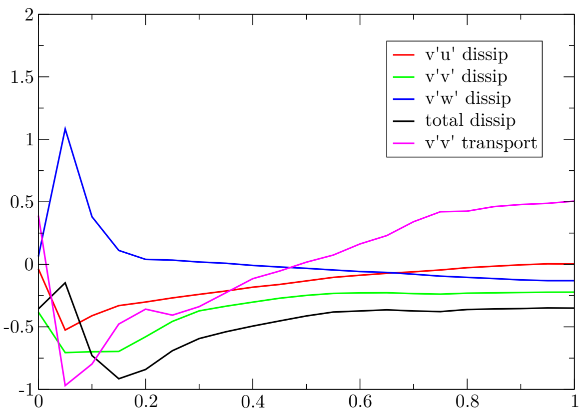

(b) $\tilde{v}'\tilde{v}'$ equation

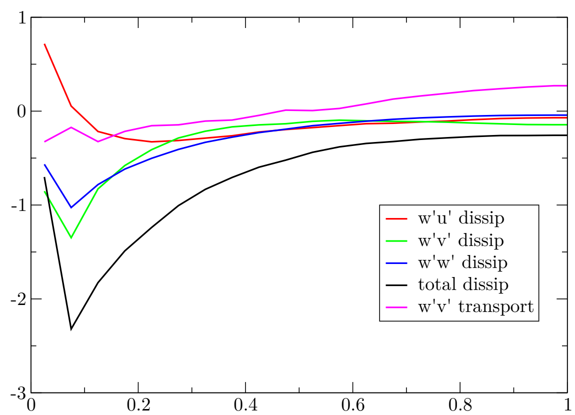

(c) $\tilde{w}'\tilde{w}'$ equation

Figure 4.27: Decomposition of $\left\langle \tilde{u}'_\alpha \tilde{\partial}_\beta \overline{u'_\alpha u'_\beta} \right\rangle$ into transport and subgrid dissipation, for channel flow at $Re_\tau = 934$.

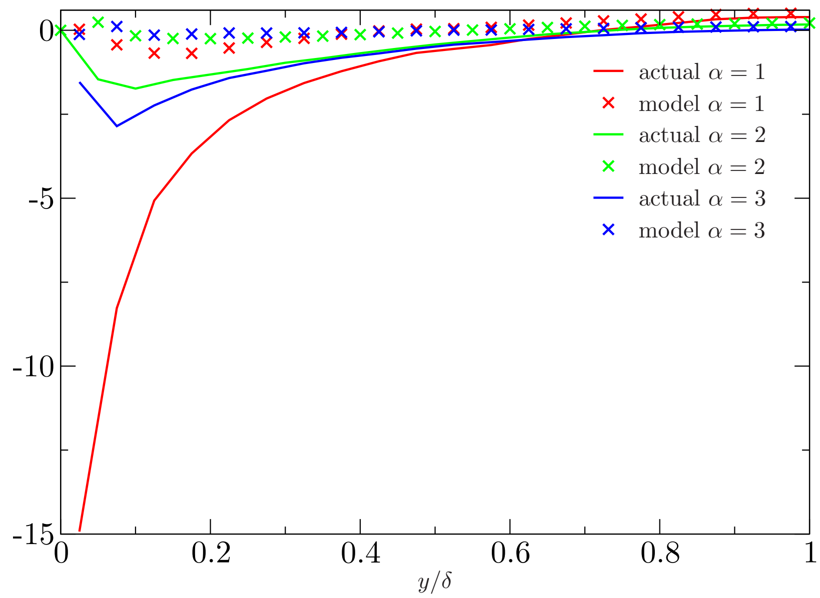

Figure 4.28: Fluctuating-fluctuating nonlinear terms in the $\langle \tilde{u}'_\alpha \tilde{u}'_\alpha \rangle$ component energy equations and standard nonlinear models evaluated *a priori*, for channel flow at $Re_\tau = 934$.

equations. The standard nonlinear model in each of the component energy equations sum in y to zero. This is due to the energy conservation property of the standard nonlinear model, which is proven in Appendix E. Therefore, by itself, the standard nonlinear model has the potential to model transport but not dissipation.

In an effort to improve the fluctuating-fluctuating model, all the models described in section 4.3.3.2, ($L20$, $L22$, LRS, $Q22$) were tested. Out of all the models tested, the optimal quadratic $Q22$ was the best overall. The optimized $Q22$ model had the smallest RMS differences from the actual flux. We also compared *a priori* the nonlinear and associated pressure terms in the filtered component energy equations. It is important to point out that all of these models, when optimized, will match *a priori* the nonlinear term, as explained in section 4.3.3.2. In fact, the dissipation and transport are individually matched *a priori*, as explained in section 4.3.3.3. However, under the current optimization for the nonlinear flux model, the resulting pressure model is not guaranteed to match *a priori*, although increasing the number of dependencies generally decreases the error in the pressure model. Figure (4.29) shows the pressure terms in the component energy equations using the different models. Notice that the Reynolds stress model is the only model that performs consistently better than the standard model *a priori*. Surprisingly, the other two models, $L22$ and $Q22$, actually perform worse than the standard model in the $\tilde{u}'\tilde{u}'$ and $\tilde{w}'\tilde{w}'$ equations. It makes sense that the model with the largest stencil (LRS) was found to best match the pressure term *a priori*, but this model also contained unstable components which caused the LES to blow up. Finally, we compared LES results, velocity mean and variances, with filtered DNS. Q22 was found to perform the best in the LES.

4.3.4.8 Nonlinear Models Constructed to Match Pressure Terms

For the nonlinear fluctuating-fluctuating models described in the previous section 4.3.4.7, increasing the stencil size and optimizing the quadratic coefficients improved the *a priori* behavior of the pressure term in the component energy equations, but we were not able to exactly match the pressure term, as shown in figure (4.29). In this section, we describe how to construct models to match the pressure term *a priori*.

Section 4.3.3.2 explains how local optimal models match the nonlinear terms

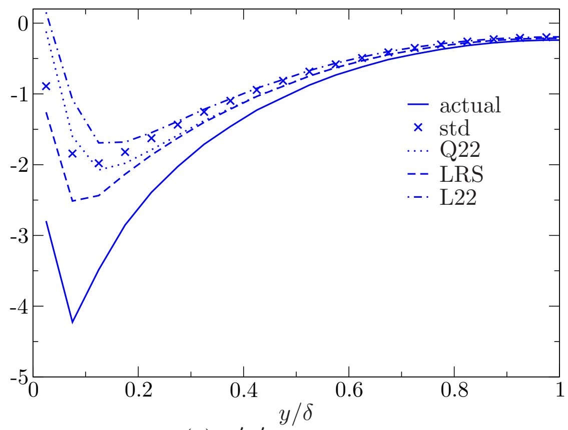

(a) $\tilde{u}'\tilde{u}'$ equation

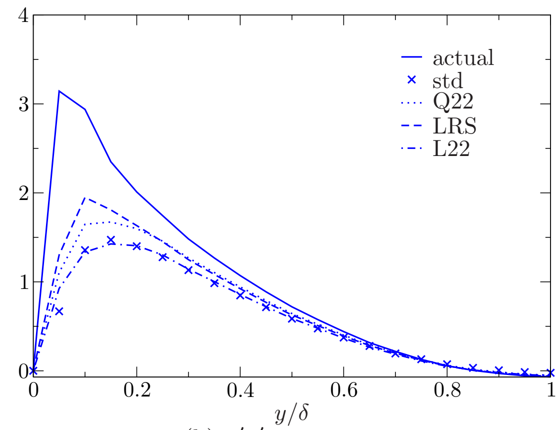

(b) $\tilde{v}'\tilde{v}'$ equation

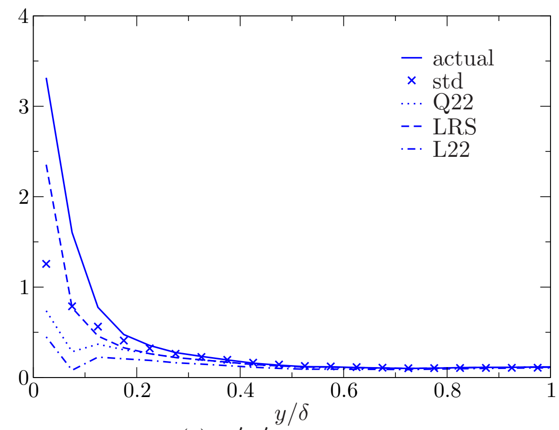

(c) $\tilde{w}'\tilde{w}'$ equation

Figure 4.29: Pressure model associated with the fluctuating-fluctuating term and it models evaluated *a priori* in the component energy equations, for channel flow at $Re_\tau = 934$.

in the component energy equations

$$\left\langle \tilde{u}'_\alpha \tilde{\partial}_\beta \overline{u_\alpha u_\beta} \right\rangle = \left\langle \tilde{u}'_\alpha \tilde{\partial}_\beta \overline{u_\alpha u_\beta}^{mod} \right\rangle \tag{4.75}$$

Local models can also be constructed to match the divergent part of the nonlinear terms, which are a good approximation to the pressure term, in the component energy equations

$$\left\langle \tilde{u}'_\gamma D_{\gamma\alpha} (\tilde{\partial}_\beta \overline{u_\alpha u_\beta}) \right\rangle = \left\langle \tilde{u}'_\gamma D_{\gamma\alpha} (\tilde{\partial}_\beta \overline{u_\alpha u_\beta}^{mod}) \right\rangle \tag{4.76}$$

where

$$D_{\gamma\alpha} = \tilde{\partial}_\gamma (\tilde{\partial}_j \tilde{\partial}_j)^{-1} \tilde{\partial}_\alpha \tag{4.77}$$

returns the divergent part of vector argument and involves the solution of a Poisson equation with specific boundary conditions described in section 4.3.2.

It is important to match both equations (4.75-4.76), because they represent different phenomena. The fluctuating-fluctuating nonlinear term itself is responsible for turbulent transport and dissipation, while it's divergent part is responsible for intercomponent energy transfer. It should be noted that a model that satisfies equation (4.76) in addition to equation (4.75) is no longer optimal. In a sense, we are trading out optimality in exchange for matching the pressure term. Furthermore, equation (4.75) is a local constraint, so models satisfying it can be constructed one y location at a time. On the other hand, $D_{\gamma\alpha}$ is an operator global in y, so equation (4.76) applies global constraints, and models satisfying it must be constructed simultaneously over all N_y locations.

There are many ways to satisfy both equations. We chose to satisfy equation (4.75) summed over β ($3 \cdot N_y$ constraints) and equation (4.76) summed over α and β

(another $3 \cdot N_y$ constraints), because these are the minimal constraints necessary to ensure that the *combined* effect of the models $\overline{u_\alpha u_\beta}^{mod}$ match that of the actual terms $\overline{u_\alpha u_\beta}$ and their associated pressure in the component energy equations. Models were constructed for the two simple linear stencils $L20$ and $L22$, with $18 \cdot N_y$ and $30 \cdot N_y$ coefficients respectively. Since there are more coefficients than constraints, we added the optimality conditions described in section 4.3.3.1, for which we minimize squared error.

Let A_1 and b_1 represent the standard optimal conditions, to be satisfied in a least squares sense, and let A_2 and b_2 represent the nonlinear and pressure constraints (described in the previous paragraph), to be satisfied exactly. For stencil $L20$ with $N_y = 40$, A_1 is 710×710, b_1 is 710×1, A_2 is 238×710, b_2 is 238×1. We use a Lagrange multiplier method to solve for the coefficients:

$$L = (A_1 x - b_1)^T (A_1 x - b_1) + \lambda (A_2 x - b_2) \tag{4.78}$$

where x is the vector of coefficients, and λ is the Lagrange multiplier vector. For stencil $L20$ with $N_y = 40$, x is 710×1, and λ is 238×1. Setting to zero the derivatives with respect to x and λ:

$$\frac{\partial L}{\partial x^T} = 2(A_1^T A_1 x - A_1^T b_1) + A_2^T \lambda = 0 \tag{4.79}$$

$$\frac{\partial L}{\partial \lambda^T} = A_2 x - b_2 = 0 \tag{4.80}$$

And the overall matrix equation becomes:

$$\begin{bmatrix} 2A_1^T A_1 & A_2^T \\ A_2 & 0 \end{bmatrix} \begin{bmatrix} x \\ \lambda \end{bmatrix} = \begin{bmatrix} 2A_1^T b_1 \\ b_2 \end{bmatrix} \tag{4.81}$$

By using these models we were able to match *a priori* the actual nonlinear and pressure terms shown in figures (4.28) and (4.29). Unfortunately, the resulting models were also unstable when used in the LES. To date, the above pressure constrained methodology has not produced successful (stable) models. We have yet to test larger stencils, such as $Q22$ and LRS. Another area for future work is to add stability constraints to this problem and to analyze the stability problems encountered by the LRS models in section 4.3.4.7.

4.3.5 LES Results

In this section, the *a posteriori* LES results using the models described in section 4.3 are presented. Out of the roughly hundred model combinations tested, only four will be presented here. They are:

(S1) Standard Second-Order Finite-Volume Models

(S2) $L22$ Optimal Nonlinear Models + $L20$ Optimal Viscous Models

(S3) $Q\gamma$ Mean-Fluctuating Models + $L20$ Optimal Fluctuating-Mean Models + $L22$ Optimal Fluctuating-Fluctuating Models + $L20$ Optimal Viscous Models

(S4) $Q\gamma$ Mean-Fluctuating Models + $L20$ Optimal Fluctuating-Mean Models + $Q22$ Optimal Fluctuating-Fluctuating Models + $L20$ Optimal Viscous Models

The first set (S1) uses standard second-order finite-volume approximations for the nonlinear and viscous terms, as described in section 4.3.2. The second set (S2) uses the basic optimal modeling approach described in section 4.3.3.1, with stencil $L22$ described in section 4.3.3.2, to model the nonlinear term, without Reynolds decomposition. The third set (S3) employs Reynolds decomposition on the nonlinear term, treating the mean-fluctuating as described in section 4.3.4.4, fluctuating-mean as described in section 4.3.4.5, and fluctuating-fluctuating with the $L22$ model as described in section 4.3.4.7. The most significant change from S2 to S3 is the modeling of the mean-fluctuating term which is responsible for production. The fourth set (S4) again employs Reynolds decomposition as with S3, but uses a better model ($Q22$) for the fluctuating-fluctuating term as described in section 4.3.4.7. The same viscous models, described in sections 4.3.4.1 and 4.3.4.2, are used for sets S2, S3, and S4. All 4 sets use the standard pressure model described in section 4.3.2.

4.3.5.1 (S1) Standard Second-Order Finite-Volume Models

Using the standard models for nonlinear, viscous, and pressure terms, an *a priori* comparison of terms from the mean momentum equation and the component energy equations are shown in figure (4.30). An *a posteriori* comparison of LES velocities profiles are shown in figure (4.31). Notice from figure (4.31) that the mean velocity is too high near the wall and too low near the center of the channel indicating that the wall shear stress is over-predicted. This is because the total term from the right hand side of the momentum equation is too high near the wall, as shown in figure (4.30). Figure (4.31) also shows that the velocity variances are too high near the wall and too low near the center of the channel. This near-wall behavior is directly related to the fact that the total term from the right hand side of the component energy equations is too high near the wall, as shown in figure (4.30).

Examining figure (4.30a) reveals that the standard nonlinear model $\tilde{\partial}_y \overline{u'v'}^{mod}_{std}$ badly represents the actual term $\tilde{\partial}_y \overline{u'v'}$, especially near the wall. Likewise, the standard viscous model $\tilde{\partial}_y \overline{\partial_y U}^{mod}_{std}$ badly represents the actual term $\tilde{\partial}_y \overline{\partial_y U}$, especially near the wall. This is because as one approaches the wall, gradients of $\overline{u'v'}$ and $\overline{U}$ increase, making the volume-filtered quantities $\tilde{u}'$, $\tilde{v}'$, and $\tilde{U}$ which are used in the standard models relatively more coarse and less capable of representing the derivatives of $\overline{u'v'}$ and $\overline{U}$. For similar reasons, the standard models become worse representations of terms in the component energy equations as one approaches the wall. See figures (4.30b-d). This is the basic problem in near-wall LES: the filtered-scales do not represent the dominant dynamics near the wall.

4.3.5.2 (S2) $L22$ Optimal Nonlinear Models + $L20$ Optimal Viscous Models

Using optimal $L22$ models for the nonlinear terms and optimal $L20$ models for the viscous terms guarantees that the *a priori* nonlinear and viscous terms in the mean momentum and component energy equations are exactly represented. See Figure (4.32). In the resulting LES, the mean velocity profile closely matches the filtered DNS, and several of the velocity variance profiles are also closer than for the S1 model. However $\langle \tilde{u}'\tilde{u}' \rangle$ is far too high near the wall and exhibits an anomolous bump near the channel center.

The component energy equation terms are shown in figure (4.32). The simple optimal models match *a priori* the profiles for the nonlinear and viscous terms. However the pressure terms do not match. The pressure model is not transfering enough energy from $\langle \tilde{u}'\tilde{u}' \rangle$ to $\langle \tilde{v}'\tilde{v}' \rangle$, but the rate of transfer to $\langle \tilde{w}'\tilde{w}' \rangle$ is correct. This

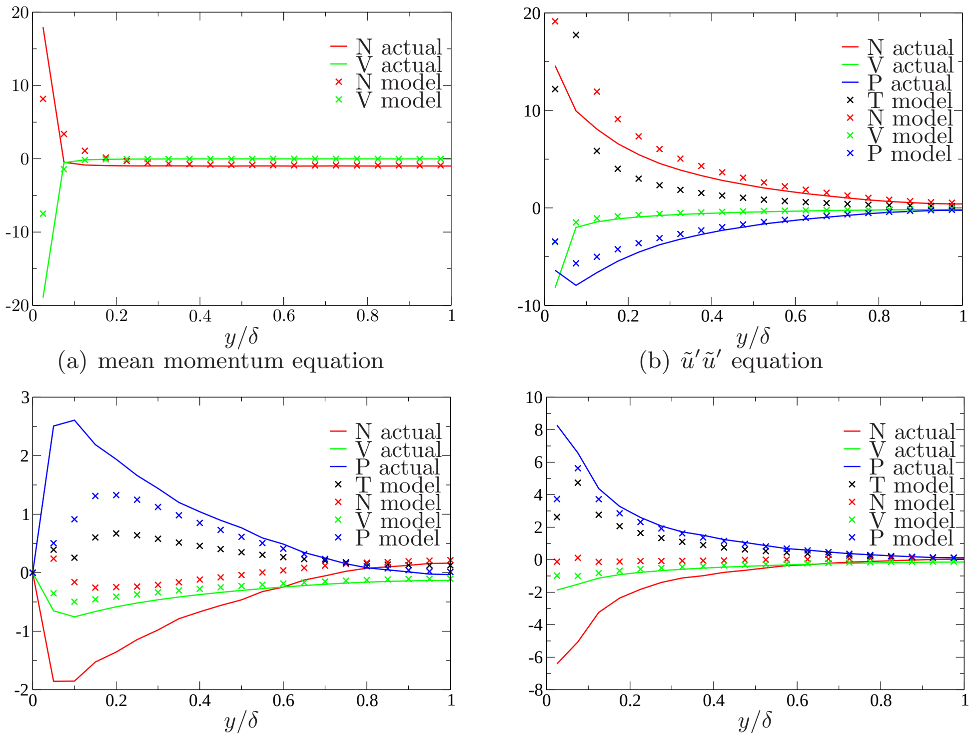

(a) mean momentum equation (b) $\tilde{u}'\tilde{u}'$ equation

(c) $\tilde{v}'\tilde{v}'$ equation (d) $\tilde{w}'\tilde{w}'$ equation

Figure 4.30: Nonlinear (N), Viscous (V), Pressure (P), and Total (T) terms, actual and (S1) standard models *a priori* in the mean momentum and component energy equations for channel flow at $Re_\tau = 934$.

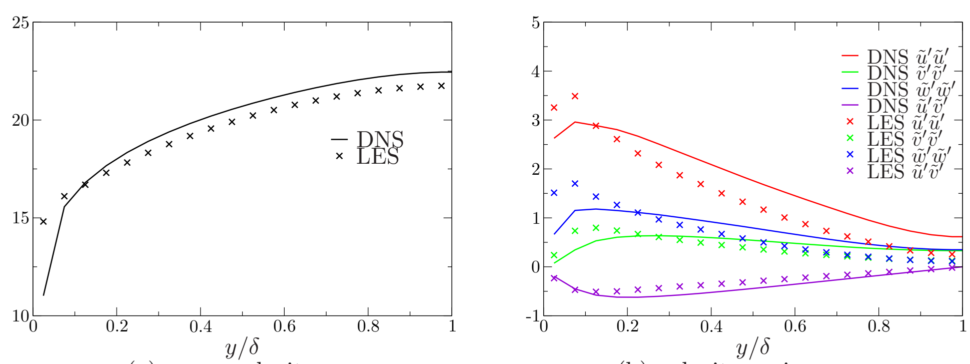

(a) mean velocity (b) velocity variances

Figure 4.31: Velocity profiles for filtered DNS and LES with (S1) standard models for channel flow at $Re_\tau = 934$.

problem with pressure may be the cause of the high near-wall $\langle \tilde{u}'\tilde{u}' \rangle$ and slightly low near-wall $\langle \tilde{v}'\tilde{v}' \rangle$. Streamwise variance $\langle \tilde{u}'\tilde{u}' \rangle$ may also be high as a result of stability problems the $\overline{uw}$ model

$$\overline{uw}^{opt}_{L22} = \mathcal{A}_{opt} + \underbrace{\mathcal{L}^{-z}_{opt}\tilde{u}^{-z} + \mathcal{L}^{+z}_{opt}\tilde{u}^{+z}}_{L_u} + \underbrace{\mathcal{L}^{-x}_{opt}\tilde{w}^{-x} + \mathcal{L}^{+x}_{opt}\tilde{w}^{+x}}_{L_w} + \overline{uw}^{mod}_{std} \tag{4.82}$$

where $\tilde{u}^{-z}$ and $\tilde{u}^{+z}$ are cells on the plus and minus z side of face $\overline{uw}$, and $\tilde{w}^{-x}$ and $\tilde{w}^{+x}$ are cells on the plus and minus x side of face $\overline{uw}$. L_u denotes the part of the model linearly dependent on $\tilde{u}$, and L_w denotes the part the model linearly dependent on $\tilde{w}$. As shown in figure (4.34), the L_u term evaluated *a priori* in the streamwise component energy equation has a positive energy transfer rate. This implies negative diffusivity which can lead to model instability. See section 4.3.3.4 for more details.

4.3.5.3 (S3) Reynolds Decomposed Nonlinear Models

The main difference between S2 and S3 is the mean-fluctuating model. (The fluctuating-mean models also differ but only slightly.) S2 used a simple optimal model $\overline{Uu'_j}^{opt}_{L22}$, while S3 uses the $Q\gamma$ model described in section 4.3.4.4. Figure (4.36) shows the resulting velocity mean and variance profiles for the Reynolds decomposed nonlinear models. As with S2, the mean velocity is again predicted very well, except that the point closest to the wall is a bit low. The velocity variances are also well-predicted, except near the wall where $\langle \tilde{u}'\tilde{u}' \rangle$ is high and $\langle \tilde{v}'\tilde{v}' \rangle$ is a bit low. The behavior here for $\langle \tilde{u}'\tilde{u}' \rangle$ is better than S2, in that there is not nearly as much overshoot near the wall and that there is no longer the anomalous bump.

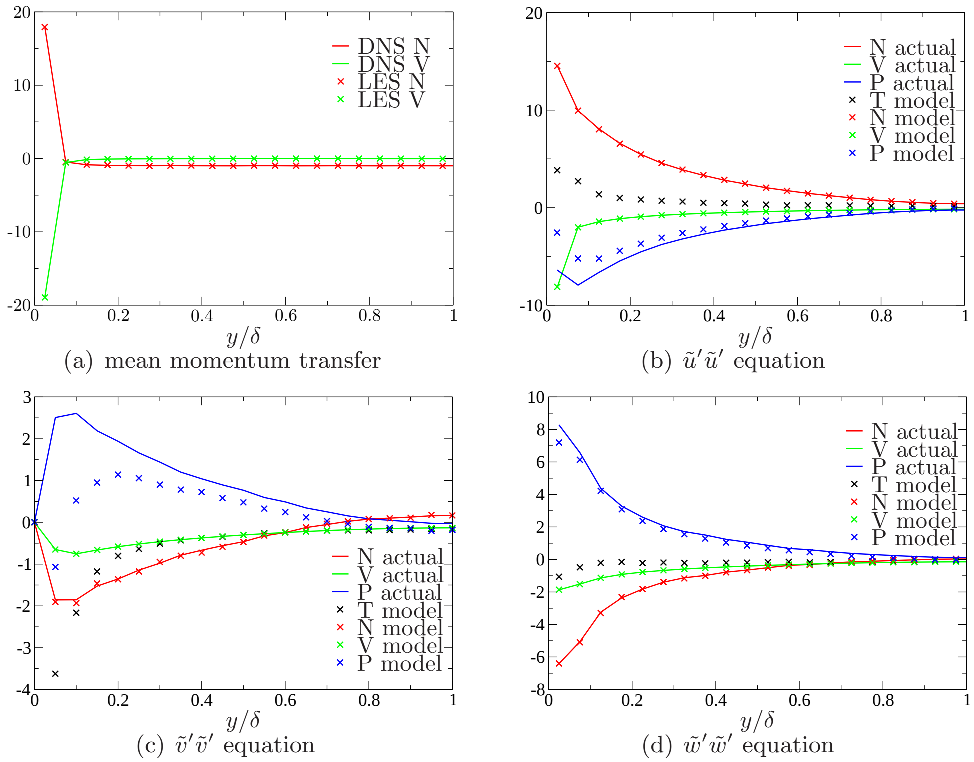

(a) mean momentum transfer (b) $\tilde{u}'\tilde{u}'$ equation

(c) $\tilde{v}'\tilde{v}'$ equation (d) $\tilde{w}'\tilde{w}'$ equation

Figure 4.32: Nonlinear (N), Viscous (V), Pressure (P), and Total (T) terms, actual and (S2) models *a priori* in the mean momentum and component energy equations for channel flow at $Re_\tau = 934$.

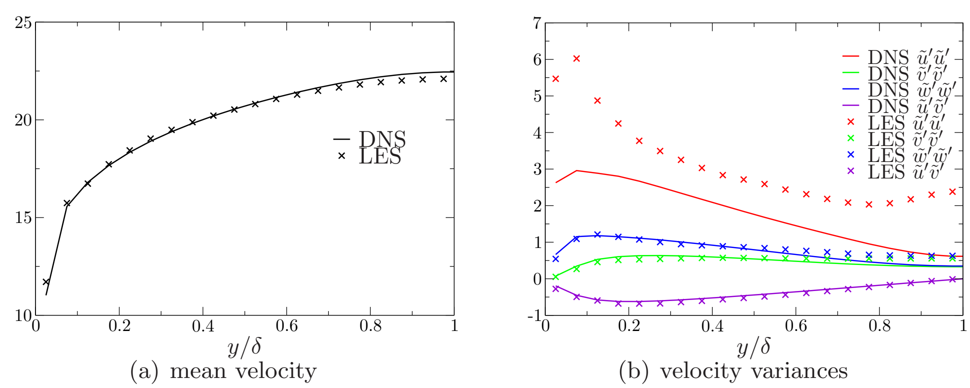

(a) mean velocity (b) velocity variances

Figure 4.33: Velocity profiles for filtered DNS and LES with (S2) models for channel flow at $Re_\tau = 934$.

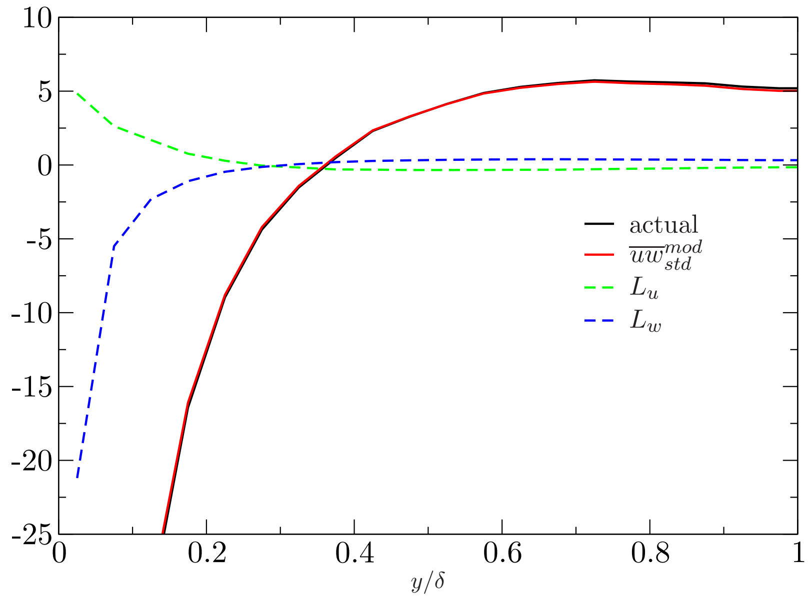

Figure 4.34: $\overline{uw}$ and it's optimal $L22$ model components evaluated *a priori* in the streamwise energy equation, for channel flow at $Re_\tau = 934$.

Figure (4.35) shows the terms from the component energy equations. The main discrepancies are still with the pressure terms. Not enough energy leaves $\langle \tilde{u}'\tilde{u}' \rangle$ and not enough energy enters $\langle \tilde{v}'\tilde{v}' \rangle$, though this is less severe than with S2.

4.3.5.4 (S4) Reynolds Decomposed Nonlinear Models, with Optimal Quadratic Fluctuating-Fluctuating Models

From S3 to S4, we swapped out the fluctuating-fluctuating $L22$ model for the slightly better $Q22$ model. This is our best set of models to date. Figure (4.38) shows the velocity mean and variance profiles. As before the mean velocities are very good, except a bit low near the wall. The variance profiles in this case are also very good. $\langle \tilde{u}'\tilde{u}' \rangle$ is a bit high and $\langle \tilde{v}'\tilde{v}' \rangle$ is a bit low, a symptom attributable again to the pressure modeling problems. Figure (4.37) shows actual and model terms in

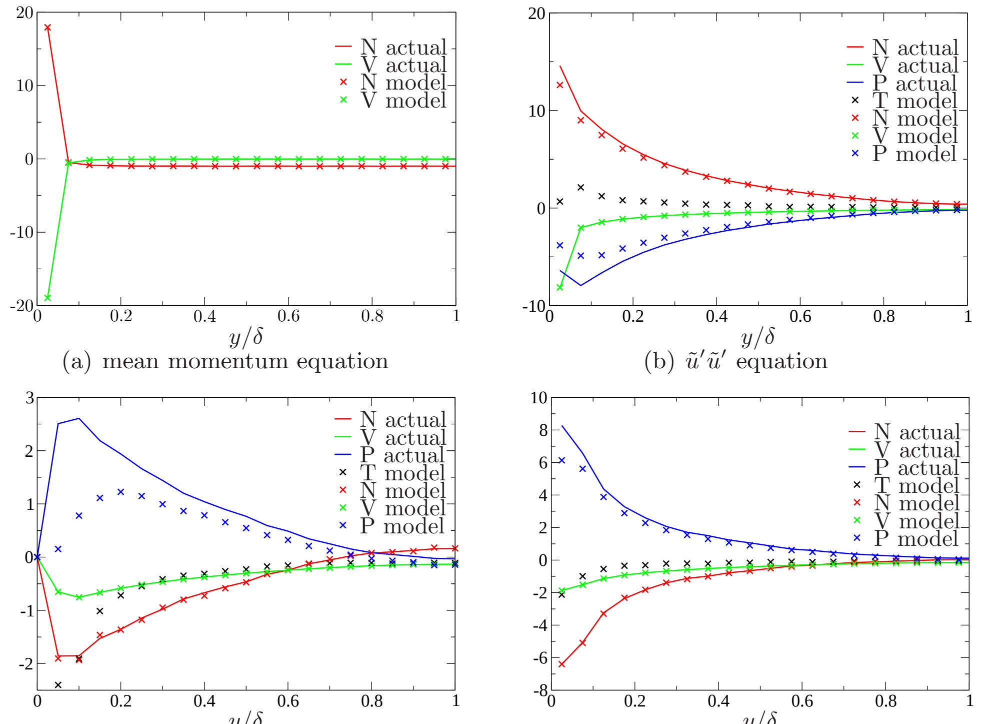

(a) mean momentum equation

(b) $\tilde{u}'\tilde{u}'$ equation

(c) $\tilde{v}'\tilde{v}'$ equation

(d) $\tilde{w}'\tilde{w}'$ equation

Figure 4.35: Nonlinear (N), Viscous (V), Pressure (P), and Total (T) terms, actual and (S3) models *a priori* in the mean momentum and component energy equations for channel flow at $Re_\tau = 934$.

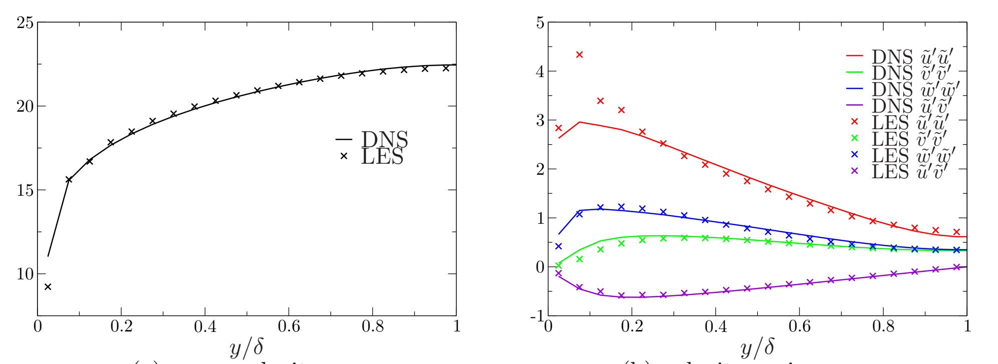

(a) mean velocity

(b) velocity variances

Figure 4.36: Velocity profiles for filtered DNS and LES with (S3) models for channel flow at $Re_\tau = 934$.

the component energy equations.

4.3.5.5 Summary

Table (4.1) shows a summary of the models and results. The first seven columns describe the combination of models. The next five columns are L1 relative errors between LES and filtered DNS of the stated quantities, and the last column is the ratio of LES to DNS mean wall shear stress.

In summary, the $Q\gamma$ model, a standard nonlinear model with adjusted mean term, is a good representation of the mean-fluctuating nonlinear term which is responsible for production and for approximately half of the intercomponent energy transfer via the pressure term (mainly transfer from $\langle \tilde{u}'\tilde{u}' \rangle$ to $\langle \tilde{w}'\tilde{w}' \rangle$, see figure (4.15)). The standard nonlinear model does not model the removal of energy in the fluctuating-mean term $\tilde{\partial}_1 \overline{u_i' U_1}$, so we have accomplished this with a $L20$ optimal model. The standard nonlinear term is not a good model for the fluctuating-fluctuating nonlinear term, nor for the other half of intercomponent energy transfer via the pressure term (mainly transfer from $\langle \tilde{u}'\tilde{u}' \rangle$ to $\langle \tilde{v}'\tilde{v}' \rangle$, see figure (4.15)). We have therefore tested many optimal models for the fluctuating-fluctuating term. Our best model to date produces reasonably good results for the velocity mean and variances, but the pressure errors have not been entirely resolved.

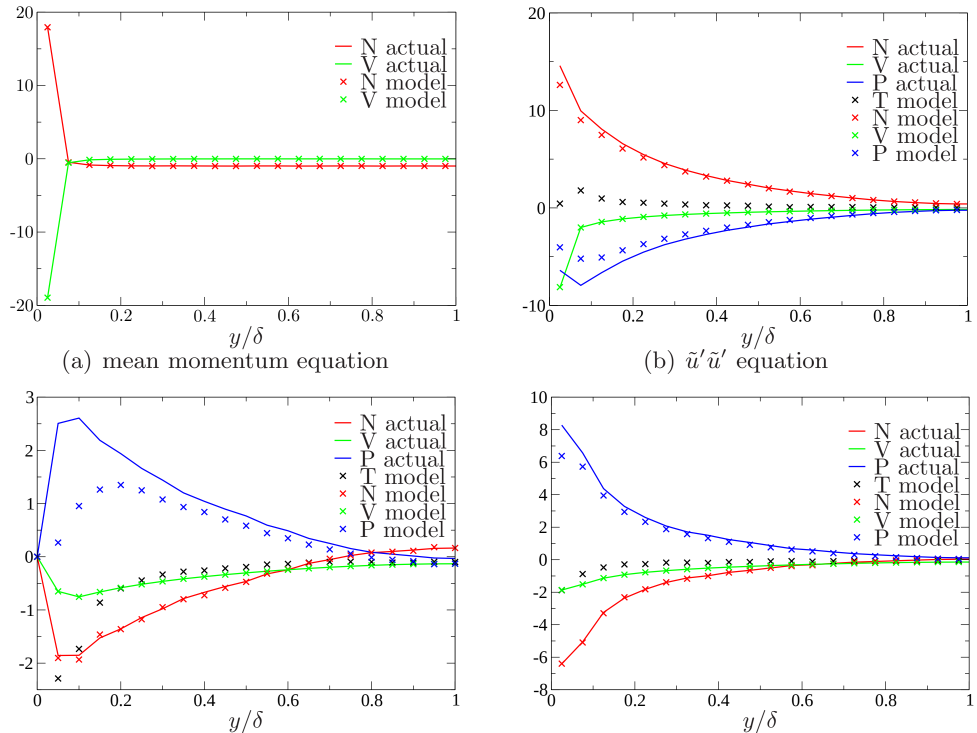

(a) mean momentum equation (b) $\tilde{u}'\tilde{u}'$ equation

(c) $\tilde{v}'\tilde{v}'$ equation (d) $\tilde{w}'\tilde{w}'$ equation

Figure 4.37: Nonlinear (N), Viscous (V), Pressure (P), and Total (T) terms, actual and (S4) models *a priori* in the mean momentum and component energy equations for channel flow at $Re_\tau = 934$.

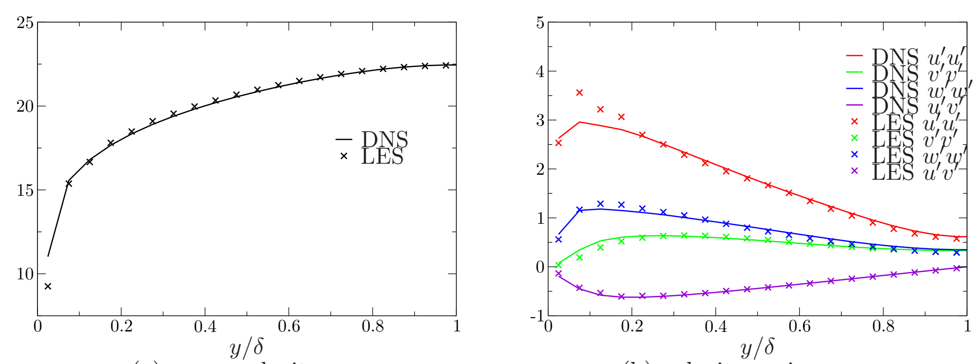

(a) mean velocity (b) velocity variances

Figure 4.38: Velocity profiles for filtered DNS and LES with (S4) models for channel flow at $Re_\tau = 934$.

Set	$\overline{p}$	$\overline{\partial_j U_i}$	$\overline{\partial_j u'_i}$	$\overline{U_i u'_j}$	$\overline{u'_i U_j}$	$\overline{u'_i u'_j}$	$\tilde{U}$	$\langle \tilde{u}' \tilde{u}' \rangle$	$\langle \tilde{v}' \tilde{v}' \rangle$	$\langle \tilde{w}' \tilde{w}' \rangle$	$\langle \tilde{u}' \tilde{v}' \rangle$	$\langle \tau_w \rangle$
S1	std	std	std	std	std	std	0.038	0.244	0.375	0.346	0.270	1.16
S2	std	A	$L20$	$L22$	$L22$	$L22$	0.009	0.727	0.212	0.138	0.110	1.03
S3	std	A	$L20$	$Q\gamma$	$L20$	$L22$	0.010	0.118	0.088	0.057	0.059	0.92
S4	std	A	$L20$	$Q\gamma$	$L20$	$Q22$	0.008	0.068	0.077	0.076	0.049	0.92

Table 4.1: Description of 4 sets of models and their LES results. Columns 2-7 describe the combination of models. These are standard models described in section 4.3.2 and optimal models described in sections 4.3.4.1 through 4.3.4.7. Columns 8-12 are L1 relative errors for the velocity mean and variances. Column 13 is the normalized mean wall shear stress, which should be exactly one.

Chapter 5

Conclusions and Future Work

There were two major areas of work in this dissertation. The first was developing a model for the three-point third-order velocity correlation in isotropic turbulence. The second was modeling subgrid turbulence for unresolved wall-bounded LES.

5.1 Three-point Third-order Velocity Correlation

We developed an explicit mathematical model for the three-point third-order velocity correlation $\mathbb{T}_{ijk}(\mathbf{r}^1, \mathbf{r}^2) = \left\langle u_i'(\mathbf{x})u_j'(\mathbf{x}+\mathbf{r}^1)u_k'(\mathbf{x}+\mathbf{r}^2)\right\rangle$. Proudman and Reid had derived a generating function for the Fourier transform of $\mathbb{T}_{ijk}$ in homogeneous and isotropic turbulence, which we transformed to physical space. Kolmogorov's theory states that if the turbulence is homogeneous, isotropic, and in the inertial range, then the two-point third-order correlation $\mathbb{T}_{ijk}(0, \mathbf{r})$ is linear in r, see equation (3.8). Knowing this limiting case and the generating function, we derived five basis functions for $\mathbb{T}_{ijk}$ for homogeneous, isotropic turbulence, in the inertial range. These basis functions were fit to DNS data for $Re_\lambda = 164$ with coefficient of determination is $R^2 = 0.96$ showing that the basis functions describe the actual data well.

In Optimal LES, spatially filtered $\mathbb{T}_{ijk}$ couples the solution of optimal linear and quadratic coefficients. This is the last correlation on the right hand side of equation (4.32) and the second correlation on the right hand side of equation (4.33). $\mathbb{T}_{ijk}$ may be spatially filtered to determine the filtered two-point third-order correlation $\tilde{\mathbb{S}}_{ijk}$, which describes energy transfer among filtered scales. It can therefore be used in *a priori* analysis of the filtered component energy or Reynolds stress transport equations.

Future work should include fitting the five basis functions for $\mathbb{T}_{ijk}$ to higher Re_λ data and also using $\mathbb{T}_{ijk}$ in future LES modeling and analysis efforts, as indeed has been done in [47].

5.2 Wall-Bounded Turbulence Modeling

We developed improved models for the nonlinear and viscous flux terms in the volume-filtered Navier-Stokes equations, with uniform grid and unresolved wall layers. The statistics used in constructing these models came from DNS of channel flow at $Re_\tau = 934$. The improved models were tested along with the standard pressure model in a staggered-grid finite-volume LES of channel flow at the same Re_τ. Our LES results, velocity mean and variances, were significantly better than most published results for channel flow LES with unresolved wall layers.

The standard pressure model and simple optimal viscous models were found to be sufficient for representing their respective terms. The nonlinear flux terms required more careful treatment. First, it was important to Reynolds-decompose the nonlinear term and to model each part separately, because different parts represent different physical phenomena. Second, it was important to evaluate the effect of each model on the pressure term, because errors in the pressure term were primarily caused by problems with the nonlinear models, specifically their divergent part. The standard pressure model itself was found to be a fairly good representation of the filtered pressure operator.

We constructed accurate models for production and convection, which are associated with the mean-fluctuating and fluctuating-mean nonlinear terms respectively. The convective flux terms were found to be dissipative and were well-represented by simple optimal models. On the other hand, optimal modeling of the mean-fluctuating terms (responsible for production) resulted in linear instabilities and errors in the associated pressure term. An improved model for production was a standard nonlinear model with a multiplicative factor to correct for underresolution of the mean velocity near the wall.

The fluctuating-fluctuating term is responsible for transport, subgrid dissipation, and intercomponent transfer (through the pressure term). For the fluctuating-fluctuating term, we constructed various optimal models, all of which matched the nonlinear terms in the component energy equation *a priori*, but none of which exactly matched the associated pressure terms. As stencil size increased, the pressure terms usually improved but never matched. LES statistics, velocity mean and variances, also improved with stencil size. Our best set of models perform better than other LES with unresolved wall layers [5, 12, 16, 48] but still exhibit slightly high streamwise variance and slightly low wall-normal variance compared to filtered DNS. This is directly related to the mismatch in pressure term for the fluctuating-fluctuating model.

The best optimal fluctuating-fluctuating model in terms of *a priori* pressure statistics was for the largest stencil, the Reynolds stress matching stencil (LRS). However, this model turned out to be unstable in the LES. Because of the size and complexity of this model, we have not yet analyzed it's stability characteristics as we did for the simplest model ($L20$) to determine how it needs to be modified. Therefore, future work should include analyzing stability for the larger stencils. We also constructed fluctuating-fluctuating models to exactly match the pressure statistics *a priori*, but all of these models also turned out unstable in the LES. Therefore, future work should include devising constraints to match pressure statistics in a stable way.

All of our modeling to date has been based on $Re_\tau = 934$ channel flow DNS data and running LES of the same flow. In the future, we should parameterize these models with Re_τ or with other mean flow parameters. These static models should quite easily generalize to other equilibrium wall-bounded flows. For developing flows, dynamic models may be more suitable. However, the following principles for modeling near-wall turbulence still apply.

(1) *A priori* accuracy of models in the filtered component energy or Reynolds stress transport equation is a good predictor of *a posteriori* accuracy of LES velocity statistics.

(2) Eigenvalues associated with linear operators in a time evolution equation are a moderately good predictor of LES stability. Source terms in the component energy equation, such as production, often result in optimal linear models with positive eigenvalues which tend to cause instability. Therefore, special attention

must be given to modeling these source terms.

(3) It is important to Reynolds-decompose the nonlinear term and to model each part separately, because different parts represent different physical phenomena.

(4) It is important to evaluate the effect of each nonlinear model on the pressure term, because errors in the pressure term are primarily caused by problems with the nonlinear models, specifically their divergent part.

The tremendous computational savings of not resolving the near-wall layer makes feasible LES of turbulent flows through complex geometry. Therefore, the development of accurate LES models for unresolved wall layers is an important step toward the prediction of practical flows using LES. We have revealed two important considerations that have received less attention in the past with regard to modeling of the nonlinear term. These are the Reynolds-decomposition of the nonlinear term and the evalution of it's effect on the pressure term. Within the optimal LES framework, significant *a priori* and *a posteriori* errors resulted from ignoring these two considerations. Because most subgrid models also ignore these considerations and exhibit similar *a posteriori* errors, they likely commit similar modeling errors. Therefore, the lessons learned from our research may be used to improve near-wall subgrid modeling in general.

Appendices

Appendix A

Determination of $\mathbb{S}$ in the Inertial Range

The derivation of (3.8) starts from the general form of an isotropic third-rank tensor function of a vector argument

$$\mathbb{S}_{ijk}(\mathbf{r}) = \langle u_i(\mathbf{x}) u_j(\mathbf{x}) u_k(\mathbf{x}+\mathbf{r}) \rangle = a\, r_i r_j r_k + b\, \delta_{jk} r_i + c\, \delta_{ik} r_j + d\, \delta_{ij} r_k \tag{A.1}$$

where the scalars a, b, c and d are functions of the magnitude of the separation vector $r = \|\mathbf{r}\|$ only. Symmetry in i and j requires that $b = c$. Further, the continuity constraint $\partial \mathbb{S}_{ijk}/\partial r_k = 0$ allows the functions a, b and d to be eliminated in terms of the third-order longitudinal correlation function:

$$f(r) = \langle v_{\|}^2(\mathbf{x}) v_{\|}(\mathbf{x}+\mathbf{r}) \rangle, \tag{A.2}$$

where $v_{\|}$ is the velocity component parallel to the separation vector $\mathbf{r}$. The result is

$$\mathbb{S}_{ijk}(\mathbf{r}) = \left\{ \frac{1}{2}\left(f - r\frac{df}{dr} \right) \frac{r_i r_j r_k}{r^3} + \frac{1}{4r^2}\left(\delta_{jk} r_i + \delta_{ik} r_j\right) \frac{d}{dr}\left(r^2 f\right) - \frac{f}{2r}\delta_{ij} r_k \right\}. \tag{A.3}$$

The third-order longitudinal correlation function is directly related to the third-order structure function, which in the Kolmogorov inertial range is $S_3(r) = -\frac{4}{5}\epsilon r$. The correlation $f(r)$ can thus be written

$$f(r) = \frac{S_3(r)}{6} = -\frac{2\epsilon r}{15} \tag{A.4}$$

Substituting into (A.3) then immediately yields (3.8).

Appendix B

The Most General Form for Φ

Presented here is a condensed version of the derivation from Proudman and Reid [54]. The three-point third-order velocity correlation is $\mathbb{T}_{ijk}(\mathbf{r},\mathbf{s}) \equiv \langle v_i(\mathbf{x})v_j(\mathbf{x}+\mathbf{r})v_k(\mathbf{x}+\mathbf{s})\rangle$. It's Fourier transform is

$$\Phi_{ijk}(\boldsymbol{\rho},\boldsymbol{\sigma}) = i(2\pi)^{-6}\int\int \mathbb{T}_{ijk}(\mathbf{r},\mathbf{s})e^{-i(\boldsymbol{\rho}\cdot\mathbf{r}+\boldsymbol{\sigma}\cdot\mathbf{s})}\,d\mathbf{r}\,d\mathbf{s} \tag{B.1}$$

Consistency with continuity requires:

$$(\rho_i+\sigma_i)\Phi_{ijk}(\boldsymbol{\rho},\boldsymbol{\sigma}) = \rho_j\Phi_{ijk}(\boldsymbol{\rho},\boldsymbol{\sigma}) = \sigma_k\Phi_{ijk}(\boldsymbol{\rho},\boldsymbol{\sigma}) = 0 \tag{B.2}$$

While the most general isotropic third-ranked tensor function of two vectors is:

$$\begin{aligned}\phi_{mnp}(\boldsymbol{\rho},\boldsymbol{\sigma}) = \phi_1\rho_m\rho_n\rho_p + \phi_2\rho_m\rho_n\sigma_p + \phi_3\rho_m\sigma_n\rho_p + \phi_4\sigma_m\rho_n\rho_p \\ +\phi_5\sigma_m\sigma_n\sigma_p + \phi_6\sigma_m\sigma_n\rho_p + \phi_7\sigma_m\rho_n\sigma_p + \phi_8\rho_m\sigma_n\sigma_p \\ +\phi_9\rho_m\delta_{np} + \phi_{10}\rho_n\delta_{mp} + \phi_{11}\rho_p\delta_{mn} + \phi_{12}\sigma_m\delta_{np} + \phi_{13}\sigma_n\delta_{mp} + \phi_{14}\sigma_p\delta_{mn}\end{aligned} \tag{B.3}$$

where $\{\phi_1,\phi_2,...,\phi_{14}\}$ are scalar functions of the magnitudes of the wavevectors $\rho \equiv |\boldsymbol{\rho}|$, $\sigma \equiv |\boldsymbol{\sigma}|$, and $\tau \equiv |\boldsymbol{\tau}|$, and $\boldsymbol{\rho}+\boldsymbol{\sigma}+\boldsymbol{\tau} = 0$.

To enforce incompressibility, we employ the divergence-free projector $\Delta_{im}(\boldsymbol{\rho}) \equiv \delta_{im} - \rho_i\rho_m/\rho^2$. So, to satisfy all three incompressibility conditions in equation (B.2) and isotropy, we apply three projectors to ϕ_{mnp}, the result is the most general form for Φ_{ijk}.

$$\Phi_{ijk}(\boldsymbol{\rho},\boldsymbol{\sigma}) = \Delta_{im}(\boldsymbol{\tau})\Delta_{jn}(\boldsymbol{\rho})\Delta_{kp}(\boldsymbol{\sigma})\phi_{mnp}(\boldsymbol{\rho},\boldsymbol{\sigma}) \tag{B.4}$$

Furthermore, the triple projection operator directly eliminates all but 4 components of ϕ_{mnp} shown in equation (B.3), so effectively the above equation becomes

$$\Phi_{ijk}(\boldsymbol{\rho},\boldsymbol{\sigma}) = \Delta_{im}(\boldsymbol{\tau})\Delta_{jn}(\boldsymbol{\rho})\Delta_{pk}(\boldsymbol{\sigma})\left[\phi_3\rho_m\sigma_n\rho_p + \phi_9\rho_m\delta_{np} + \phi_{11}\rho_p\delta_{mn} + \phi_{13}\sigma_n\delta_{mp}\right] \tag{B.5}$$

Renaming the scalar functions as follows: $\phi_3 \to \zeta$, $\phi_9 \to \phi$, $\phi_{11} \to \phi_2$, $\phi_{13} \to \phi_1$, we obtain (3.9).

Appendix C

Calculation Procedures for Basis Functions of $\mathbb{T}$

Symbolic calculation of the tensor basis functions $\mathbb{T}^n$ were carried out using a collection of scripts written in Matlab. These scripts operate on mathematical expressions in the form of strings of characters, such as

```
-36*DELTA_ik*r^6*s^-3*s_j*t^-3 + 432*r^-1*r_j*r_k*s_i*t^-1
```

which is just a small part of $\mathbb{T}^1$. Scripts perform addition, multiplication, and spatial differentiation (gradient or divergence). Addition and multiplication of terms is straightforward. Derivatives with respect to the separation vectors of scalars (e.g. r^5) and vectors (e.g. $\mathbf{r}$) must be computed. The following simple rules for the evaluation of the derivatives ∂_i^r

$$\partial_i^r s^\alpha = \left.\frac{\partial s^\alpha}{\partial s_i}\right|_{\mathbf{r}} = \alpha s^{\alpha-2} s_i \tag{C.1}$$

$$\partial_i^r t^\alpha = \left.\frac{\partial t^\alpha}{\partial s_i}\right|_{\mathbf{r}} = -\alpha t^{\alpha-2} t_i \tag{C.2}$$

$$\partial_i^r s_j = \left.\frac{\partial s_j}{\partial s_i}\right|_{\mathbf{r}} = \delta_{ij} \tag{C.3}$$

$$\partial_i^r t_j = \left.\frac{\partial t_j}{\partial s_i}\right|_{\mathbf{r}} = -\delta_{ij}, \tag{C.4}$$

are implemented in the symbolic manipulation scripts, along with analogous rules for ∂_i^s and ∂_i^t. These along with the chain rule are sufficient to evaluate (3.12).

Finally, the scripts also simplify contractions; for example: $\delta_{ij} r_i = r_j$, $r_j s_j = \mathbf{r} \cdot \mathbf{s}$, and $s_j s_j = s^2$.

Using the symbolic evaluator described above, (3.12) was evaluated for 20 different ψ given by $\psi = p_{a,b} \equiv (r^a s^b - r^b s^a) t^c$, where $a + b + c = 8$ and a, b, $c \geq 0$ are integers. Of these 20 candidate tensor expressions, 14 are non-zero. However, all 14 have discontinuities and/or singularities (which are non-physical) at r, s, or t of zero.

To eliminate the discontinuities and singularities, linear combinations of the 14 non-trivial basis functions are sought which exactly cancel them. This is done by using the first order approximation of $\mathbf{t}$ for small s, namely $\mathbf{t} \approx \mathbf{r}$ and simplifying the resulting expressions for each basis function. Singular and discontinuous terms (for small s) are identified as those with net power of s that is less than or equal to zero, and that are not independent of s. Thus, terms with factors such as s_k/s or $s_i s_j s_k / s^3$ are identified as discontinuous at $s = 0$ (their limiting values as $s \to 0$ depend on the direction of the approach), while factors such as s_k/s^3 and $1/s$ are simply singular at $s = 0$. Each of the 14 reduced basis tensors includes one or more of 28 distinct discontinuous or singular terms. The null space of the 28×14 matrix of coefficients of the singular and discontinuous terms defines the space of tensor function in which all these terms cancel. Remarkably, it was found that the dimension of this null space is 6 (rather than zero). A vector basis for the null space then defines a basis of tensor functions in which the problematic terms have been eliminated.

However, this does not necessarily lead to a basis free of singularities and discontinuities. The reason is that the approximation for $\mathbf{t}$ was only first order in s, and higher order terms can also lead to singularities or discontinuities. Indeed, it was observed that 4 of the 6 basis tensors determined above were discontinuous. By substituting $\mathbf{t} = \mathbf{r} - \mathbf{s}$, and expanding to explicitly expose the higher-order terms in s, the remaining singular/discontinuous terms were identified. Using the same procedure described above, it was found that these singularities and discontinuities had a five-dimensional null-space. A basis for the five-dimensional space of continuous nonsingular model tensors is thus found and is given in equations (3.25–3.29).

Appendix D

Simplest Optimal Model Matches Budget Term

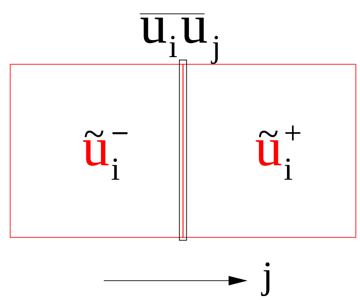

Figure D.1: Configuration of simplest stencil cells $\tilde{u}_i$ with respect to flux $\overline{u_i u_j}$.

The simplest stencil ($L20$) for $\overline{u_i u_j}$ is shown in figure (D.1). A general model including this stencil may be written $\overline{u_i u_j}^{mod}_{L20}$

$$\overline{u_i u_j}^{mod}_{L20} = L^- \tilde{u}_i'^- + L^+ \tilde{u}_i'^+ + ... \tag{D.1}$$

The corresponding optimal model will be denoted $\overline{u_i u_j}^{opt}_{L20}$

$$\overline{u_i u_j}^{opt}_{L20} = L^-_{opt} \tilde{u}_i'^- + L^+_{opt} \tilde{u}_i'^+ + ... \tag{D.2}$$

It shall be shown that any optimal model including linear dependence on the two adjacent $\tilde{u}_i'$ cells, as shown in figure (D.1), also statistically matches the corresponding term in the component energy equation, that is:

$$\left\langle \tilde{u}_i' (\overline{u_i u_j}^{opt-}_{L20} - \overline{u_i u_j}^{opt+}_{L20}) \right\rangle = \left\langle \tilde{u}_i' (\overline{u_i u_j}^- - \overline{u_i u_j}^+) \right\rangle \tag{D.3}$$

where superscript $(-/+)$ refers to the face to the $(-j/+j)$ side of cell $\tilde{u}_i$.

The definition of an optimal model is one which minimizes the squared difference between model and data, which we will call S:

$$S = \left\langle (\overline{u_i u_j}^{mod}_{L20} - \overline{u_i u_j})^2 \right\rangle \tag{D.4}$$

$$\left\langle (\overline{u_i u_j}^{mod}_{L20} - \overline{u_i u_j})^2 \right\rangle \geq \left\langle (\overline{u_i u_j}^{opt}_{L20} - \overline{u_i u_j})^2 \right\rangle \forall L^-, L^+ \tag{D.5}$$

To solve for the optimal model, we set to zero derivatives of S with respect to the coefficients $(L^-, L^+, ...)$. For L^-, this is

$$\frac{\partial S}{\partial L^-} = \left\langle 2(\overline{u_i u_j}^{\cancel{mod} \to opt}_{L20} - \overline{u_i u_j}) \underbrace{\frac{\partial \overline{u_i u_j}^{mod}_{L20}}{\partial L^-}}_{\tilde{u}_i'^-} \right\rangle = 0 \tag{D.6}$$

$$\left\langle (\overline{u_i u_j}^{opt}_{L20} - \overline{u_i u_j}) \tilde{u}_i'^- \right\rangle = 0 \tag{D.7}$$

where we write $\overline{u_i u_j}^{\cancel{mod} \to opt}_{L20}$ because it is the specific model that acheives the zero derivative condition. Doing the same thing for L^+, we get

$$\left\langle (\overline{u_i u_j}^{opt}_{L20} - \overline{u_i u_j}) \tilde{u}_i'^+ \right\rangle = 0 \tag{D.8}$$

The above two equations are the optimality conditions corresponding to events $\tilde{u}_i'^-$ and $\tilde{u}_i'^+$. Shifting from face-centered reference to cell-centered reference, these equations become

$$\left\langle (\overline{u_i u_j}^{opt+}_{L20} - \overline{u_i u_j}^{+}) \tilde{u}_i' \right\rangle = 0 \tag{D.9}$$

$$\left\langle (\overline{u_i u_j}^{opt-}_{L20} - \overline{u_i u_j}^{-}) \tilde{u}_i' \right\rangle = 0 \tag{D.10}$$

Subtracting the above two equations and rearranging

$$\left\langle (\overline{u_i u_j}^{opt+}_{L20} - \overline{u_i u_j}^{opt-}_{L20} - \overline{u_i u_j}^{+} + \overline{u_i u_j}^{-})\tilde{u}'_i \right\rangle = 0 \tag{D.11}$$

$$\left\langle (\overline{u_i u_j}^{opt+}_{L20} - \overline{u_i u_j}^{opt-}_{L20})\tilde{u}'_i \right\rangle = \langle (\overline{u_i u_j}^{+} - \overline{u_i u_j}^{-})\tilde{u}'_i \rangle \tag{D.12}$$

Appendix E

Standard Quadratic Model Conserves Energy

The standard quadratic approximation for staggered uniform grids, conserves component energies when the velocity field is divergence-free and boundaries are zero or periodic.

We will prove this discretely, but first let's prove this in a continuous setting which is easier. Let u_i be divergence-free ($\partial_i u_i = 0$) on domain Ω. The quadratic term $u_\alpha u_j$ in the $u_\alpha u_\alpha$ energy equation is

$$u_\alpha \partial_j u_\alpha u_j = u_\alpha u_\alpha \underbrace{\partial_j u_j}_{0} + u_\alpha u_j \partial_j u_\alpha = \partial_j u_\alpha u_\alpha u_j - u_\alpha \partial_j u_\alpha u_j \tag{E.1}$$

Rearranging

$$2 u_\alpha \partial_j u_\alpha u_j = \partial_j u_\alpha u_\alpha u_j \tag{E.2}$$

Integrating over Ω

$$2 \int_\Omega u_\alpha \partial_j u_\alpha u_j = \int_\Omega \partial_j u_\alpha u_\alpha u_j = \int_{\partial\Omega} u_\alpha u_\alpha u_j n_j = 0 \tag{E.3}$$

The right equality is because the boundaries are zero or periodic. Therefore, energy only enters or exits through the boundaries.

We will now show that the standard quadratic approximation $\overline{u_\alpha u_j}^{mod}_{std}$ does this discretely. Consider the quadratic term $\overline{u_\alpha u_j}^{mod}_{std}$ in the $\tilde{u}_\alpha \tilde{u}_\alpha$ energy equation

$$\tilde{u}_\alpha \tilde{\partial}_j \overline{u_\alpha u_j}^{mod}_{std} \tag{E.4}$$

Summation in j is implied. For simplicity consider 2-D and $\alpha = x$.

$$\tilde{u}\tilde{\partial}_j\overline{u_\alpha u_j}^{mod}_{std} = \tilde{u}\tilde{\partial}_x\overline{uu}^{mod}_{std} + \tilde{u}\tilde{\partial}_y\overline{uv}^{mod}_{std} \tag{E.5}$$

Now, let us change notation a little and let i, j denote indices for cell location. A diagram showing the configuration centered at cell $\tilde{u}^{i,j}$ is shown in figure (E.1). The above term can then be expanded to

$$\begin{aligned} &\frac{\tilde{u}^{i,j}}{\Delta_x}\left(\left(\frac{\tilde{u}^{i,j}+\tilde{u}^{i+1,j}}{2}\right)^2 - \left(\frac{\tilde{u}^{i,j}+\tilde{u}^{i-1,j}}{2}\right)^2\right) \\ +&\frac{\tilde{u}^{i,j}}{\Delta_y}\left(\left(\frac{\tilde{u}^{i,j}+\tilde{u}^{i,j+1}}{2}\right)\left(\frac{\tilde{v}^{i,j+1}+\tilde{v}^{i-1,j+1}}{2}\right) - \left(\frac{\tilde{u}^{i,j}+\tilde{u}^{i,j-1}}{2}\right)\left(\frac{\tilde{v}^{i,j}+\tilde{v}^{i-1,j}}{2}\right)\right) \end{aligned} \tag{E.6}$$

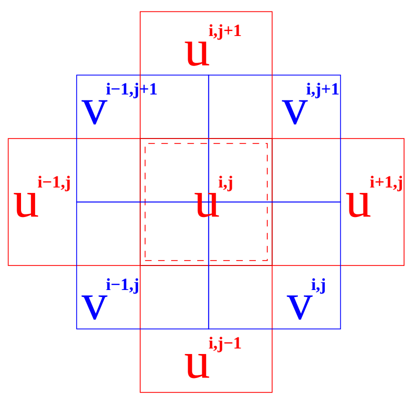

Figure E.1: Configuration of cells used in standard quadratic model for calculation of energy centered on cell $\tilde{u}^{i,j}$

Gathering together all the $\tilde{u}^{i,j}\tilde{u}^{i,j}$ terms

$$\frac{\tilde{u}^{i,j}\tilde{u}^{i,j}}{4}\left(\frac{\tilde{u}^{i,j}+2\tilde{u}^{i+1,j}-\tilde{u}^{i,j}-2\tilde{u}^{i-1,j}}{\Delta_x} + \frac{\tilde{v}^{i,j+1}+\tilde{v}^{i-1,j+1}-\tilde{v}^{i,j}-\tilde{v}^{i-1,j}}{\Delta_y}\right) + ... \tag{E.7}$$

The divergence free condition $\frac{\tilde{u}^{i+1,j}-\tilde{u}^{i,j}}{\Delta_x} + \frac{\tilde{v}^{i,j+1}+\tilde{v}^{i,j}}{\Delta_y} = 0$ eliminates all the above terms, except the two terms with coefficient 2. Then adding in the rest of the terms containing the cross terms $\tilde{u}^{i,j}\tilde{u}^{i\pm1,j\pm1}$

$$\begin{aligned} &\frac{\tilde{u}^{i,j}\tilde{u}^{i+1,j}(\tilde{u}^{i,j}+\tilde{u}^{i+1,j}) - \tilde{u}^{i,j}\tilde{u}^{i-1,j}(\tilde{u}^{i,j}+\tilde{u}^{i-1,j})}{4\Delta_x} \\ +&\frac{\tilde{u}^{i,j}\tilde{u}^{i,j+1}(\tilde{v}^{i,j+1}+\tilde{v}^{i-1,j+1}) - \tilde{u}^{i,j}\tilde{u}^{i,j-1}(\tilde{v}^{i,j}+\tilde{v}^{i-1,j})}{4\Delta_y} \end{aligned} \tag{E.8}$$

Notice that the left and right terms above are like exact differentials $\partial_x uuu$ and $\partial_y uuv$. Therefore, when summed over the domain, they result in only boundary terms.

$$\begin{aligned} &\frac{\tilde{u}^{R,j}\tilde{u}^{R+1,j}(\tilde{u}^{R,j}+\tilde{u}^{R+1,j}) - \tilde{u}^{L,j}\tilde{u}^{L-1,j}(\tilde{u}^{L,j}+\tilde{u}^{L-1,j})}{4\Delta_x} \\ +&\frac{\tilde{u}^{i,T}\tilde{u}^{i,T+1}(\tilde{v}^{i,T+1}+\tilde{v}^{i-1,T+1}) - \tilde{u}^{i,B}\tilde{u}^{i,B-1}(\tilde{v}^{i,B}+\tilde{v}^{i-1,B})}{4\Delta_y} \end{aligned} \tag{E.9}$$

where right, left, top, and bottom boundary cells are denoted R, L, T, B. One can see that if boundaries are periodic, $R+1 = L$ or $T+1 = B$, then boundary terms cancel, leaving net zero energy flux. If boundary velocities are zero, $\tilde{u}^{R,j} = \tilde{u}^{L,j} = 0$ or $\tilde{v}^{i,T+1} = \tilde{v}^{i,B} = 0$, then the boundary terms are also zero. Note that in this case, or in general with any non-periodic boundary and staggered grid, that the velocity component in the non-periodic direction has one extra grid cell in that direction, and that the boundary cells straddle the boundary.

Appendix F

Discrete Divergence-Free Projection

F.1 Discrete Divergence-Free Projection of the Filtered Field

A divergence-free continuous field u does not imply a discretely divergence-free filtered field $\tilde{u}$. Figure (F.1) shows discrete divergence of filtered fields $\left\langle \tilde{\nabla} \cdot \tilde{u})^2 \right\rangle^{1/2}$, which is non-zero everywhere and gets larger close to the wall.

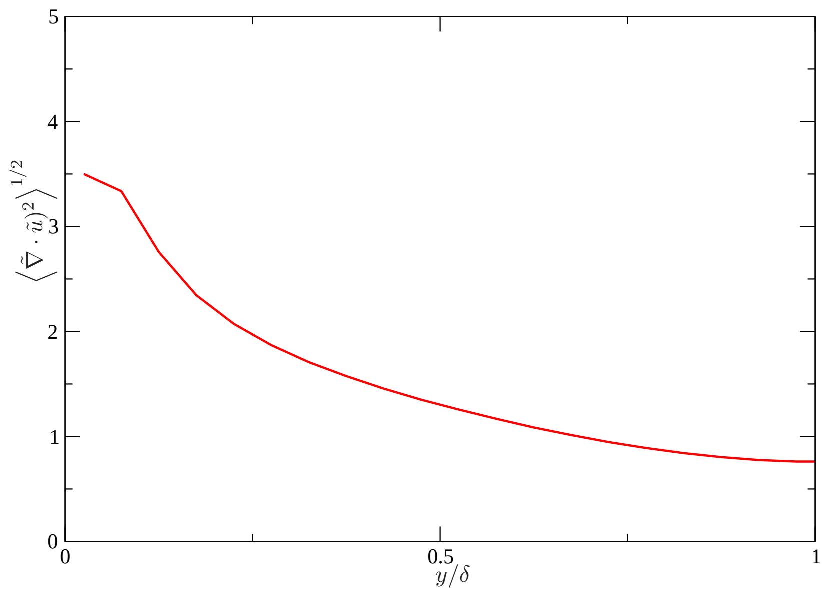

Figure F.1: Discrete divergence of filtered fields, for channel flow at $Re_\tau = 934$

However, the energy content of the discretely divergent part of the filtered field is small. Figure (F.2) shows the variances $\langle \tilde{u}^2 \rangle$, $\langle \tilde{v}^2 \rangle$, $\langle \tilde{w}^2 \rangle$, $\langle \tilde{u}\tilde{v} \rangle$ of the fields with (dotted curves) and without (solid curves) divergence-free projection. The curves with and without divergence-free projection are very close everywhere, with slight deviation near the wall.

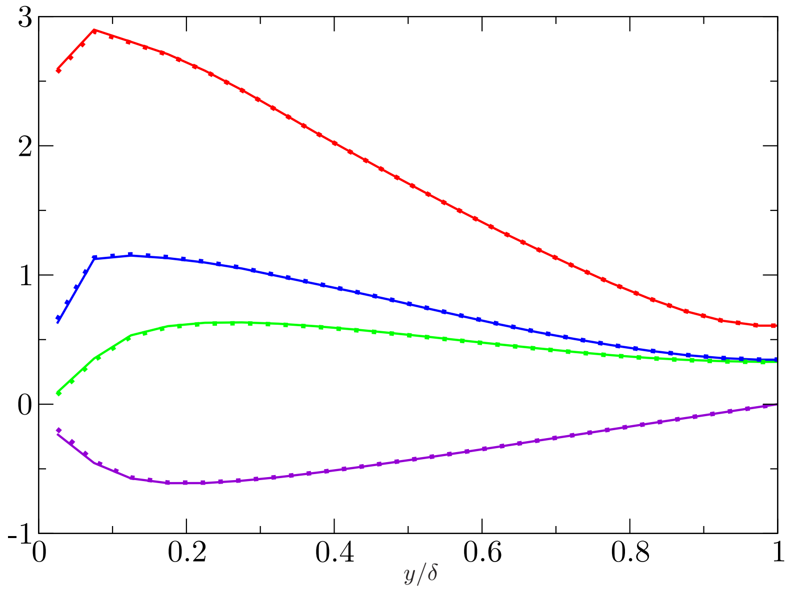

Figure F.2: Velocity variances $\langle \tilde{u}^2 \rangle$, $\langle \tilde{v}^2 \rangle$, $\langle \tilde{w}^2 \rangle$, $\langle \tilde{u}\tilde{v} \rangle$ of the fields with (dotted curves) and without (solid curves) divergence-free projection, for channel flow at $Re_\tau = 934$

F.2 Discrete Divergence-Free Projection Boundary Condition

Let u be the continuous fields, let $\tilde{u}$ be the filtered fields, and let $\tilde{u}^p$ be the discrete divergence-free projection of the filtered fields. The actual boundary condition implemented for the discrete divergence-free projection is $\tilde{u}_2^p = 0$ along the wall, regardless of the values of u_2 along the wall. Noting that the boundary $\tilde{u}_2$ straddles the wall, the filtering operation on this cell volume averages u_2 on the half of the cell that is inside the domain. u_2 outside the domain is undefined and *assumed* to be zero. This makes $\tilde{u}_2$ small but non-zero. It maybe argued that the region outside the domain should not be treated as having zero velocity, but having the reflected value $u_2(-y) = -u_2(y)$, in which case, $\tilde{u}_2 \equiv 0$. What difference does this make in taking the divergence-free projection? Whether or not $\tilde{u}_2 = 0$ at the wall makes no difference in result of the discrete divergence-free projection $\tilde{u}^p$. Likewise, it makes no difference whether or not $\tilde{u}_2^p$ at the wall gets evolved.

Bibliography

[1] R. Adrian. On the role of conditional averages in turbulence theory. In J. Zakin and G. Patterson, editors, *Turbulence in Liquids*, pages 323–332. Science Press, Princeton, New Jersey, 1977.

[2] R. Adrian, B. Jones, M. Chung, Y. Hassan, C. Nithianandan, and A. Tung. Approximation of turbulent conditional averages by stochastic estimation. *Physics of Fluids*, 1(6):992–998, 1989.

[3] R. Adrian and P. Moin. Stochastic estimation of organized turbulent structure: homogeneous shear flow. *Journal of Fluid Mechanics*, 190:531–559, 1988.

[4] R. J. Adrian. Stochastic estimation of sub-grid scale motions. *Appl. Mech. Rev.*, 43:214, 1990.

[5] E. Balaras, C. Benocci, and U. Piomelli. Finite-difference computations of high reynolds number flows using the dynamic subgrid-scale model. *Theoretical and Computational Fluid Dynamics*, 7:207–216, 1995.

[6] E. Balaras, C. Benocci, and U. Piomelli. Two-layer approximate boundary conditions for large-eddy simulations. *AIAA Journal*, 34:1111–1119, 1996.

[7] J. Bardina, J. Ferziger, and W. Reynolds. Improved subgrid-scale models for large-eddy simulation. AIAA-80-1357, 1980.

[8] Y. Bazilevs, V.M. Calo, J.A. Cottrell, T.J.R. Hughes, A. Reali, and G. Scovazzi. Variational multiscale residual-based turbulence modeling for large eddy simulation of incompressible flows. *Computer Methods in Applied Mechanics and Engineering*, 197:173–201, 2007.

[9] A. Bhattacharya, A. Das, and R. D. Moser. A filtered-wall formulation for large-eddy simulation of wall-bounded turbulence. *Physics of Fluids*, 20:115104, 2008.

[10] A. Bhattacharya, S. C. Kassinos, and R. D. Moser. Representing anisotropy of two-point second-order turbulence velocity correlations using structure tensors. *Physics of Fluids*, 20:101502, 2008.

[11] J. Boris, F. Grinstein, E. Oran, and R. Kolbe. New insights into large eddy simulation. *Fluid Dynamics Research*, 10(4–6):199–228, 1992.

[12] W. Cabot and P. Moin. Approximation wall boundary conditions in the large-eddy simulation of high reynolds number flow. *Flow, Turbulence and Combustion*, 63:269–291, 1999.

[13] H. Chang and R. D. Moser. An inertial range model for the three-point third-order velocity correlation. *Physics of Fluids*, 19:105111, 2007.

[14] J. Chollet and M. Lesieur. Parameterization of small scales of three-dimensional isotropic turbulence using spectral closures. *Journal of the Atmospheric Sciences*, 38:2747–2757, 1981.

[15] A. J. Chorin. Numerical solution of the navier-stokes equations. *Mathematics of Computation*, 22:745–762, 1968.

[16] D. Chung and D. I. Pullin. Large-eddy simulation and wall modelling of turbulent channel flow. *Journal of Fluid Mechanics*, 631:281–309, 2009.

[17] J. W. Deardorff. A numerical study of three-dimensional turbulence channel flow at high reynolds numbers. *Journal of Fluid Mechanics*, 41:453–480, 1970.

[18] J. C. del Alamo, J. Jimenez, P. Zandonade, and R. D. Moser. Scaling of the energy spectra of turbulent channels. *Journal of Fluid Mechanics*, 500:135–144, 2004.

[19] P. A. Durbin and B. A. Petterson Reif. *Statistical Theory and Modeling for Turbulent Flows*. John Wiley & Sons, 2002.

[20] C. L. Fefferman. Existence and smoothness of the navier-stokes equation. In A. Wiles J. Carlson, A. Jaffe, editor, *The Millennium Prize Problems*, page 57. Clay Mathematics Institute, Cambridge, 2000.

[21] U. Frisch. *Turbulence: The Legacy of A. N. Kolmogorov*. Cambridge U. Press, 1995.

[22] M. Germano, U. Piomelli, P. Moin, and W. Cabot. A dynamic subgrid-scale eddy viscosity model. *Physics of Fluids*, 3:1760–1765, 1991.

[23] S. Ghosal. An analysis of numerical errors in large-eddy simulations of turbulence. *Journal of Computational Physics*, 125:187–206, 1996.

[24] M. D. Greenberg. *Advanced Engineering Mathematics*. Pearson Education, 1998.

[25] F. H. Harlow and J. E. Welch. Numerical calculation of time-dependent viscous incompressible flow of fluid with free surface. *Physics of Fluids*, 8:2182–2189, 1965.

[26] S. Hoyas and J. Jiménez. Scaling of velocity fluctuations in turbulent channels up to $re_\tau = 2000$. *Physics of Fluids*, 18:011702, 2006.

[27] Javier Jiménez and Robert D. Moser. LES: Where are we and what can we expect. *AIAA J.*, 38:605–612, 2000.

[28] J. Kim, P. Moin, and R. D. Moser. Turbulence statistics in fully developed channel flow at low reynolds number. *Journal of Fluid Mechanics*, 177:133, 1987.

[29] A. N. Kolmogorov. Dissipation of energy in locally isotropic turbulence. *Dokl. Akad. Nauk SSSR*, 32:16–18, 1941. reprinted in *Proc. R. Soc. Lond. A* **434** 15-17 (1991).

[30] A. N. Kolmogorov. The local structure of turbulence in incompressible viscous fluid for very large reynolds numbers. *Dokl. Akad. Nauk SSSR*, 30:299–303, 1941. reprinted in *Proc. R. Soc. Lond. A* **434** 9-13 (1991).

[31] R. Kraichnan. The structure of isotropic turbulence at very high Reynolds numbers. *Journal of Fluid Mechanics*, 5:497–543, 1959.

[32] R. H. Kraichnan. Direct interaction approximation for shear and thermally driven turbulence. *Phys. Fluids*, 7:1048, 1964.

[33] A. G. Kravchenko and P. Moin. On the effect of numerical errors in large eddy simulations of turbulent flows. *Journal of Computational Physics*, 131:310–322, 1997.

[34] J. Langford and R. Moser. Optimal LES formulations for isotropic turbulence. *Journal of Fluid Mechanics*, 398:321–346, 1999.

[35] J. A. Langford. *Toward ideal large-eddy simulation.* PhD thesis, University of Illinois at Urbana-Champaign, Urbana-Champaign, Illinois, 2000.

[36] J. A. Langford and R. D. Moser. Breakdown of continuity in large-eddy simulation. *Physics of Fluids*, 11:943–945, 2001.

[37] J. A. Langford and R. D. Moser. Optimal large-eddy simulation results for isotropic turbulence. *Journal of Fluid Mechanics*, 521:273–294, 2004.

[38] M. Lesieur. *Turbulence in Fluids.* Kluwer Academic Publishers, Dordrecht, 3rd edition, 1997.

[39] M. Lesieur and O. Métais. New trends in large-eddy simulations of turbulence. *Annual Review of Fluid Mechanics*, 28:45–82, 1996.

[40] E. Leveque, F. Toschi, L. Shao, and J.-P. Bertoglio. Shear-improved smagorinsky model for large-eddy simulation of wall-bounded turbulent flows. *Journal of Fluid Mechanics*, 570:491–502, 2007.

[41] D. Lilly. A proposed modification of the Germano subgrid-scale closure method. *Physics of Fluids*, 4(3):633–635, 1992.

[42] I. Marusic. Unravelling turbulence near walls. *Journal of Fluid Mechanics*, 630:1–4, 2009.

[43] C. Meneveau and J. Katz. Scale-invariance and turbulence models for large-eddy simulation. *Annual Review of Fluid Mechanics*, 32:1–32, 2000.

[44] A. Misra and D. I. Pullin. A vortex-based subgrid model for large-eddy simulation. *Physics of Fluids*, 9:2443–2454, 1997.

[45] P. Moin and K. Mahesh. Direct numerical simulation: A tool in turbulence research. *Annual Review of Fluid Mechanics*, 30:539–578, 1998.

[46] R. D. Moser, J. Kim, and N. N. Mansour. Direct numerical simulation of turbulent channel flow up to $Re_\tau = 590$. *Physics of Fluids*, 11(4):943–945, April 1999.

[47] R. D. Moser, N. P. Malaya, H. Chang, P. S. Zandonade, P. Vedula, A. Bhattacharya, and A. Haselbacher. Theoretically based optimal large-eddy simulation. *Physics of Fluids*, 21:105104, 2009.

[48] F. Nicoud, J. S. Baggett, P. Moin, and W. Cabot. Large eddy simulation wall-modeling based on suboptimal control theory and linear stochastic estimation. *Physics of Fluids*, 13(10):2968–2984, 2001.

[49] J. O'Neil and C. Meneveau. Spatial correlations in turbulence: Predictions from the multifractal formalism and comparison with experiments. *Phys. of Fluids A*, 5(1):158–172, 1993.

[50] U. Piomelli and E. Balaras. Wall-layer models for large-eddy simulations. *Annual Review of Fluid Mechanics*, 34:349–374, 2002.

[51] U. Piomelli, P. Moin, J.H. Ferziger, and J. Kim. New approximate boundary conditions for large-eddy simulations of wall-bounded flows. *Physics of Fluids A*, 1:1061–1068, 1989.

[52] S. B. Pope. *Turbulent Flows.* Cambridge University Press, 2000.

[53] S. B. Pope. Ten questions concerning the large-eddy simulation of turbulent flows. *New Journal of Physics*, 6:35, 2004.

[54] I. Proudman and W. H. Reid. On the decay of a normally distributed and homogeneous turbulent velocity field. *Phil. Trans. R. Soc. Lond. A*, 247:163–189, 1954.

[55] J. Qian. Correlation coefficients between the velocity difference and local average dissipation of turbulence. *Physical Review E*, 54(1):981–984, 1996.

[56] J. Qian. Closure approach to high-order structure functions of turbulence. *Phys. Rev. Lett.*, 84:646–649, 2000.

[57] W. C. Reynolds. The potential and limitations of direct and large eddy simulations. In J. L. Lumley, editor, *Whither Turbulence? Turbulence at the Crossroads*, pages 313–343. Springer-Verlag, Berlin, 1990.

[58] R. Rogallo and P. Moin. Numerical simulation of turbulent flows. *Annual Review of Fluid Mechanics*, 16:99–137, 1984.

[59] U. Schumann. Subgrid scale model for finite difference simulations of turbulent flows in plane channels and annuli. *Journal of Computational Physics*, 18:376–404, 1975.

[60] L. Shao, Z. Zhang, G. Cui, and C. Xu. Subgrid modeling of anisotropic rotating homogeneous turbulence. *Physics of Fluids*, 17(11):115106–1–115106–7, 2005.

[61] J. Smagorinsky. General circulation experiments with the primitive equations. *Monthly Weather Review*, 91:99–164, 1963.

[62] P. R. Spalart, W. H. Jou, M. Strelets, and S. R. Allmaras. Comments on the feasibility of les for wings and on a hybrid rans/les approach. In C. Liu and Z. Liu, editors, *Advances in DNS/LES*, pages 137–148. Columbus, OH, 1997.

[63] C. Speziale. Analytical methods for the development of Reynolds-stress closures in turbulence. *Annual Review of Fluid Mechanics*, 23:107–157, 1991.

[64] K. R. Sreenivasan and R. A. Antonia. The phenomenology of small-scale turbulence. *Annu. Rev. Fluid Mech.*, 29:435–472, 1997.

[65] P. Vedula, R. D. Moser, and P. S. Zandonade. On the validity of quasi-normal approximation in turbulent channel flow. *Physics of Fluids*, 17:055106, 2005.

[66] S. Volker, P. Venugopal, and R. D. Moser. Optimal large eddy simulation of turbulent channel flow based on direct numerical simulation statistical data. *Physics of Fluids*, 14:3675, 2002.

[67] T. von Karman and L. Howarth. On the statistical theory of isotropic turbulence. *Proc. R. Soc. Lond. A*, 164:192–215, 1938.

[68] P. S. Zandonade, J. A. Langford, and R. D. Moser. Finite volume optimal large-eddy simulation of isotropic turbulence. *Physics of Fluids*, 16:2255–2271, 2004.

Vita

Henry Chang graduated from Webb Institute with a Bachelor of Science in Naval Architecture and Marine Engineering in June 1998. He then worked at the Naval Surface Warfare Center Carderock Division in Bethesda, Maryland, until entering graduate school in August 2004. He earned a Master of Science in Theoretical and Applied Mechanics from the University of Illinois at Urbana-Champaign in August 2005. That fall, he enrolled in the Ph.D. program in Computational Science, Engineering, and Mathematics at the University of Texas at Austin.

Email address: changhenry@gmail.com

This dissertation was typeset with LaTeX[†] by the author.

[†] LaTeX is a document preparation system developed by Leslie Lamport as a special version of Donald Knuth's TeX Program.